Reconstructing Cosmology using Principal Component Analysis

Ranbir Sharma

A thesis submitted for the partial fulfillment of

the degree of Doctor of Philosophy

Department of Physical Sciences,

Indian Institute of Science Education and Research Mohali

Knowledge city, Sector 81, SAS Nagar, Manauli PO, Mohali 140306, Punjab,

India.

August, 2022

Declaration

The work presented in this thesis has been carried out by me under the guidance of Dr. Harvinder Kaur Jassal at the Indian Institute of Science Education and Research, Mohali. This work has not been submitted in part or in full for a degree, a diploma, or a fellowship to any other university or institute. Whenever contributions of others are involved, every effort is made to indicate this clearly, with due acknowledgment of collaborative research and discussions. This thesis is a bona fide record of original work done by me and all sources listed within have been detailed in the bibliography.

Ranbir Sharma
(candidate)

In my capacity as the supervisor of the candidate's thesis work, I certify that the above statements by the candidate are true to the best of my knowledge.

Harvinder Kaur Jassal
(Supervisor)

Acknowledgements

At this moment of accomplishment, I would like to express my sincere gratitude towards my thesis supervisor Dr. Harvinder Kaur Jassal. She gave me freedom to explore in my own and help me to nurser my ideas. Her patience, support, and encouragement help me to overcome difficult situations, not only in my academic life but also in general.

I would like to thank Prof. Jasjeet S Bagla for many discussions and inputs which help to improve my Ph.D work. I am thankful to my Ph.D committee member Dr. Rajeev Kapri for his support and fruitful discussions. I acknowledge IISER Mohali for providing the necessary facilities for this Ph.D project. For many fruitful discussions I would like to thank Manvendra, Rohit, Ankit, Avinash, Akash, Swati, Swaraj, Wasim. To stand by my side when I suffered the fatal accident and during the recovery phases, I would like to thank again my colleagues and friends Rohit, Nishat, Manvendra, Avinash, Ankit, Jasjeet, Harvinder, Smriti, Esha, Kanwaljeet, Sudipto and Sourav.

I would also like to take this opportunity to thank my friends, colleagues and comrades Aastha, Mayukh, Mihir, Vineet, Afzal, Shivanshu, Amartya, Rudranil, Shreyan, Subhadip, Gurdev, Kusum, Rajvinder, Simran, Sukhwinder, Kala, Akshi, Neetu, Rito, Vijay, Aman, Sandeepa and Vaibhav. It is solely for them that I understand different aspects of life.

I thank my graduation, post-graduation friends Abeg and Priyanka to inspire me to pursue research, when I was in the time of great confusion. I am thankful to my parents who in spite of many difficulties of their immediate surroundings and their own, never stop inspiring me to carry on my research work.

Abstract

In this thesis, we reconstruct cosmological quantities which dictate the late-time evolution of the Universe using different statistical methods. In the first part of the thesis, we apply the Principal Component Analysis(PCA) to reconstruct the observables in Cosmological data-sets. PCA is a model independent, non-parametric method and can be used to separate the noise of the data from the signal. PCA is an application of linear algebra and we need only the tabulated data-set of the observational quantity as our input. As output we obtain the form of the observable which describes the data-set the best. We modify the PCA algorithm via the calculation of the Covariance matrix. We show that the combination of correlation coefficient calculation(CCC) and PCA (PCA + CCC) can be used as a potential reconstruction tool. (PCA + CCC) give a prescription of selecting the number of final principal components that are sufficient to reconstruct the final observable. We apply our algorithm on a simulated data-set first to validate and check the efficiency of our algorithm. We devise two approaches in the PCA mechanism. The first one is a derived approach, where we reconstruct the observable quantities using PCA and subsequently construct the equation of state parameter of dark energy. The other approach is the direct reconstruction of the equation of state from the data in hand. We use different initial basis vectors to reconstruct the observable quantities and use CCC to select one particular initial basis vector over the other. Given the data-set, we use CCC also to select one approach over the other. The reconstruction of the equation of state indicates a slowly varying equation of state of dark energy.

In the second part of the thesis, we combine PCA and Markov Chain Monte Carlo (MCMC) to infer the cosmological model parameters. We use the No U Turn Sampler (NUTS) to run the MCMC chains in the model parameter space. After validating our methodology with simulated data, we apply the same to observed data-sets. Here we take the points generated from the PCA reconstruction of the observable as the data-set for the Maximum Likelihood Estimation (MLE) and a specific cosmological model as our theory vector. We assume a polynomial expansion over the variable $(1 - a)$, where a is the scale factor as the parametrization of the equation of state of dark energy(EoS). When the method of (PCA + CCC) reconstruction is combined with MCMC tool, we have the freedom of selecting the number of points in the observational part of MLE. We see that the predictions for the model parameters are viable. We show that the parameter estimation does not depend strongly on the prior probability assumption, and the idea can be generalized to other data-sets as well as different sampling techniques. The

relation between the Hubble parameter and the equation of state of dark energy also contains the first differentiation of the Hubble parameter, which introduces an unwanted error in the equation of state predictions. This method eliminates the error that arises from the first order differentiation of the Hubble parameter to infer the value and ranges of the Equation of State of dark energy. In this work, we only use the error function that comes directly from the PCA algorithm, and one can use different error functions in the error part of the MLE as well. It can be used as a model selection tool and can be used in those data-sets which have fewer data-points.

List of Publications

- Ranbir Sharma, Ankan Mukherjee, H K Jassal,
  Reconstruction of late time cosmology using Principal Component Analysis,
  Eur. Phys. J. Plus (2022) 137:219
  [arXiv:2004.01393]

- Ranbir Sharma, H K Jassal,
  Inference of model parameters using Principal Component Analysis,
  Manuscript in preparation

Contents

Chapter 1

Introduction

"The perception that all the processes of nature are systematically connected drives science on to prove this systematic connection throughout, both in general and in particular."

- Anti-D*ü*hring, *F. Engels*,

In the process of evolution of society, different scientific ideas and skills began to develop. We came to know more and more about our surroundings and our position in it. Gradually, we understood the interconnection between different scientific branches, which were developed in isolation of each other. These bridges between different disciplines mark the epochs of different new scientific discoveries which revolutionized science. General theory of relativity is one of them, which changed our way of understanding the Universe. In cosmology, we are interested in studying the origin and evolution of the Universe. Theory of relativity equips us with the mathematical tool to explore the Universe and also enables us to have greater understanding of the fundamental forces of Nature. It establishes the idea that the dynamics of space and time can solely be determined by the energy content of it [1, 2]. Therefore, to understand the dynamics of the spacetime of the Universe we must know the different energy contents of the Universe.

The observable physical quantity for us is the light of different frequencies from stars, galaxies, clusters, and matter in between them as well as the gravitational waves, which come from different merger objects. In the current era, we are not only equipped with sophisticated cosmological models and precise observational dataset, but also the deployment of advanced statistical techniques, which helps us to predict and infer the dynamical models of Universe. In this thesis we explore

methods of utilising the data to determine different parameters which govern the evolution of the Universe.

1.1 An overview

Till the begining of 20th century, the prevailing belief was that the Universe is static and everlasting. Einstein added the "Cosmological Constant (Λ)" to make the solution of General Theory of Relativity (GTR) consistent for the steady state of the Universe. Expansion of the Universe was established by the observations of Hubble and Slipher [3, 4], which was a blow to the steady-state theory of the Universe. After the discovery by Hubble, the next seven decades witnessed development of different dataset which added to our understanding of the Universe's expansion.

The fundamental assumption in cosmology is that the Universe is homogeneous and isotropic. This is known as the cosmological principle. The Einstein equation for a homogeneous and isotropic Universe, give the dynamics of the Universe in terms of cosmic time and determines the different phases of the Universe. The discovery of Cosmic Microwave Background (CMB) by Penzias and Wilson [5, 6] wrecked the deep rooted believe of the steady state theory of the Universe. The 'excess antenna temperature' measured by Penzias and Wilson isotropically in all directions [5] was correctly interpreted in [6], which showed that Universe was clearly adiabatically expanding and cooling as postulated by Lemaitre [7] using a solution of Einstein's field equation found previously by Friedman [8]. In 2006, Mather and Smoot won the Nobel prize for the measurement of the black-body spectrum and the discovery of temperature anisotropy of the cosmic microwave background (CMB) [9]. This discovery put the big bang model of cosmology on a firm footing.

In different phases of the Universe's evolution, different energy components dominate and drive the evolution of the Universe. The Universe underwent a rapid, exponential energy at very early time. This phase namely, inflation gives the causal mechanism for the existence of large-scale structures of the Universe. Inflation solves cosmological problems, such as the flatness and the horizon problem. Universe entered a radiation-dominated era after the end of inflation. In this phase, light elements such as Helium and Deuterium were formed. The radiation-dominated era is followed by the matter-dominated era at around redshift $z \approx 3000$. In the matter-dominated era, pressure-less dark matter began to

dominate the total energy of the Universe. This is the era in which structures (galaxies, clusters) formed.

The baryonic matter in the Universe contributes only about 4-5% to the energy budget. The rest of the energy content of the Universe is "dark". The dark sector of the Universe consists of dark energy and dark matter. Dark matter constitutes almost 25% of the energy density of the Universe. By comparing the dispersion velocities of galaxies in the COMA cluster with the observable star mass, Zwicky had indicated the existence of dark matter as early as 1933[10]. Baryons and dark matter are the main contributors to the formation of large-scale structures. Unlike visible baryonic matters, dark matter does not interact with the electromagnetic force. Its presence is mainly observed from the gravitational effect on surrounding visible matter. From observation and simulation, the clustering property of dark matter due to gravitational instability is proved.

In the year 1998, the observational data collected for Supernovae Type Ia(SNIa) [11] by the High-redshift Supernova Search Team and by the Supernova Cosmology Project Team [12] independently reported that the present Universe is accelerating. This lead to flurry of activity to understand the source of this acceleration in the energy content of the Universe. This unknown energy content of the Universe is dubbed "Dark Energy". Presently, we do not understand whether dark energy is a Cosmological Constant [13–16] or a time-evolving quantity [17, 18]. The energy densities of the matter and radiation decrease with the passage of time. At late times, dark energy catches up with the matter component and starts to dominate the expansion. The onset of cosmic acceleration is around the redshift $z \approx 1$. The cosmological constant Λ is the simplest candidate for dark energy, which has a constant energy density. There is huge discrepancy between the theoretical value predicted and the value suggested by observation. For particle physics, the value of cosmological constant appears as a vacuum energy density, and the estimated value is $\rho_{vac} \approx 10^{74} GeV^4$. This value suggests an eternal early stage of cosmic acceleration in the very early stage. The observed value of vacuum energy is $\rho_\Lambda \approx 10^{-47} GeV^4$. We have to justify the small observed value of ρ_Λ in the case of the cosmological constant scenario. This led to formulation of different alternative scenarios which include fluid models or scalar field models.

The dark energy contribution should have a negative pressure to dictate the accelerating phase of the Universe. Some models belonging to this class are quintessence [19–43], K-essence [44–46], perfect fluid models [47, 48]. Quintessence and K-essence use scalar fields to modify the potential and kinetic terms of the

Lagrangian such that deduction from the Einstein equation gives an accelerating phase. Perfect-fluid models achieve this goal by a specific form of the equation of state. Another approach is to modify the spacetime curvature part of the Einstein equation. Some of the more popular ones are $f(R)$ gravity [49–51], scalar tensor theories [52–56], braneworld models [57, 58]. The models were proposed to solve the fine tuning problem of cosmological constant, however these models have fine tuning problem of their own.

It is an important task to constrain parameters of different models with observational data. The equation of the state of dark energy, which dictates the dynamics of dark energy, is the physical quantity that distinguishes dark energy models from one another. The equation of the state of dark energy is $w_{DE} = \frac{p_{DE}}{\rho_{DE}}$, where p_{DE} is the pressure of dark energy and ρ_{DE} is the energy density. For ΛCDM, the equation of state parameter is constant in time, $w_{DE} = -1$. Other dark energy models give a time-varying equation of state of dark energy.

We need statistical techniques and different observational datasets to distinguish one model from the other. Statistical techniques are also used to predict and infer from observational datasets. The SNIa observations give us the distance information of different supernovae upto redshift $z = 2.6$ [59]. The cosmic chronometer distance gives us the value of different Hubble parameter redshift values upto $z = 2.35$ [60–64]. In the case of Hubble parameter dataset we use different differential age techniques to find the value of Hubble parameter in a particular redshift. Along with Hubble parameter and supernovae datasets we also have Cosmic Microwave Background(CMB) and Baryon Acoustic Acceleration(BAO) datasets, which are used in the cosmological parameter estimation. In recent time the weak gravitational lensing data emerged as another observational tool to understand the dark sector of the Universe. Weak gravitational lensing is the perturbative distortion of the images of distant objects due to gravitational deflection of light. It gives us the way to understand the distribution of matter in the Universe, and as the dynamical dark energy and neutrino masses affect the growth of the structure, the weak lensing data contains the valuable information regarding the dark constituents of the Universe [65–69]. Again, the expression of the dispersion measures(DM) of Fast Radio Burst(FRB)s contain the cosmological parameters. Therefore, DM measurements is a potential tool to constrain the cosmological parameters and can be used mainly to break the degeneracy of the cosmological parameters [70–72].

Dark energy study is facilitated with sophisticated qualitative models which

can give exact accurate predictions. Also, the increasing availability of precise and large dataset helps in constraining these models. Along with these two aspects another aspect which revolutionized the cosmological parameter fitting is the deployment and advancement of statistical techniques, which helps in inference from the dataset. With the availability of the large datasets, we also need the precise measurements of the model parameters. Precision requires that we have sufficient knowledge of the error bars of the data set, which may be an error function or the errors for each measurement. There are four main applications of statistics in cosmology [73]. These are hypothesis testing, parameter estimation, model testing and forecasting. In the case of hypothesis testing, we deal with testing a null hypothesis in the presence of an alternative hypothesis, and finally quantifying the goodness of the hypothesis. Hypothesis may be an idea on the dynamics of the Universe or an idea about the errors of a particular experimental set-up. Parameter estimation basically quantifies a model in the presence of the experimental dataset in hand. It specifies the range of the parameter value if the dataset is present. Model testing is a way to select one model over the other. This may be done by checking and comparing the allowed parameter ranges of the model parameters or may be done by calculating the complexity of each model. This is also done in the presence of the observational dataset. The forecast part is useful to suggest future data points for the new observational measurements.

In the following chapters we begin with a discussion of General Theory of Relativity and cosmology. After a brief explanation on different distance measurements in cosmology, we discuss different statistical techniques used in cosmology which are relevant to the work presented in the thesis.

1.2 General Theory of Relativity and the Expanding Universe

We study the Universe based on the assumption that the Universe is homogeneous and isotropic on a large scale. There are justifications for treating the distribution of matter as homogeneous for scales larger than around 100 Mpc. This assumption of homogeneous and isotropic nature of the Universe is called the cosmological principle. It also singles out a particular class of observer, called the fundamental observer, for which the Universe appears to be isotropic. Any other observer who is moving with uniform velocity with this class of observer finds the universe to be anisotropic. The line element, which is the gen-

eral spacetime interval, contains the information of spacetime geometry. General Theory of Relativity(GTR) connects this line element to the energy content of the Universe and this is done by the Einstein field equation of gravitation. The line element for a homogeneous and isotropic Universe is given by the Friedmann–Lemaître–Robertson–Walker(FLRW) metric

$$ds^2 = g_{\mu\nu}dx^\mu dx^\nu = -dt^2 + a^2(t)d\sigma^2 \tag{1.1}$$

Here, $g_{\mu\nu}$ is the 'metric tensor', with $\mu, \nu = 0, 1, 2, 3$. Eqn(1.1) gives the distance between two spacetime points, and hence it contains the information of the geometry of spacetime. In the above equation, $a(t)$ is the scale factor with the cosmic time(t), and $d\sigma^2$ is the time-independent metric of the 3-dimensional space with constant curvature K. This is given by,

$$d\sigma^2 = \lambda_{ij}dx^i dx^j = \frac{dr^2}{1 - Kr^2} + r^2(d\theta^2 + sin^2\theta d\phi^2) \tag{1.2}$$

Here, $K = -1, 0, 1$ correspond to an open, flat, and closed universe. This metric represents the Friedmann-Lemaitre-Robertson-Walker(FLRW) spacetime. The indices, $i, j = 1, 2, 3$ and we have used the polar coordinates (r, θ, ϕ).

The curvature of spacetime is quantified by the Ricci tensor, which is given as

$$R_{\mu\nu} = \Gamma^\alpha_{\mu\nu,\alpha} - \Gamma^\alpha_{\mu\alpha,\nu} + \Gamma^\alpha_{\mu\nu}\Gamma^\beta_{\alpha\beta} - \Gamma^\alpha_{\mu\beta}\Gamma^\beta_{\alpha\nu} \tag{1.3}$$

Contraction of this tensor gives us the Ricci scalar, which is the curvature of a manifold.

$$R = g^{\mu\nu}R_{\mu\nu} \tag{1.4}$$

Einstein field equation are given by,

$$G^\mu_\nu = 8\pi G T^\mu_\nu, \tag{1.5}$$

where $G_{\mu\nu} = R_{\mu\nu} - \frac{1}{2}g_{\mu\nu}R$ is the Einstein tensor. Like any other field equation, it connects the effect of a field with its cause or the source term. Eqn(1.5) connects

the effect of the gravitational field with the source of gravity, which is the term given by the energy-momentum tensor ($T_{\mu\nu}$).

The energy-momentum tensor of the Einstein equation 1.5 is given by the equation of a perfect fluid as,

$$T^{\mu}_{\nu} = (\rho + p)u^{\mu}u_{\nu} + p\delta^{\mu}_{\nu} \tag{1.6}$$

where $u^{\mu} = (-1, 0, 0, 0)$ is the four-velocity of the perfect fluid in the comoving coordinates, while both ρ and p are functions of t. The components of T^{ν}_{μ} are $T^{0}_{0} = -\rho$ and $T^{j}_{i} = p\delta^{i}_{j}$. The Hubble parameter H is defined as,

$$H \equiv \frac{\dot{a}}{a} \tag{1.7}$$

where the dot represents derivative with respect to time. For the FLRW metric, the Einstein equation eqn(1.5), lead to the Friedmann equations

$$H^2 = \frac{8\pi G}{3}\rho - \frac{K}{a^2} \tag{1.8}$$

$$3H^2 + 2\dot{H} = -8\pi G p - \frac{K}{a^2} \tag{1.9}$$

Combining these two equations we have

$$\frac{\ddot{a}}{a} = -\frac{4\pi G}{3}(\rho + 3p) \tag{1.10}$$

If $(\rho + 3p) < 0$ the expansion of the Universe accelerates.

After combining eqn(1.8) and eqn(1.10) we get,

$$\dot{\rho} + 3H(\rho + p) = 0 \tag{1.11}$$

The equation of state (w)

$$w \equiv \frac{p}{\rho} \tag{1.12}$$

From eqn(1.10) we can see that the value of w determines whether the Universe is undergoing a decelerated expansion or an accelerated expansion. Therefore, Universe is accelerating or decelerating if $w < -1/3$ or $w > -1/3$.

From the continuity equation eqn(1.11) we can write,

$$\rho \propto a^{-3(1+w)} \tag{1.13}$$

For the cosmological constant $w = -1$ i.e. $p = -\rho$, and in this case eqn(1.11) gives that ρ is constant. From eqn(1.8) we see that for a constant ρ, for a flat Universe ($K = 0$), the scale factor will evolve exponentially: $a \propto exp(Ht)$.

We can write the eqn(1.8) in the form,

$$\Omega_M + \Omega_K = 1 \tag{1.14}$$

$$where, \qquad \Omega_M \equiv \frac{8\pi G\rho}{3H^2}, \qquad \Omega_K \equiv -\frac{K}{(aH)^2} \tag{1.15}$$

Inserting the relativistic matter, non-relativistic matter and dark energy as the energy components, namely ρ_R, ρ_M, ρ_{DE}, in the total energy of a flat Universe we get,

$$\rho_{total} = \rho_R(a) + \rho_M(a) + \rho_{DE}(a) \tag{1.16}$$

For non-relativistic matter pressure is negligible, hence $w = 0$ and we can get from eqn(1.13) $\rho_M \propto a^{-3}$. For relativistic matter $w = 1/3$ and we get $\rho_r \propto a^{-4}$. As discussed above for the vacuum energy, $p = -\rho$ and ρ_Λ is constant.

Then, from eqn(1.16) we get,

$$\frac{\dot{a}^2 + K}{a^2} = H_0^2[\Omega_{R0}a^{-4} + \Omega_{M0}a^{-3} + \Omega_{\Lambda 0}] \tag{1.17}$$

Here, H_0 is the Hubble constant, which is the present-day value of the Hubble parameter and the parameters Ω_{M0}, Ω_{R0}, $\Omega_{\Lambda 0}$ are the present-day values of non-relativistic matter, relativistic matter and dark energy density respectively. The subscript '0' to denote the present-day value of the energy density. We can write the cosmological parameters as,

$$\Omega_{R0} = \frac{8\pi G}{3H_0^2}\rho_{R0},\ \ \Omega_{M0} = \frac{8\pi G}{3H_0^2}\rho_{M0},\ \ \Omega_{\Lambda 0} = \frac{8\pi G}{3H_0^2}\rho_{\Lambda 0} \tag{1.18}$$

For curvature if we define, $\Omega_{K0} = -K/(a_0 H_0)^2$, from eqn(1.17) we will get,

$$\frac{\dot{a}^2}{a^2} \equiv H^2 = H_0^2 \left(\Omega_{R0}\frac{a_0^4}{a^4} + \Omega_{M0}\frac{a_0^3}{a^3} + \Omega_{K0}\frac{a_0^2}{a^2} + \Omega_{\Lambda 0} \right) \tag{1.19}$$

The 5 year WMAP [74–76] and the recent PLANCK [77] data suggested that the value of Ω_{K0} is nearly zero (95% confidence range for Ω_{K0} was given as $-0.0175 < \Omega_{K0} < 0.0085$). We can safely assume the value of the curvature parameter as $\Omega_{K0} = 0$, i.e. the Universe is spatially flat. From eqn(1.8) we see that $\Omega = \Omega_R + \Omega_M + \Omega_\Lambda = 1$. It is clear from eqn(1.19) that there is a singularity at $t = 0$ and that different species dominate different eras of the Universe. As the equation of the value of the state parameter for the radiation and matter are 1/3 and 0 respectively, the universe went through a decelerating phase ($\ddot{a} < 0$). Unless the Universe is exactly flat from the start, i.e. $K = 0$, the curvature part would dominate the contribution of other energy budgets of the Universe. In the present era, when the energy budget of the Universe is dominated by the energy component having a negative pressure component, the Universe can go to an accelerating phase.

1.3 Hubble law

The Hubble law connects the observed wavelength of a distant galaxy to the wavelength in the rest frame [78]. The observed wavelength is larger than the rest frame wavelength; this indicates the first observational proof of an expanding Universe. To quantify this effect, we introduce the redshift z,

$$z \equiv \frac{\lambda_0}{\lambda} - 1 = \frac{a_0}{a} - 1 \tag{1.20}$$

Here, λ_0 is the observed wavelength of a galaxy and λ is the wavelength in its rest frame. For $v << c$, $\lambda_0 \approx (1 + v/c)\lambda$, which implies $z \approx v/c$. If the physical distance between an observer and an object is denoted by $\mathbf{r}$, then we can write $\mathbf{r} = a(t)\mathbf{x}$, where $\mathbf{x}$ is the comoving distance. $\mathbf{x}$ remains constant for two points in the Hubble flow. Differentiating the expression of r,

$$\dot{\mathbf{r}} = H\mathbf{r} + a\dot{\mathbf{x}} \tag{1.21}$$

In the eqn(1.21), $H\mathbf{r}$ appears for the Hubble expansion, whereas $\upsilon_{\mathbf{p}} \equiv a\dot{\mathbf{x}}$ is the peculiar velocity of the object with respect to the Hubble flow. Along the line of sight, the speed of the object is,

$$\upsilon \equiv \dot{\mathbf{r}} \cdot \mathbf{r}/r = Hr + \upsilon_{\mathbf{p}} \cdot \mathbf{r}/r \tag{1.22}$$

where, $r \equiv |\mathbf{r}|$. When $\upsilon_{\mathbf{p}} \cdot \mathbf{r}/r \approx 0$ we can recover the classical Hubble law from eqn(1.22) as, $\upsilon \approx H_0 r$, H_0 being the Hubble constant.

1.4 Distance measurements and Cosmological datasets

In this section, we discuss different distance measurements. We start with the expression of the three-dimensional line element of eqn(1.1). From eqn(1.2) we get for $r = \sin\xi$ (K = +1), $r = \xi$ (K = 0) and $r = \sinh\xi$ (K=-1),

$$d\sigma^2 = d\xi^2 + (f_K(\xi))^2(d\theta^2 + sin^2\theta d\phi^2) \tag{1.23}$$

$$f_K(\xi) = \begin{cases} \sin(\xi), & (K = +1), \\ \xi, & (K = 0), \\ \sinh(\xi), & (K = -1). \end{cases} \tag{1.24}$$

1.4.1 Comoving distance

Light ray traveling along x direction satisfies the geodesic equation, $ds^2 = 0$ and we can write $dx = -cdt/a(t)$. The comoving distance is then given by,

$$d_c \equiv x_1 = \int_0^{x_1} dx = -\int_{t_0}^{t_1} \frac{c}{a(t)} dt \tag{1.25}$$

Here, we assume that light is emitted at $t = t_1$, with $x = x_1$. Eqn(1.20) can be reduced to $dt = -dz/[H(1+z)]$ and in terms of redshift z we can write the

comoving distance as

$$d_c = \frac{c}{a_0 H_0} \int_0^z \frac{dz'}{\mathcal{E}(z')} \tag{1.26}$$

where, $\mathcal{E}(z) \equiv H(z)/H_0$. After expanding the function $\int_0^z d\tilde{z}/\mathcal{E}(\tilde{z})$ about $z = 0$, we get

$$\int_0^z \frac{d\tilde{z}}{\mathcal{E}(\tilde{z})} = z - \frac{\mathcal{E}'(0)}{2} z^2 + \frac{1}{6}\left\{2\mathcal{E}'(0)^2 - \mathcal{E}''(0)\right\} z^3 + \mathcal{O}(z^4), \tag{1.27}$$

prime in here represents the derivative with respect to the redshift z. For a redshift $z << 1$, we can write

$$d_c \approx \frac{c}{a_0 H_0} z \tag{1.28}$$

$$\upsilon \approx (a_0 H_0) d_c \tag{1.29}$$

Eqn(1.29) is derived using eqn(1.28) and eqn(1.22). υ is the recession velocity and we can write the physical distance $r = a_0 d_c$ as, $r \approx (c/H_0)z \approx \upsilon/H_0$. Therefore, for low redshift the relation of the physical distance is the familiar Hubble law.

1.4.2 Luminosity distance

The luminosity distance to supernova encodes information about the expansion rate of the Universe. Through the comparison of apparent luminosities of supernova type Ia, in different redshifts we obtain the value of the luminosity distance d_L.

Between two observers at different points separated by the proper distance δl and the comoving length difference δx, we can write $\delta l = a(t)\delta x$ and the velocity attribute due to the expansion of spacetime is

$$\delta\upsilon = \frac{d}{dt}\delta l = \dot{a}\delta x = H\delta l \tag{1.30}$$

Let us consider that at one of these points there is a source of electromagnetic radiation, and at another there is an observer. If the frequency of the electromagnetic radiation is ω, the observer at the other point measures the frequency at the

Doppler sifted frequency $(\omega + \delta\omega)$, where

$$\frac{\delta\omega}{\omega} = -\delta\upsilon = -\frac{\dot{a}}{a}\delta l = -\frac{\dot{a}}{a}\delta t = -\frac{\delta a}{a} \tag{1.31}$$

For two infinitesimally close points we can apply the laws of special theory of relativity. Eqn(1.31) can be integrated to,

$$\omega(t)a(t) = \text{constant} \tag{1.32}$$

For a material particle, we can also write the effective velocity equation. Let two observers are situated δl proper distance away and a material particle passes the first observer with velocity υ. Then, the velocity of the second observer, relative to the first one when the material particle passes is

$$\delta u = \frac{\dot{a}}{a}\delta l = \frac{\dot{a}}{a}\upsilon dt = \upsilon\frac{\delta a}{a} \tag{1.33}$$

If the second observer attributes υ' velocity to the particle, we can write,

$$\upsilon' = \frac{\upsilon - \delta u}{1 - \upsilon\delta u} = \upsilon - (1 - \upsilon^2)\upsilon\frac{\delta a}{a} \tag{1.34}$$

$$\delta\upsilon = -\upsilon(1 - \upsilon^2)\frac{\delta a}{a} \tag{1.35}$$

By integrating eqn(1.35) we get, $p = constant/a$, indicating that the velocity is decreasing as a^{-1}.

Assume a pencil of light that is emitted by one source observer and received by another. If for a comoving observer, there is $d\mathcal{N}$ number of photons in a volume of $\mathcal{V}$, which have the momentum range $(\mathbf{p}, \mathbf{p} + \mathbf{d^3p})$, we can write

$$d\mathcal{N} = f d\mathcal{V} d^3p$$

Here, $f(\mathbf{x}, \mathbf{p}, t)$ is the phase space distribution function. This expression is true for all species of matter particles, including photons. As the phase space density of photons is conserved, $f_\gamma(t, d^3\mathbf{x}, d^3\mathbf{p})$ is invariant during the propagation of the light beam between two observer. Therefore, we can write

$$f_\gamma(t, \mathbf{x}, \mathbf{p}) = \frac{d\mathcal{N}}{d^3\mathbf{x}d^3\mathbf{p}} = \frac{d\mathcal{N}_\gamma}{dtdAd\omega d\Omega}\frac{1}{\omega^2} = \text{invariant} \tag{1.36}$$

Here, $d^3\mathbf{p} \propto p^2 dp d\Omega \propto \omega^2 d\omega d\Omega$ and $d^3\mathbf{x} \propto cdtdA$. $d\Omega$ is the solid angle and dA is the area perpendicular to the propagation of the radiation. As, $dE = \hbar\omega d\mathcal{N}$ and intensity is $I = (dE/dtdAd\omega d\Omega)$ we get,

$$\frac{I}{\omega^3} = \text{invariant} \tag{1.37}$$

If $\mathcal{F}$ is the flux received from a source at distance $r = r_{em}$ and $\mathcal{L}$ is the luminosity we can express,

$$\mathcal{F} = \frac{1}{\text{area}}\frac{dE_{rec}}{dt_{rec}} \tag{1.38}$$

$$= \frac{1}{4\pi a_0^2 r_{em}^2 (1+z)^2}\mathcal{L} \tag{1.39}$$

In the above equations the subscript 'rec' is for the receiving observer and 'em' is for the source. In eqn(1.39) $\mathcal{L}$ is the luminosity distance of the source.

As luminosity is one of the observables, and the distance to an object can be written with the help of flux $\mathcal{F}$ and luminosity $\mathcal{L}$. If we can write,

$$d_L(z) = \left(\frac{\mathcal{L}}{4\pi\mathcal{F}}\right)^{1/2} = a_0 r_{em}(z)(1+z) = a_0(1+z)\mathcal{S}_\kappa \tag{1.40}$$

where, $\mathcal{S}_k$ is the same function defined in eqn(1.24).

1.4.3 Angular diameter distance

If Δl is the physical length of an object orthogonal to the line of sight of an observer's position, and if the object subtends an angle $\Delta\theta$ at the observer, for a smaller value of $\Delta\theta$ we can write $\Delta l = r_{em}a(t_e)\Delta\theta$. We denote angular distance, from the source to the receiver as d_A then we will get $\Delta\theta = \Delta l/d_A$. Therefore,

$$d_A(z) = r_{em}a(t_e) = a_0 r_{em}(1+z)^{-1} \tag{1.41}$$

Eqn(1.41) eventually give us,

$$d_A = \frac{d_L}{(1+z)^2} \tag{1.42}$$

Eqn(1.42) is popularly known as duality or reciprocity of the Ethergington relation.

In the fig(1.1), we see that for the model of a flat Universe where matter and dark energy matter species are considered, the luminosity and angular diameter distance increase monotonically for the low redshift and after that d_A starts decreasing. We also see that, for a particular redshift, the value of d_L decreases, as Ω_M increases. This is also true for d_A.

1.5 Observational Datasets

In this section we will discuss the observational dataset used in our work, namely the supernova type Ia dataset and the Hubble parameter or cosmic chronometer dataset.

1.5.1 Supernovae Type Ia

Supernovae are characterized by its peak brightness that is associated with an exploding star. These are one of the most violent explosions of the Universe, which releases nearly 10^{44} J of energy at a timescale of about a second from a region of planetary size. This outshines all stars of the galaxy at their maximum brightness [79]. Supernovae Type Ia(SNIa) are the results of the explosion of a carbon-oxygen white dwarf in a binary system as it goes beyond the Chandrasekhar limit, either due to accretion from a donor or mergers. These are called the standard candles of the Universe. A type Ia supernova is identified by its light-curve, where the presence of spectral line for Silicon or Calcium is significant but not the spectral lines of Hydrogen or Helium. The light curves of different SNIa are not the same but similar, and the empirical methods that depend only on observations allow these different light curves to collapse into a single curve.

From the SNIa discovered by the Pan-STARRS1 (PS1) Medium Deep Survey pantheon dataset ([80, 81]) gives light-curves of more than a thousand SNIa, which gives distance modulus μ values at 1048 different redshifts. The last two decades marked different supernovae surveys, which probe a large range in redshift. CfA1-

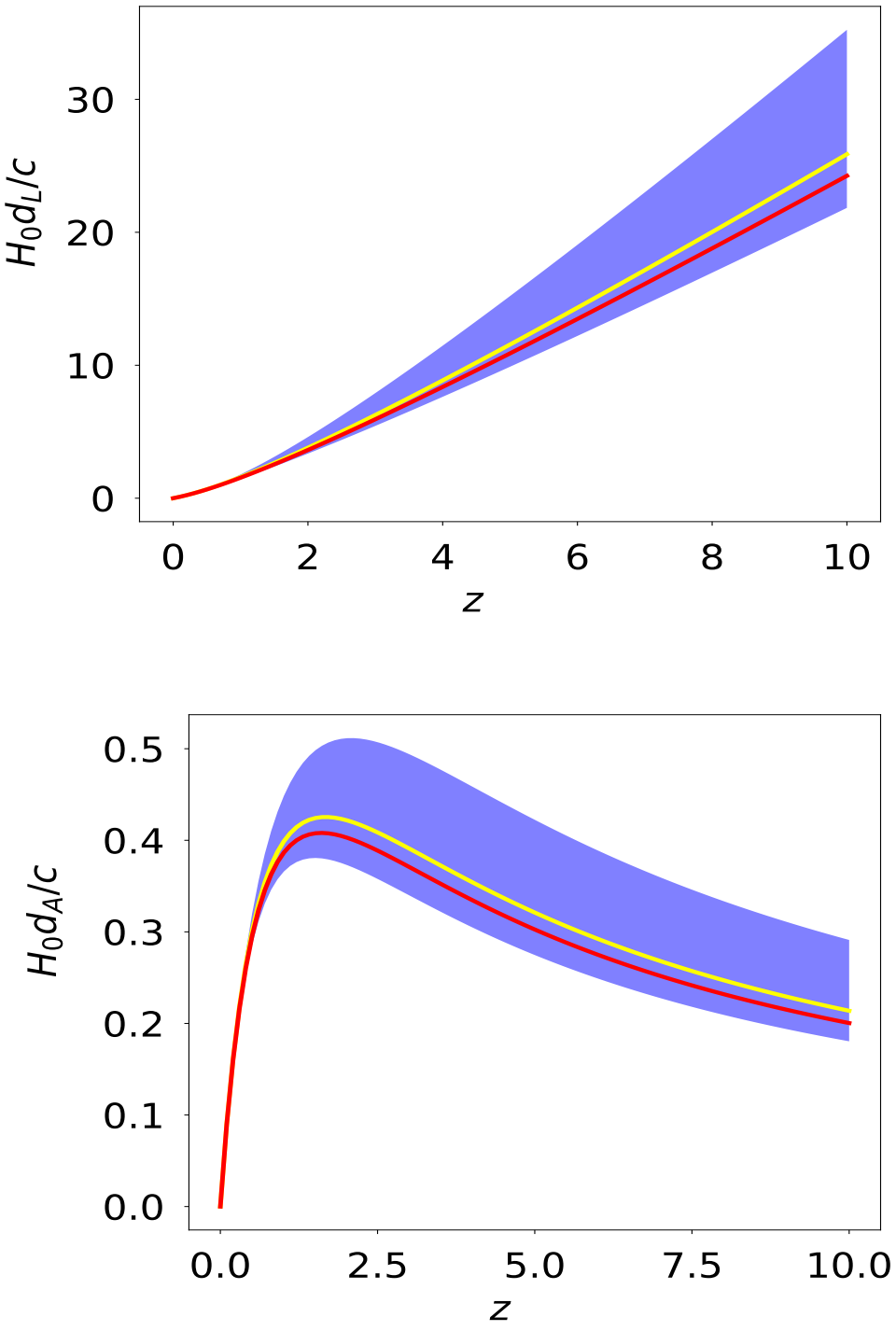

Figure 1.1: The plots in the figure shows the evolution of luminosity distance and angular diameter distance. In the figures we plot for a specially flat Universe, where only two components of matter have been consider, matter and dark energy. Red and yellow curves are for $\Omega_M = 0.25$ and $\Omega_M = 0.3$ respectively. The blue region shows the variation of Ω_M from 0.1 to 0.4.

CfA4 [82–84] CSP [85–87] LOSS [88] assembled large sets of low-redshift ($0.01 < z < 0.1$) SNe. Fro $z > 0.1$ reshift there are many overlap surveys ESSENCE [89–91], SNLS [92, 93], SDSS [94–96] and PS1 [97, 98] Now we also have high redshift data from the SCP survey [99] as well as the GOODS [100, 101] and DELS/CLASH surveys [102–104].

The pantheon compilation [80, 81] gives the value of the distance modulus μ as

$$\mu = m_B - M + \alpha_x - \beta c + \Delta_M + \Delta_B \tag{1.43}$$

where Δ_M and Δ_B are the distance correction based on the host-galaxy mass of the SN and the distance correction based on the predicted biases of the simulations, respectively. α and β are the coefficients of relation between luminosity and stretch and between luminosity and color, respectively. M is the absolute B-band magnitude of a fiducial SNIa with $x = 0$ and $c = 0$.

From [80, 81], we can write the error in the total distance of each SNIa as

$$\sigma^2 = \sigma_N^2 + \sigma_{Mass}^2 + \sigma_{\mu-z} + \sigma_{lens}^2 + \sigma_{int}^2 + \sigma_{Bias}^2 \tag{1.44}$$

In eqn(1.44), σ_N^2 is the photometric error, Uncertainty due to mass step correlation and distance bias corrections are as σ_{Mass}^2 and σ_{Bias}^2. The uncertainty from the peculiar velocity uncertainty and redshift measurement uncertainty in quadrature is given as $\sigma_{\mu-z}$, whereas σ_{lens}^2 is the uncertainty of stochastic gravitational lensing. σ_{int}^2 is for the intrinsic scatter.

The theoretical value of μ is calculated as follows.

$$\mu = 5 \log_{10} \left(\frac{d_L}{1\text{MPc}} \right) + 25 \tag{1.45}$$

1.5.2 Hubble parameter dataset

We also use the cosmic chronometer measurements, which consists of the tabulated 38 data points of values $H(z)$ versus z [60–64, 105–114].

Direct measurement of the Hubble parameter is a powerful tool to constrain the cosmological parameter of a theory, which can be seen from the Friedman equation 1.19. The differential age method is used to measure the Hubble parameter at

different redshifts. We can see from eqn(1.45) that to constrain the dark energy Equation of State parameter(EoS) from the distance modulus measurement we have to go through the process of integration, eqn(1.40). The differential age method gives us the way to bypass the integration [115].

To find the value of Hubble parameter, we have to rely on a clock that dates the variation in the age of the Universe with redshift. For the differential age method, this clock is the spectroscopic dating of galaxy ages. Two passively evolving galaxies are chosen that formed at the same time but separated by a small redshift interval δz such that the derivative dz/dt can be assumed as $\delta z/\delta t$, here $t(z)$ is the age of the Universe at redshift z. To improve the statistical significance we have to select a fair sample of passively evolving galaxies at the two redshift points. After selecting the galaxy pairs, we compare the upper cut-offs in their age distributions. All selected galaxies must have similar metallicities, and we have to ensure that the average age of their stars is much greater than the age difference of the two galaxies.

Through the differential age method, we calculate dz/dt for different redshifts z, from which we can calculate the Hubble parameter $H(z)$ as

$$H(z) = -\frac{1}{(1+z)}\frac{dz}{dt} \tag{1.46}$$

This differential age determination is more reliable than the absolute age determination of galaxies [116, 117].

1.6 Statistical methods - A brief review

Classical statistics comprises of three steps:

- Formulation of a hypothesis using prior knowledge of the system under study.
- collecting and recording of the hypothesis-test data via experiments
- the construction of a test hypothesis.

Making a decision on the basis of test statistics requires that, one has to know the sampling distribution or expectations of the statistics. Typically, one has

to know the frequency distribution of the test statistics to validate the final result. This poses a problem, as in astronomy we deal with very small sample size, and astronomers can not control or rerun "the experiment". This poses a poor assumption of the underlying distributions. Therefore, the process of extracting information from observed data is incorporated with the statistics. Statistical techniques are used in error estimation, finding correlation between the data points, extracting information from the incomplete dataset, and finally in the process of decision making. Development of astronomical ideas or the cosmological ideas in particular, can be defined in the following categories.

- Observation
- Data reduction
- Analysis
- Inference
- Update Knowledge for the theoretical model

Observation is the process of collecting and recording data from the Universe. In the data reduction, we reduce the noise and the unwanted data part from the collected dataset. Different statistical techniques of data reductions are used in this noise cancellation part. In the analysis part we use different statistical techniques to infer prior knowledge or theory. Calculation of statics is also included in this step. Statics are those quantities that summarize the data; it is the ultimate form of data reduction. According to the dataset at hand, mean, median, or standard deviation may be the statics of the dataset. After the analysis, we can compare different models that hitherto existed. The concluding remarks after the analysis quantifies the significance of a model. Inference tells us if the results are not plausible then at which stage we have to re-check the experimental data. The next step is the update of our knowledge for modification of our idea or theory. This development is a two-way process and after getting inference from experiments and the required modification, the developed theory has the potential to predict the future data points. For these future data-points the experiment has to be conducted again.

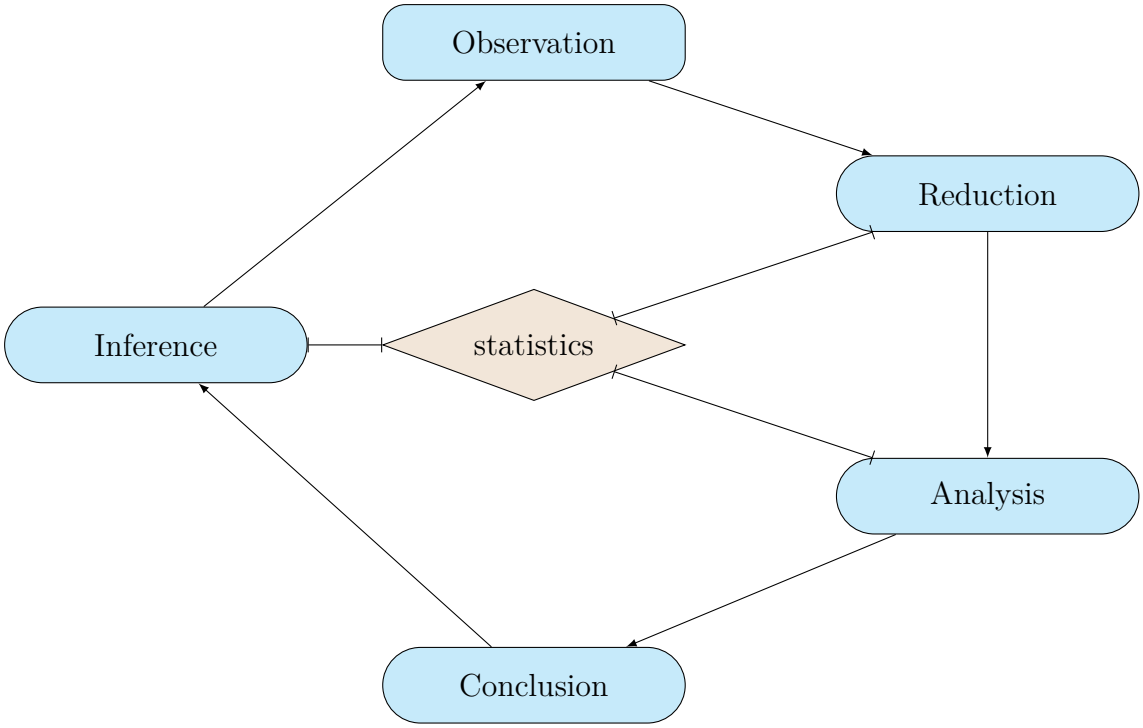

For an astronomical experiment, this spiral development is defined by [118]. This is the process of development of both theory and experimental methods. Experiments collect raw data, and the process of reduction cleans up the experimental effect.

In the following section, we give a brief description of some of the most widely used statistical methods and techniques that we use in our work.

1.7 Bayesian model selection and Inference of the parameters

Selection of one correct cosmological model from the set, which consistent with observation is one of the principal goals of cosmology [119]. Theoretical models are quantified by the respective theoretical model parameters. Selection of correct or a best-suited model with the observation is a two-step process. First, we determine the allowed theoretical range of the parameters, and then we attach a distribution with the parameters. Range of the parameters is the prior information we need in the model selection process, and in the light of the Bayesian approach, probability distribution assigned to the parameters are called prior probabilities. The combination of parameter set and prior distribution is called *model*; which contains information of the theoretical and statistical prior input. The second step

is the comparison of the theoretical model with the observation, which quantifies the allowed range of parameters.

1.7.1 Bayes' theorem

To infer a theory, we need both the multidimensional theoretical model parameters $\vec{\theta}$ as well as the observational dataset $\mathcal{D}$. We can think of $\vec{\theta}$ and $\mathcal{D}$ as two methods to create the data-points, and $\mathcal{P}(\dots)$ is the *valuation* that gives the probability of that particular method. We can compile the necessary characteristics of the probability as follows,

$$\left.\begin{array}{rcrcr} \mathcal{P}(\vec{\theta}) & \geq & 0 & \longrightarrow & \textit{positivity} \\ \int \mathcal{P}(\vec{\theta}) d\vec{\theta} & = & 1 & \longrightarrow & \textit{sum rule} \\ \mathcal{P}(\vec{\theta} \cap \mathcal{D}) & = & \mathcal{P}(\mathcal{D}|\vec{\theta})\mathcal{P}(\vec{\theta}) & \longrightarrow & \textit{product rule} \end{array}\right\} \tag{1.47}$$

From eqn(1.47), the product rule of two joint probability of a model parameter set $(\vec{\theta})$ and data $(\mathcal{D})$ can be given as

$$\left.\begin{array}{rcrcr} \mathcal{P}(\vec{\theta})\mathcal{P}(\mathcal{D}|\vec{\theta}) & = & \mathcal{P}(\vec{\theta} \cap \mathcal{D}) & = & \mathcal{P}(\mathcal{D})\mathcal{P}(\vec{\theta}|\mathcal{D}) \\ \textit{Prior} \times \textit{Likelihood} & = & \textit{Joint} & = & \textit{Evidence} \times \textit{Posterior} \\ \pi(\vec{\theta})\mathcal{L}(\mathcal{D}|\vec{\theta}) & & = & & \mathcal{E}\Pi(\vec{\theta}|\mathcal{D}) \end{array}\right\} \tag{1.48}$$

To define the individual elements of Bayes' Theorem, we follow the nomenclature of [119]. Prior probability$(\pi(\vec{\theta}))$ represents the information of our parameter distribution. Likelihood$(\mathcal{L}(\mathcal{D}|\vec{\theta}))$ is the probability distribution of the dataset for allowed input of the parameters. Posterior probability is the inferred distribution of probability after we have the dataset. Evidence is the representation of how well our previous assignment was able to predict the data. Evidence is also called 'marginalized likelihood'. We can summarize the above calculation of inference in three equations given by,

$$\int \pi(\vec{\theta}) d\vec{\theta} = 1 \tag{1.49}$$

$$\mathcal{E} = \int \pi(\vec{\theta}) \mathcal{L}(\mathcal{D}|\vec{\theta}) d\vec{\theta} \tag{1.50}$$

$$\mathcal{P}(\vec{\theta}) = \frac{\pi(\vec{\theta}) \mathcal{L}(\mathcal{D}|\vec{\theta})}{\mathcal{E}} \tag{1.51}$$

The difference between the prior and the posterior is the information;

$$\mathcal{H}(\Pi|\pi) = \int \Pi(\vec{\theta}|\mathcal{D}) \log(\Pi(\vec{\theta}|\mathcal{D})/\pi(\vec{\theta})) d\vec{\theta} \tag{1.52}$$

1.7.2 Bayesian model selection

Bayesian parameter estimation is a framework for model comparison or model selection. Rather than singling out a particular model, we compare competing models, which explain the observed outcome through different physical processes. The typical use of the Bayesian methods is in the estimation of the allowed parameter values of a model. After selection of a correct model, we want to know the allowed range of the parameters given the data. We decide the range of parameters that are needed in the model to explain the observed data. As every model explains the observed data through some physical processes we would like to know which are the physical processes that affect our observed data. Therefore, the model comparison or model selection is the way to get to this goal. This is done by computing posterior probability. From eqn(1.48) we can see that the posterior probability is proportional to the likelihood. Bayesian inference gives the acceptable range of parameter estimation.

As we have seen from the equations eqn(1.50, 1.51) of sec(1.7.1) to predict the posterior probability of the parameters, we have to calculate the likelihood $\mathcal{L}(D|\vec{\theta})$, which also depends on our previous belief represented by $\pi(\vec{\theta})$. If now we assume that our probabilities are conditioned on our assumed model, then we have to modify eqn(1.48) to get the posterior probability of parameter set $\vec{\theta}$ as

$$\mathcal{P}(\vec{\theta}|\mathcal{D}, \mathcal{M}) = \frac{\mathcal{P}(\mathcal{D}|\vec{\theta}, \mathcal{M}) \mathcal{P}(\vec{\theta}|\mathcal{M})}{\mathcal{P}(\mathcal{D}|\mathcal{M})} \tag{1.53}$$

In eqn(1.53), $\mathcal{P}(\mathcal{D}|\mathcal{M})$ is the likelihood of the data given the model, which is

also known as Bayesian evidence. Rewriting the Bayesian posterior probability of the model, we get

$$\mathcal{P}(\mathcal{M}|\mathcal{D}) = \frac{\mathcal{P}(\mathcal{D}|\mathcal{M})\mathcal{P}(\mathcal{M})}{\mathcal{P}(\mathcal{D})} \tag{1.54}$$

In eqn(1.54) we can see that the Bayesian evidence term $\mathcal{P}(\mathcal{D}|\mathcal{M})$ appears. The model selection needs to compute only the value of $\mathcal{P}(\mathcal{M}|\mathcal{D})$, which depends on the Bayesian evidence and the prior probability distribution of the model $\mathcal{P}(\mathcal{M})$. For our convenience we take a flat prior. To get an expression of Bayesian evidence term, we use eqn(1.53) and integrate over all possible values of $\vec{\theta}$, which will make the left hand side of eqn(1.53) unity.

$$\left.\begin{aligned} \mathcal{P}(\mathcal{D}|\mathcal{M}) &= \int \mathcal{P}(\mathcal{D}|\vec{\theta},\mathcal{M})\mathcal{P}(\vec{\theta}|\mathcal{M})d\vec{\theta} \\ Evidence &= \int (Likelihood \times Prior) d\vec{\theta} \end{aligned}\right\} \tag{1.55}$$

From eqn(1.55) it is clear that evidence is the average likelihood of the parameters integrated over the prior parameter. Bayesian evidence gives us the model predictiveness as an output. For a particular model, if it fits the observational data well for most regions of the parameter space, then the average likelihood and finally the Bayesian evidence will be high. This leads to good predictiveness of that particular model. If the evidence is low, then it indicates that for some regions of the parameter space, the model poorly predicts the observed value. For a good predictive model, the desired observational quantity should not depend strongly on the model parameters. If we define the simplicity of the model by the number of parameters that it needs to calculate the observed quantity, then we can say that the predictivity of the model is closely connected with the simplicity of the model. It is because more number of parameters in the model leads to more diverse predictions.

1.7.3 Information Criteria

If we consider two models, $\mathcal{M}_0$ and $\mathcal{M}_1$ then the ratio of Bayesian evidence of these models is called the Bayes factor,

$$B_{01} \equiv \frac{\mathcal{E}_0}{\mathcal{E}_1} \tag{1.56}$$

Eqn(1.56) is a measure of predictiveness of one model over the other, when dataset is given. Therefore, if B_{01} is less than 1, we can say that the model $\mathcal{M}_1$ can agree with the data more than the model $\mathcal{M}_0$.

The comparison of models with a large number of parameters is a difficulty. The main hindrance comes in solving the integration of eqn(1.55) to calculate the evidence. In such a case, we use different information criteria. These information criteria depend on the maximum likelihood rather than the likelihood for the whole parameter range. Akaike information criteria(AIC) and Bayesian information criteria(BIC) are two of the most widely used information criteria, which are derived from the Gaussianity or near-Gaussianity of the posterior distribution [73, 120, 121]. The AIC and BIC for a model are defined as

$$AIC = -2ln(\mathcal{L}_{max}) + 2k$$
$$BIC = -2ln(\mathcal{L}_{max}) + klnN$$

where $\mathcal{L}_{max}$ is the maximum likelihood, k is the number of parameters of the model under consideration, and N is the number of data points. In case of parameter degeneracy the inclusion or rejection of an model parameter can be done by AIC and BIC.

When we have a certain model $\mathcal{M}$, data $\mathcal{D}$, a set of parameters $\vec{\theta}$ and a method to find out the probabilities of the model parameters from the dataset, we can find the possible value of the parameters with certain probability. This is called the parameter estimation, and one of the prominent way of parameter estimation is the Monte Carlo sampling.

1.7.4 Parameter estimation using Monte Carlo sampling

We start by collecting samples from the target population. Prior to the analysis we have the following components,

- a model based on the physical system we have
- observational data
- the model parameters, which quantify the physical system

- method for taking the sample from the population.

We can find the expectation value of any function $f(\vec{\theta})$ of the parameters $\vec{\theta}$ as,

$$\langle f(\vec{\theta})\rangle = \int d\vec{\theta} f(\vec{\theta})\mathcal{P}(\vec{\theta}) \tag{1.57}$$

In eqn(1.57), $\mathcal{P}(\vec{\theta}) = \mathcal{P}(\vec{\theta}|\mathcal{D},\mathcal{M})$, is the posterior probability. The computationally efficient method for performing this integration is to explore the parameter space by taking samples [119]. The probability of taking the sample is proportional to the posterior density $\mathcal{P}(\vec{\theta})$ of the parameter space at that point. Our motive is to calculate the full properties of the parameter space from the samples we have collected. We are interested in calculating $\mathcal{P}(f(\vec{\theta})|\{\vec{\theta}\})$ instead of $\mathcal{P}(f(\vec{\theta})|\mathcal{P}(\vec{\theta}))$. Central limit theorem states that for a sample of large size, the sum of any quantity calculated from different sample distributions tends to a normal probability distribution. We can estimate $\langle f(\vec{\theta})\rangle$ as

$$\hat{\mathcal{E}}_f = \frac{1}{n_s}\sum_{i=1}^{n_s} f(\vec{\theta}_i) \tag{1.58}$$

Here, $\vec{\theta}_i$ represents the ith sample from the parameter space and n_s the total number of collected samples. The law of large numbers states that the average of sample mean and standard deviation of a quantity approximate the actual mean and standard deviation of the targeted population. Therefore, the expectation of the function of the parameter is the true expectation $\langle\hat{\mathcal{E}}_f\rangle = \langle f(\vec{\theta})\rangle$. For the large number of samples, $\mathcal{P}(\hat{\mathcal{E}}_f)$ tends to the normal distribution $\mathcal{N}(\langle f(\vec{\theta})\rangle, \sigma_E^2)$, where $\sigma_E = \sigma_f/\sqrt{n_s}$ and σ_f^2 is the true variance of $f(\vec{\theta})$.

It is therefore computationally efficient to divide the posterior distribution in small samples. Below, we briefly describe some of the sampling techniques.

Direct sampling:

Rather than generating samples only asymptotically, these methods generate independent samples directly [119]. There are two distinct ways in this methodology.

In one case, the so called *inverse method*, we draw samples from the cumulative distribution $\mathcal{Q}(\vec{\theta})$ and then draw the corresponding value through the inverse calculation of probability density function (pdf) $\mathcal{P}(\vec{\theta})$. $\mathcal{Q}(\vec{\theta})$ is the monotonically

increasing function and for the pdf $\mathcal{P}(\vec{\theta})$, it is given as

$$\mathcal{Q}(\vec{\theta}) = \int_{-\infty}^{\theta} d\vec{\theta'}\mathcal{P}(\vec{\theta'}) \tag{1.59}$$

If we consider the one-dimensional case, first a random sample x_i is chosen from the uniform distribution of zero to one. We try to find θ_i for which $\mathcal{Q}(\theta_i) = x_i$. Then we sample $\mathcal{P}(\theta_i)$ with probability $\mathcal{P}(\theta_i)$.

In the second case, which is called the *accept-reject sampling method*, selecting an appropriate 'umbrella' or 'envelope' distribution $U(\vec{\theta})$ from which it is easy to sample. We take $U(\vec{\theta}) \geq \mathcal{P}(\theta)$ for all points in the parameter space $\vec{\theta}$. We keep a sample with probability $\mathcal{P}(\vec{\theta})/U(\vec{\theta})$ or reject otherwise. Samples selected in this are independent of each other.

Markovian sampling:

Direct methods of sampling are efficient in the one-dimensional parametric case. For multi-dimensional parameteric case, the method which is mostly used is the Markov chain method. If the probability to move from the current position of the parameter space $\vec{\theta_i}$ to the next point of the parameter space $\vec{\theta}_{i+1}$ depends only on the current position $\vec{\theta_i}$, then the process is called the Markovian process. The Markovian way to estimate the posterior probability $\mathcal{P}(\vec{\theta_i})$ is such that, after following a long Markov chain, the probability of arriving at the current position is same as the actual probability of the posterior distribution $\mathcal{P}(\vec{\theta})$. If we use the transition probability $T(\theta_{i+1}|\theta_i)$, to define the probability of moving from the position θ_i to θ_{i+1} then probability at the point θ_{i+1} is

$$\mathcal{P}(\theta_{i+1}) = \int d\theta_i \mathcal{P}(\theta_i) T(\theta_{i+1}|\theta_i) \tag{1.60}$$

The condition of transition depict in eqn(1.60) is ensured by the condition of detailed balance.

$$\mathcal{P}(\theta_{i+1})T(\theta_i|\theta_{i+1}) = \mathcal{P}(\theta_i)T(\theta_{i+1}|\theta_i) \tag{1.61}$$

The condition of detailed balance indicates that the probability of going from θ_i from θ_{i+1} is same as that of moving from θ_{i+1} to θ_i. The user has the freedom to choose the form of T. The only thing that needs to be taken into account when choosing T is that the transition probability should lead us to all the points of the parameter space.

Metropolis-Hasting algorithm:

Metropolis-Hasting [122, 123] is one of the Markovian methods which satisfies the condition of detailed balance. Due to its simplicity, it is one of the most popular methods. Metropolis-Hasting uses Bayes' Theorem sec(1.7.1) to calculate the posterior probability density from which sampling is difficult. It is a version of accept-reject method where we need an umbrella distribution, called the proposal distribution. This proposal distribution $q(\theta_{i+1}|\theta_i)$ gives the probability of getting to the point θ_{i+1} when the current position θ_i is given. The acceptance probability is

$$\alpha(\theta_{i+1}|\theta_i) = min\left\{1, \frac{\mathcal{P}(\theta_{i+1})q(\theta_i|\theta_{i+1})}{\mathcal{P}(\theta_i)q(\theta_{i+1}|\theta_i)}\right\} \tag{1.62}$$

Here,

$$r \equiv \frac{\mathcal{P}(\theta_{i+1})q(\theta_i|\theta_{i+1})}{\mathcal{P}(\theta_i)q(\theta_{i+1}|\theta_i)}$$

is called the Hasting ratio. For symmetric case, $q(\theta_i|\theta_{i+1}) = q(\theta_{i+1}|\theta_i)$ and expression of r reduce to $r \equiv \mathcal{P}(\theta_{i+1})/\mathcal{P}(\theta_i)$, which is the Metropolis ratio. We have the transition probability as

$$T(\theta_{i+1}|\theta_i) = \alpha(\theta_{i+1}|\theta_i)q(\theta_{i+1}|\theta_i) \tag{1.63}$$

This shows that eqn(1.63) satisfies the Markovian condition of detailed balance.

Hamiltonian(hybrid) Monte Carlo:

Hamiltonian Monte Carlo(HMC) is a modified form of the classical Metropolis-Hasting algorithm. It is designed to follow the Hamiltonian dynamics such that maximum part of the parameter space has been covered. Here with the regular variables(which in the Hamilonian Monte Carlo language called the position variable) we introduce an auxiliary field variable (called the momentum variable). Typically, these auxiliary variables have independent Gaussian distributions. Like the Metropolis-Hasting algorithm, this method falls into the broad category of acceptance-rejection algorithm.

If $\mathbf{q}$ and $\mathbf{p}$ are the position and the momentum variables, we have the Hamiltonian equations as

$$\frac{dq_i}{dt} = \frac{\partial H}{\partial p_i}$$
$$\frac{dp_i}{dt} = -\frac{\partial H}{\partial q_i}$$

Where, for HMC we write the Hamiltonian as $H(\mathbf{p}, \mathbf{q}) = U(\mathbf{q}) + K(\mathbf{p})$

While performing the HMC the properties of the Hamiltonian dynamics should be satisfied [124], which are

- *Reversibility*: We use this property to ensure that the target distribution is left invariant while the updates in the MCMC iterations.

- *Law of conservation*: While each update we have to ensure that the time derivative of the Hamiltonian should be zero. Here time variable basically represents the steps we have taken. In HMC the acceptance probability is one when the Hamiltonian is conserved.

- *Preservation of volume*: Following the Hamiltonian equations we obtain the preservation of volume in ($\mathbf{q}$, $\mathbf{p}$) space. Preservation of the phase-space volume is that the method explores a parameter space.

In HMC, the canonical distribution over the phase space has the following probability density function.

$$\mathcal{P}(\vec{\theta}) = \frac{1}{\mathcal{Z}} e^{-\beta H(\mathbf{p},\mathbf{q})} \tag{1.64}$$

Here, $\beta = 1/T$ is the usual inverse temperature, and $\mathcal{Z}$ is the partition function. Splitting eqn(1.64) in terms of potential and kinetic part, we have,

$$\mathcal{P}(\vec{\theta}) = \frac{1}{\mathcal{Z}} e^{-\beta U(\mathbf{q})} e^{-\beta K(\mathbf{p})} \tag{1.65}$$

Eqn(1.65) is the indication that both $\mathbf{q}$ and $\mathbf{p}$ are independent. The motive of introducing momentum variable is that when both $\mathbf{q}$ and $\mathbf{p}$ satisfy Hamiltonian dynamics, the chain will follow elliptical contours, which ensure exploration of a greater area in parameter space.

Leapfrog Method:

To solve the differential equations of Hamiltonian dynamics, we discretize the time variables. The simplest and most efficient way to do this is the Leapfrog method. If ϵ is the step size, then starting with the state at time zero, we can compute the steps ϵ, 2ϵ, 3ϵ iteratively. The following are the steps for the leapfrog method.

$$\left.\begin{aligned} q_i(t+\tfrac{1}{2}\epsilon) &= q_i(t) + \tfrac{1}{2}\epsilon p_i(t) \\ p_i(t+\epsilon) &= p_i(t) - \epsilon q_i(t+\tfrac{1}{2}\epsilon) \\ q_i(t+\epsilon) &= q_i(t+\tfrac{1}{2}\epsilon) + \tfrac{1}{2}\epsilon p_i(t+\epsilon) \end{aligned}\right\} \tag{1.66}$$

Eqn(1.66) summarize the leapfrog method. To change the state to t from $t+\epsilon$, we first update the position variable in a half step, starting with $q_i(t)$ and the momentum variable $p_i(t)$. Then we update the momentum variable $p_i(t)$ with the full step. Then we update the second half of the position variable with the help of updated position and momentum variable and the process iterate.

No-U-Turn Hamiltonian Monte Carlo:

HMC requires fixing the step size ϵ and the number of Leapfrog steps L. A poor choice of either of these parameters will result in poor efficiency of the HMC. No-U-Turn Hamiltonian Monte Carlo(NUTS) automatically fixes the value of L, which is an extension of HMC. A small value of L dictates that the particle(selected point of the parameter space) moving on a random walk. Again, for a larger value of L the particle will oscillate and waste valuable computational time. NUTS runs the Hamiltonian evolution equation for a particular case in both forward and backward directions of *time* until the condition of U turn condition is satisfied. NUTS proceeds by creating two particles $(\mathbf{q}_n^+, \mathbf{p}_n^+)$ and $(\mathbf{q}_n^-, \mathbf{p}_n^-)$, representing the progress in the forward and backward direction of *time*. This means creating a *binary tree* at each step of the iteration [125]. The U turn condition is given by

$$(\mathbf{q}_n^+ - \mathbf{q}_n^-).\mathbf{p}_n^- < 0$$
$$(\mathbf{q}_n^+ - \mathbf{q}_n^-).\mathbf{p}_n^+ < 0$$

In NUTS, we move in both directions of the closed elliptical path of Hamiltonian phase space, and when the vector alignment of the momentum variables $\mathbf{p}_n^+$

and $\mathbf{p}_n^-$ flips it indicates that we have moved half way of the trajectory, and then we stop.

There are also non-parametric and model independent techniques which can be used in reconstruction of observational quantities and also in parameter estimation. Here, we attempt to implement one of the non-parametric and model independent technique called Principal Component Analysis(PCA). In the next section we discuss different variants of the methodology and then we introduce the PCA road map in general.

1.8 Application of Principal Component Analysis in Cosmology

Principal Component Analysis(PCA) has the potential to predict the form of cosmological quantities in a model-independent, nonparametric manner [126–130]. In [131] and [132], different variants of PCA techniques are adopted. From the point of view of the application of PCA, there exist two distinct methodologies. These methods differ mainly in the way the covariance matrix is calculated, which is the first step of any PCA technique. One way to implement PCA is by computing the Fisher matrix, [126–130, 133–139]. One can bin the redshift range and assume a constant value for the quantity to be reconstructed in that redshift bin. These constant values are the initial parameters of the PCA. The Fisher matrix quantifies the correlation and uncertainties of these parameters. Therefore, by deriving these constants from different bins using PCA, we can reproduce our target quantity in terms of redshift [130]. Alternatively, a polynomial expression for the dynamical quantity can be assumed. In this case, the coefficients of the polynomial are the initial parameters for PCA, and the analysis gives the final values of these coefficients, which eventually gives the dynamical quantity [127].

Principal Component Analysis is independent of any prior biases and is also helpful in comparing the quality of different datasets [134, 140]. It is an application of linear algebra, which makes the linearly correlated data points uncorrelated. The correlated data points of the dataset used in PCA are transformed by rotating the axes, where the angle of rotation of these axes is such that linear correlations between data points are the smallest compared to any other orientation. The new axes are the Principal Component(PC)s of the data points, and these PCs are orthogonal to each other. In terms of information in the dataset, PCA creates

a hierarchy of priority between these PCs. The first PC contains information of the signal the most, and hence has the smallest dispersion of data points about it. The second PC contains less information than the first PC and therefore provides a higher dispersion of the data points as compared to the first PC. Higher-order PCs have the least priority as these correspond to noise and we can drop them. The reduction of dimensions is a distinctive feature of PCA. Therefore, the final reconstructed curve in the lower dimension corresponds predominantly to the signal of the dataset. The PCA method also differs from the regression algorithms, which cannot distinguish between signal and noise. PCA can omit the noise-related features and pick the actual trend of the data points [73, 141, 142]. In the following section, we discuss the general formalism of PCA.

1.9 Introductory idea and the algorithm of Principal Component Analysis

An interesting method to reconstruct the evolution of cosmological quantities is the application of non-parametric techniques. Various statistical techniques have been adopted for non-parametric reconstruction of cosmological quantities [143–148]. Along with PCA, another promising techniques in non-parametric approaches is the Gaussian process (GP) [149–155], where we can create a multivariate Gaussian function with a determined mean and corresponding covariance function from any finite number of collections of random variables.

Principal Component Analysis(PCA) is an application of linear algebra that has a wide spectrum of applications from neuroscience to computer graphics, including almost all the basic science branches. PCA provides the roadmap to reduced a complex data-structure to a minimum dimension, also it omits the noise part of the dataset and reveals new and sometimes hidden structure of the dataset.

1.9.1 The road-map of Principal Component Analysis

The goal is to find out the basis, which can express the dataset in a more meaningful manner. In the process of expressing the dataset in new basis we differentiate between signal and noise parts of the dataset.

Initial basis:

We start by expressing the dataset in a basis vector. This choice of initial basis vector is done on a case-by-case basis. After the selection of the initial basis, each sample we create is one of the vector points of our dataset.

In linear algebra, the set of orthogonal basis vectors of dimension $1 \times m$ is written as,

$$\mathbf{B} = \begin{bmatrix} \mathbf{b_1} \\ \mathbf{b_2} \\ \vdots \\ \mathbf{b_m} \end{bmatrix} = \begin{bmatrix} 1 & 0 & \dots 0 \\ 0 & 1 & \dots 0 \\ \vdots & \vdots & \ddots \vdots \\ 0 & 0 & \dots 1 \end{bmatrix} = \mathbf{I} \tag{1.67}$$

In eqn(1.67) $\mathbf{b}$ is a orthogonal basis vector of dimension $1 \times m$. Each component b_i has m number of terms. Eqn(1.67) can be expressed in a concise way as $\{\mathbf{b_i}\}$. As a first step, we express the whole dataset in terms of $\{\mathbf{b_i}\}$.

Change of basis:

As the second step, we rearrange the basis vectors, which means the reorientation of the axis of the dataset. In most of the cases, we first place the origin of the basis vector in the mean of the dataset. The final basis vector should represent the dataset in a more expressive manner, which means expressing the significant features of the dataset. In matrix form, we can express the dataset in $\mathbf{U}$, in which each column represents one sample of the dataset. If the total number of basis is m, as shown in eqn(1.67) and n is the number of samples collected, then the dimension of $\mathbf{U}$ will be $m \times n$.

If $\mathbf{V}$ is the final dataset which is related to the initial dataset by linear transformation then

$$\mathbf{PU} = \mathbf{V} \tag{1.68}$$

Eqn(1.68) is the equation of rotation, which transform $\mathbf{U}$ to the basis vector $\mathbf{V}$. If $\mathbf{p}_i$ are the rows of $\mathbf{P}$, and $\mathbf{u}_i$ and $\mathbf{v}_i$ are the columns of $\mathbf{U}$ and $\mathbf{V}$ respectively, we will get

$$\mathbf{v}_i = \begin{bmatrix} \mathbf{p}_1 \cdot \mathbf{u}_i \\ \mathbf{p}_2 \cdot \mathbf{u}_i \\ \vdots \\ \mathbf{p}_m \cdot \mathbf{u}_i \end{bmatrix} \tag{1.69}$$

We can say from eqn(1.69) that each element of $\mathbf{V}$ is a projection of p_i to $\mathbf{u}_i$. Therefore, $\mathbf{v}_i$ is a projection on to the basis of $\{\mathbf{p}_1, \mathbf{p}_2, \ldots, \mathbf{p}_m\}$. We can say, $\mathbf{P}$ are the new form of basis which transforms the data matrix $\mathbf{X}$ to the newdata matrix $\mathbf{Y}$.

Covariance Matrix:

Reduction of redundant part of the dataset is the objective of PCA. If two measurements are given as,

$$\mathbf{A} = \{a_1, a_2, \ldots, a_n\} \qquad \mathbf{B} = \{b_1, b_2, \ldots, b_n\}$$

n is the total number of sample collected. We can write the variance and covariance as

$$\begin{aligned} \sigma_A^2 &= \frac{1}{n} \sum_i a_i^2 \\ \sigma_B^2 &= \frac{1}{n} \sum_i b_i^2 \\ \sigma_{AB}^2 &= \frac{1}{n} \sum_i a_i b_i \end{aligned}$$

The absolute magnitude of the covariance matrix is a measure of degree of redundancy. The covariance matrix quantifies the linear relationship of the two variables $\mathbf{A}$ and $\mathbf{B}$. A large positive value of covariance indicates a positively correlated value, and similarly a negative covariance value indicates anticorrelation. For a large numbers of variables, the dimension of covariance matrix increases accordingly. Therefore, for two uncorrelated variables A and B we have $\sigma_{AB} = 0$, and if $\sigma_{AB} = \sigma_A$ then $A = B$.

Now if we generalize the PCA data-matrix $\mathbf{X}$ from two one-dimensional data-variables $\mathbf{A}$ and $\mathbf{B}$ to an arbitrary m number of variables then this $m \times n$ matrix

$\mathbf{X}$ is given as

$$\mathbf{X} = \begin{bmatrix} \mathbf{x}_1 \\ \mathbf{x}_2 \\ \cdots \\ \mathbf{x}_m \end{bmatrix} \tag{1.70}$$

In eqn(1.70) each row of the data-matrix $\mathbf{X}$ represents all the measurements correspond to a particular basis vector, while each column of the data-matrix corresponds to the value of all the variables to a particular trial. The general definition of the covariance matrix can be given as

$$\mathbf{C_X} = \frac{1}{n}\mathbf{X}\mathbf{X}^T \tag{1.71}$$

The matrix $\mathbf{C_X}$ is a symmetric matrix, with dimension $m \times m$. The diagonal entries of $\mathbf{C_X}$ are the variance of the corresponding basis variable and the off-diagonal entries are the covariance. The covariance value gives the idea about the redundancy and noise of the dataset. The covariance matrix contains all the covariance pairs of the PCA dataset; the covariance matrix is at the heart of the PCA methodology.

Let us assume that final data matrix is given by $\mathbf{Y}$ and the corresponding covariance matrix is denoted as $\mathbf{C_Y}$. The desired form of $\mathbf{P}$ should be that for which the co-variance matrix $\mathbf{C_Y}$ has the following properties

- All off-diagonal entries of $\mathbf{C_Y}$ will be zero, so the linear correlation of the pca data-matrix is omitted.
- PCA creating a hierarchy of priority and each successive dimension or the basis vector in the data-matrix $\mathbf{Y}$ rank-ordered according to the variance.

In the matrix form, if $\mathbf{P}$ is the matrix which can diagonalize $\mathbf{C_X}$ then, we can write,

$$\mathbf{C_Y} = \mathbf{P}\mathbf{C_X}\mathbf{P}^T \tag{1.72}$$

There are many ways to diagonalize the matrix $\mathbf{C_Y}$. Here we describe the decomposition with the help of eigenvector matrix to diagonalize $\mathbf{C_Y}$. The resulting ordered set of the vector $\mathbf{p}$ is called principal components [156]. In the case of eigenvector decomposition, we first find the eigenvector ($\mathcal{E}$) of the covariance

matrix ($\mathbf{C_X}$) of initial basis. The orthonormality of the basis vector ensures the existence of the matrix $\mathcal{E}$. From eqn(1.72) we can write $\mathbf{P} \equiv \mathcal{E}^T$.

The salient assumptions of PCA: The following are the assumptions in the algorithm of PCA.

I) Linearity:
PCA only can break the linear correlation of the data-matrix. This assumption introduces the eigenvector matrix as the sole candidate for the rotational matrix $\mathbf{P}$.

II) Vibrant features attached to larger variance:
This assumption restrict PCA to the set of statistical techniques in which application and implementation is possible only for the low noise dataset, that is where Signal to Noise Ratio(SNR) is high.

III) Principal Components are orthogonal to each other:
This assumption implies the use of linear algebra to decompose the error-matrix or covariance matrix and differentiate in between signal and noise.

In the following chapter, we discuss a special variant of PCA methodology that we develop and its implementation in different cosmological datasets. We focus mainly on dark energy equation of state parameter reconstruction. The method is however a general method which can be applied to different datasets to determine different parameters.

Chapter 2

Reconstruction using Principal Component Analysis

This chapter is based on "Reconstruction of late time cosmology using the Principal Component Analysis; Ranbir Sharma, Ankan Mukherjee, H K Jassal; Eur. Phys. J. Plus (2022) 137:219; [arXiv:2004.01393]

In this chapter we discuss the reconstruction of Hubble parameter $H(z)$, distance modulus $\mu(z)$ from Principal Component Analysis (PCA). We introduce two approaches in the reconstruction of the late time cosmological quantities and incorporate the correlation test calculation(CCC) to fix the number of parameter of final reconstruction of PCA. We show that the combination of PCA with CCC reduces the biases in the PCA methodology. The only input in the (PCA + CCC) technique is a tabulated dataset of the dependent variable or the observable. We will get the functional form of the observable in terms of independent variable as an output.

2.1 Methodology of reconstruction through Principal Component Analysis

We begin with an initial basis, $g_i = f(x)^{i-1}$, where $i = 1, 2, ..., N$ through which we can express the quantity to be reconstructed as,

$$\xi(x) = \sum_{i=1}^{N} b_i f(x)^{(i-1)} \tag{2.1}$$

The initial basis can be written in matrix form as, $\mathbf{G} = (f_1(x), f_2(x), ..., f_N(x))$. Coefficients b_i create a *coefficient space* of dimension N. Each point in the coefficient space gives a realization of $\xi(x)$, including a constant $\xi(x)$. PCA modifies the coefficient space and chooses a single realization. One can consider different kinds of functions as well as different combinations of polynomials as initial bases. Choosing one initial basis function over the other is done by correlation coefficient calculation described below.

The Pearson correlation coefficient for two parameters A and B is given by,

$$\rho = \frac{Cov(A, B)}{\sigma_A \sigma_B} \tag{2.2}$$

where $\rho \in [-1, 1]$. For linearly uncorrelated variables, the correlation coefficient, $\rho = 0$. An exact correlation is identified by $\rho = -1$ or $\rho = +1$. The Spearman rank coefficient is, in turn, the Pearson correlation coefficient of the ranks of the parameters; rank being the value assigned to a set of objects and it determines the relation of every object in the set with the rest of them. We mark the highest numeric value of a variable A as ranked 1, the second-highest numeric value of the variable as ranked 2 and so on. A similar ranking is done for the ranks of the parameter B.

To obtain the coefficients for the correlation analysis, we divide the parameter space into n patches. We therefore have n values associated with one coefficient of the polynomial; this is the number of columns of the coefficients matrix $\mathbf{Y}$, (eqn(2.6)). After ranking all the values of A and B, we obtain the table for the ranks of A and B. We then proceed to compute the Spearman correlation coefficient(r), which is the Pearson Correlation coefficient of rank of A and B. Like in the case of the Pearson Correlation coefficients, $r \in [-1, 1]$. Computing Kendall correlation coefficient(τ) gives a prescription to calculate the total number of concordant and dis-concordant pairs from the values of the variables A and B [157].

If we pick two pairs of points from the table of A and B, say (a_i, b_i) and (a_j, b_j), for $i \neq j$ if $a_i > a_j$ when $b_i > b_j$ or if $a_i < a_j$ when $b_i < b_j$; then that pair of points are said to be in concordance with each other. On the other hand, for $i \neq j$, $a_i > a_j$ when $b_i < b_j$ or if $a_i < a_j$ when $b_i > b_j$, then these two pairs are called to be in dis-concordance with each other. Every concordant pair is scored $+1$ and every dis-concordant pair is scored -1. The Kendall correlation coefficients are

defined as,

$$\tau = \frac{\text{actual score}}{\text{maximum possible score}} \tag{2.3}$$

$$\text{maximum possible score} = \frac{n(n-1)}{2}$$

Again, if N_{cp} is the number of concordance pair and N_{dp} is the number of disconcordance pair

$$\text{actual score} = N_{cp} - N_{dp}$$

Hence the expression of τ is,

$$\tau = \frac{N_{cp} - N_{dp}}{n(n-1)/2} \tag{2.4}$$

where, $\tau \in [-1, 1]$.

We perform the correlation coefficients calculation twice. The first time is to select the number of terms in the initial polynomial N(eqn(2.1)), and second time to select the number of terms in the final polynomial, (eqn(2.8)). We select that value of N for which the Pearson Correlation Coefficient is higher than the Spearman and Kendall Correlation coefficients. We use the R-package for statistical computing to calculate the correlation coefficients [158].

Values of linear and non-linear correlations depend on the quantity we want to reconstruct. They are also sensitive towards the data-set that we use in reconstruction. For instance, reconstruction of a fast varying function, which has non-zero higher order derivatives will introduce more non-linear contributions to the correlation of b_i than linear contributions, and we need a greater set of initial basis, which means a higher value of N. We take different values of N and check the linear and non-linear correlation coefficients to fix the value of N. Though a large value would help, we can not, however, fix N to any arbitrarily significant number as it makes the analysis computationally expensive.

To compute the covariance matrix, we define the coefficient matrix ($\mathbf{Y}$) by selecting different patches from the coefficient space, where n is the number of patches that we have taken into account and N is the total number of initial bases defined in eqn(2.1); therefore, $\mathbf{Y}$ is a matrix of dimension $N \times n$ and $b_n^{(N)}$ being the value of Nth coefficient in the nth patch.

In the present analysis, we have taken n to be the order of 10^3. We estimate the best-fit values of the coefficients at each patch by χ^2 minimization, where χ^2

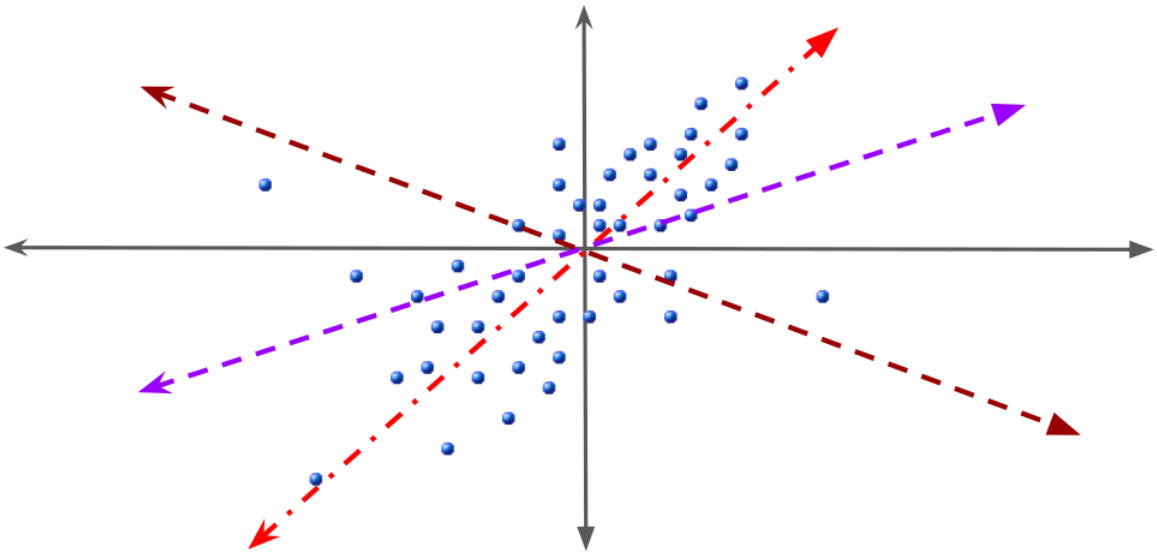

Figure 2.1: Figure gives the visual representation of the coefficient space created by the repetitive use of χ^2 in different patches, before the application of PCA. Different axis represents different coefficient axis. This is the representation of the data-matrix $\mathcal{Y}$. Here every axis is perpendicular to each other.

is defined as

$$\chi^2 = \sum_{j=1}^{k} \frac{(\xi(x)_{data} - \xi(\{b_i\}, x))^2}{\sigma_j^2} \tag{2.5}$$

k is the total number of points in the datasets. The coefficient space after the application of repetitive χ^2 can be visually represented as shown in fig(2.1). If the observational dataset have significant non-diagonal elements in the data covariance matrix(C_{data}), we have to incorporate C_{data} in eqn(2.5), as $\chi^2 = \Delta^T \mathcal{C}_{data}^{-1} \Delta$, where $\Delta = \xi(x)_{data} - \xi(\{b_i\}, x)$ and x, $\xi(x)_{data}$ vary for each data-points. Calculation of χ^2 in all the patches gives us the variation of the N coefficients and finally gives n number of points in the coefficient space, over which we apply PCA. We calculate the covariance matrix and correlations of the coefficients for these n points. In this analysis, each patch contains the origin of the multi-dimensional coefficient space.

The covariance matrix of the coefficients, $\mathbf{C}$ is written as,

$$\mathbf{C} = \frac{1}{n} \mathbf{Y}\mathbf{Y}^T \tag{2.6}$$

Eigenvector matrix, $\mathcal{E}$ of this covariance matrix will rotate the initial basis of the coefficient space to a position where the patch-points will be uncorrelated. We organize the eigenvectors in the eigenvector matrix $\mathcal{E}$ in the increasing order of eigenvalues. Eigenvalues of the Covariance matrix quantifies the error associated

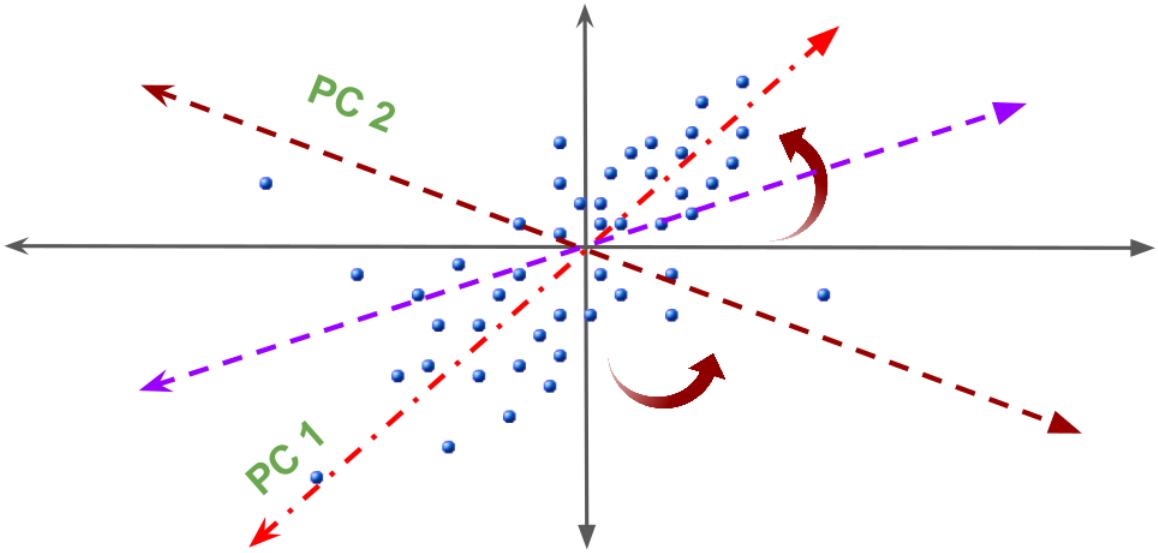

Figure 2.2: Figure gives the visual representation of rotation of the axis of coefficient space due to application of PCA. The red and brown axes are the final principal components for the data-set $\mathcal{Y}$. Here every axis is perpendicular to each other.

with each principal component [126, 130, 159, 160].

If $\mathbf{U} = (u_1(x), u_2(x), ..., u_N(x))$ the final basis is given by,

$$\mathbf{U} = \mathbf{G}\mathcal{E} \tag{2.7}$$

The final reconstructed form of $\xi(x)$ is,

$$\xi(x) = \sum_{i=1}^{M} \beta_i u_i(x) \tag{2.8}$$

where $M \leq N$ and the β_is are the uncorrelated coefficients associated with the final basis. The coefficients β_i are re-calculated by using χ^2 minimization, for the same n patches considered earlier to create initial coefficient matrix eqn(2.6). The value of M can be determined by correlation coefficient calculation discussed above. As PCA only breaks the linear correlation, we select M for which PCA is able to break Pearson correlation coefficient to the largest extent. As discussed in the sec(1.9) PCA is an application of linear algebra, and to break the linear correlation, PCA rotates the initial basis axes. The coefficient space view of the rotation and the final orientation of the axes can be visualized as shown in the fig(2.2). Eigenvalues of the covariance matrix $(e_1, e_2, e_3, ..., e_M)$ indicate how well PCA can pick the best patch point in the coefficient space. We look for the lowest number of final basis which can break the linear correlation to the greatest extent. We can start with smaller value of N which eventually influence the value of M,

but it will pose the risk of losing essential features from PCA data-set.

2.2 Reconstruction of dark energy equation of state

The Hubble parameter ($H(z)$) for a spatially flat Universe, composed of dark energy and non-relativistic matter is given by,

$$H^2(z) = H_0^2[\Omega_m(1+z)^3 + \Omega_x e^{3\int_0^z \frac{1+w(z')}{1+z'}dz'}] \tag{2.9}$$

Here we have assumed that the contributions to the energy density is only due to the non-relativistic dark matter and dark energy. The density parameters for non-relativistic matter and dark energy are given by Ω_m and Ω_x. The quantity H_0 denotes the present-day value of the Hubble parameter, namely the Hubble constant and $w(z)$ is the dark energy equation of state parameter ($w(z)$).

We assume no interaction between matter and dark energy in the present analysis. In the following subsections, we discuss the derived and direct approach to reconstruct $w(z)$ using PCA.

2.2.1 Derived Approach

The derived approach is a two-step process in the reconstruction of dark energy Equation of State(EoS). In the first step, we reconstruct the observable, namely the Hubble parameter using the $H(z)$ data and the distance modulus ($\mu(z)$) using the type Ia supernova data. Subsequently, we reconstruct $w(z)$ as a derived quantity from these two different physical quantities. Similar sequence of reconstructions have already been discussed in [126, 128, 130, 140]. Differentiating eqn(3.2) with redshift z as the argument and rearranging the terms we can express $w(z)$ as,

$$w(z) = \frac{3H^2 - 2(1+z)HH'}{3H_0^2(1+z)^3\Omega_M - 3H^2} \tag{2.10}$$

Here, H' is the derivative of Hubble parameter with respect to redshift z. Since $w(z)$ is related to $H(z)$ through eqn(2.10) by the zeroth and the first order differentiation of $H(z)$, the small difference in the actual and the reconstructed curve of $H(z)$ is amplified by the H' term. This process of amplification of the deviation

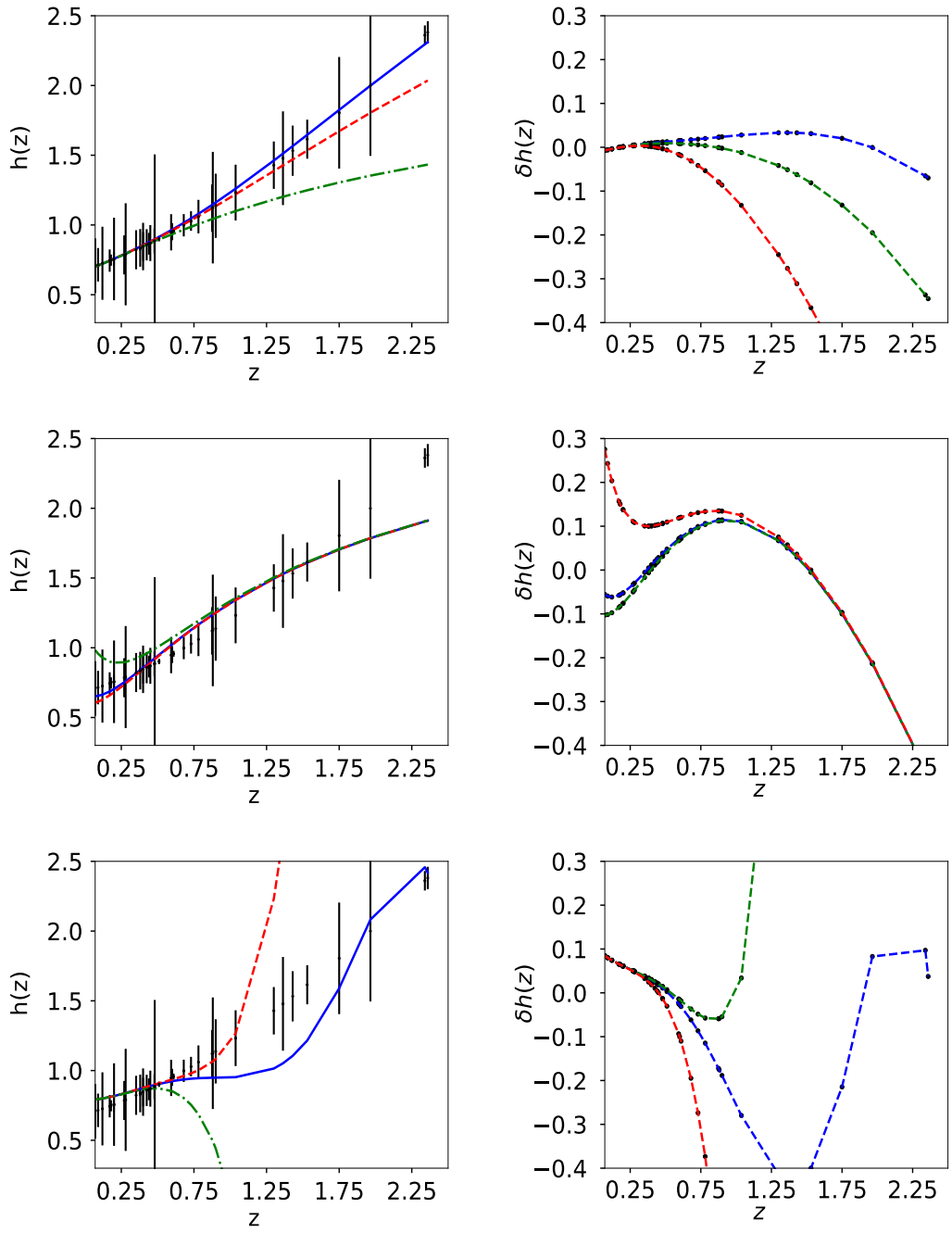

Figure 2.3: The plots in the figure show the reconstructed reduced Hubble parameter $h(z)$ for simulated data-set along with their residues. $\delta h(z)$ are the residues in the Hubble parameter. Residues are calculated as the difference between PCA reconstruction and the corresponding $h(z)$ calculated from the cosmological constant model. The left column is for the independent variable $(1-a)$, the middle column is for a and the right column is for z. For the blue curves, there is no reduction, that is, $M = N = 7$. The green and red curves are obtained by the reduction of the highest and second-highest Principal Components, respectively.

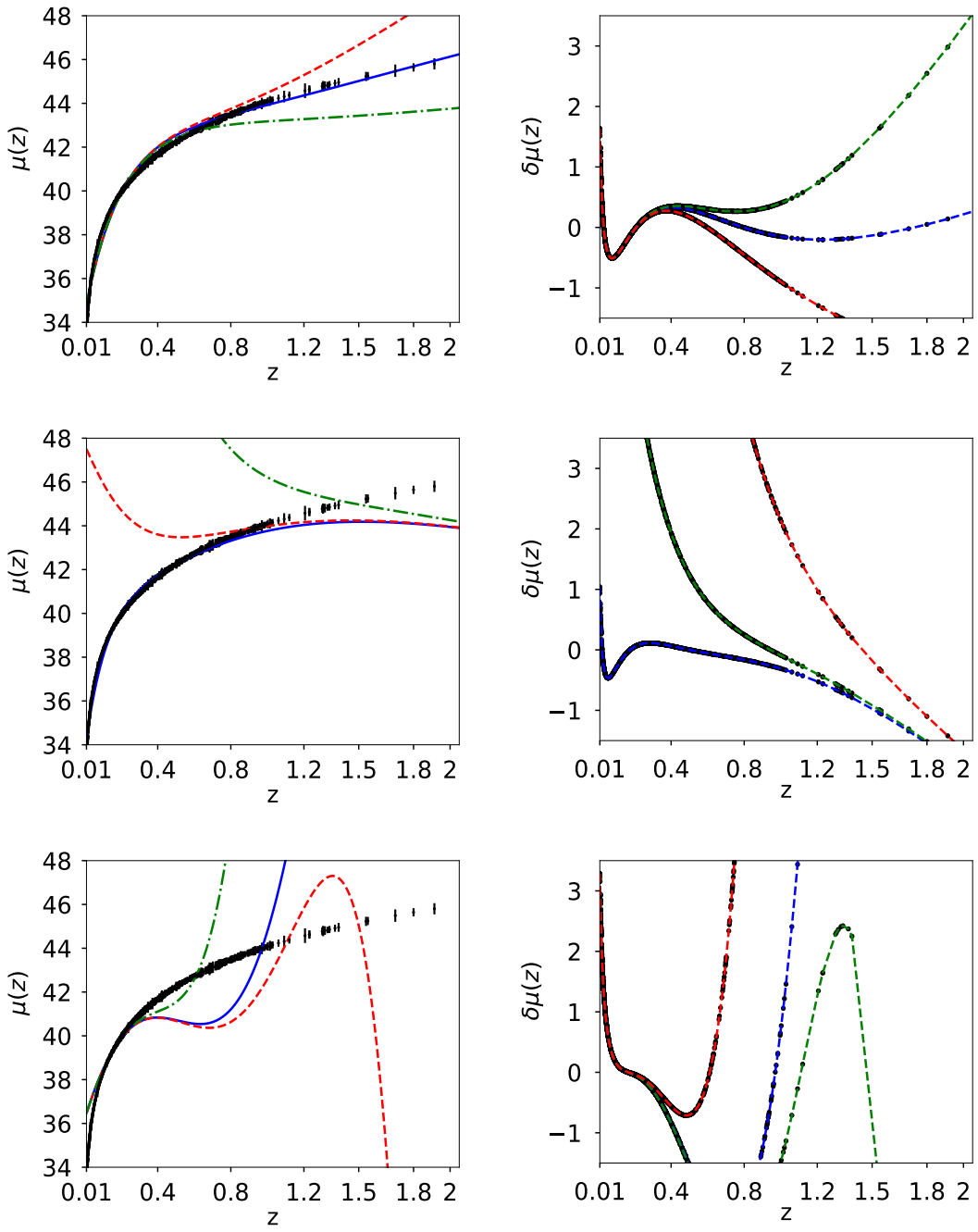

Figure 2.4: The plots in the figure show the reconstructed distance modulus $\mu(z)$ for simulated data-set along with their residues. $\delta\mu(z)$ are the residues in the distance modulus. Residues are calculated as the difference between PCA reconstruction and the corresponding $\mu(z)$ calculated from the cosmological constant model. The left column is for the independent variable $(1-a)$, the middle column is for a and the right column is for z. For the blue curves, there is no reduction, that is, $M = N = 7$. The green and red curves are obtained by the reduction of the highest and second-highest Principal Components, respectively.

from actual nature becomes more severe with subsequent higher-order differentiation of the reconstructed quantity.

The luminosity distance $d_L(z)$ is given by,

$$d_L(z) = \frac{c}{H_0}(1+z)\int_0^z d_H(z')dz' \tag{2.11}$$

where d_H, in terms of eqn(3.2) is,

$$d_H(z) = \left(\Omega_m(1+z)^3 + \Omega_x e^{3\int_0^z \frac{(1+w(z'))dz'}{(1+z')}}\right)^{-1/2} \tag{2.12}$$

and is related to the distance modulus as

$$\mu(z) = 5\log\left(\frac{d_L}{1Mpc}\right) + 25 \tag{2.13}$$

which is the dependent-variable in the type Ia supernovae data. From PCA, we determine the form of $\mu(z)$ directly from data and then from eqn(2.11) and eqn(2.12) find the expression of d_L. From eqn(2.13), we trace back to eqn(2.12) and find an expression which gives the $w(z)$ in terms of the distance modulus.

Since $D(z) = (H_0/c)(1+z)^{-1}d_L(z)$, the equation of state parameter is given by

$$w(z) = \frac{2(1+z)D'' + 3D'}{3D'^3\Omega_m(1+z)^3 - 3D'} \tag{2.14}$$

The second order derivative in eqn(2.14) makes the reconstruction of $w(z)$ through that of distance modulus unstable. For instance, if the reconstruction fails to pick some of the minute difference in the observational curve, then that difference will be amplified twice in the final calculation of the EoS. Therefore, the reconstruction of $\mu(z)$ should be more accurate in picking up approximately all the features of $w(z)$ which may be hidden within the supernovae data [115, 127, 161, 162].

In the reconstruction of $H(z)$ and $\mu(z)$, we begin with polynomial expansions in terms of the different variables z, a and $(1-a)$ where z is the red-shift and a is the scale factor. The analysis is carried out with seven terms in initial basis, which means creating a coefficient space of $N = 7$ dimensions (eqn(2.1)). We test our algorithm on a simulated data-set of ΛCDM cosmology. We generate the data-points of $H(z)$ and $\mu(z)$ for $w(z) = -1$ and the values of cosmological parameters Ω_m and H_0 are fixed at Planck 2018 values [163]. Fig(2.5) and table 2.2 show that our algorithm can predict the simulated data.

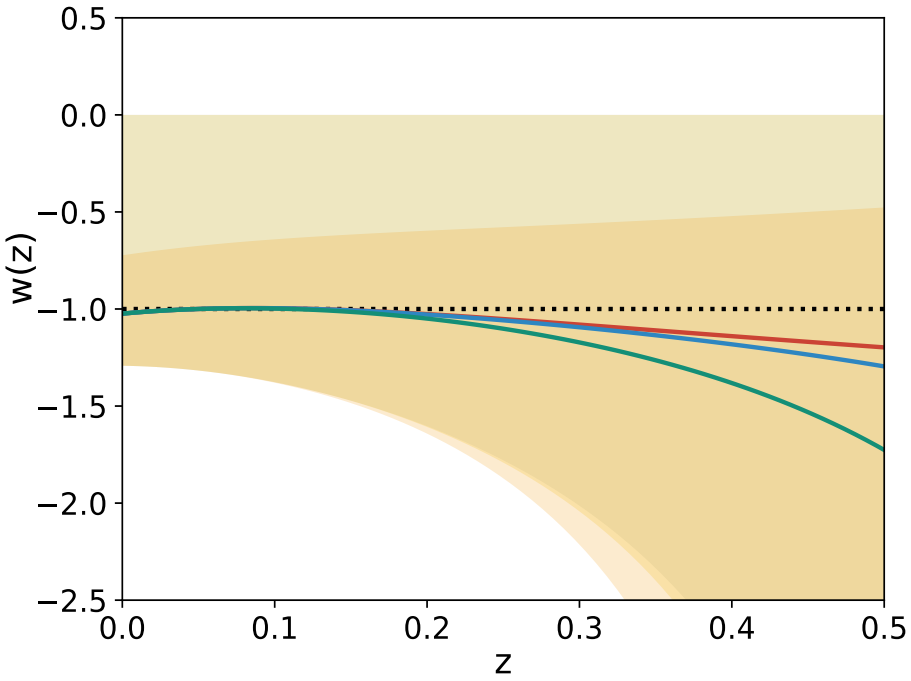

Figure 2.5: The plots in this figure show reconstruction of $w(z)$ for the simulated data. Red, blue and green curves are for the reconstruction with no reduction and with reduction of one and two terms respectively. In these curves, the value of Ω_m is fixed at 0.364, the value of Ω_m for which the reconstructed curve with no reduction and reduction of one term of the initial basis are the closest to the underlying $w(z) = -1$ for most of the low-redshift range. In the figure there are three patches; grey, yellow and brown, corresponding to all the reconstruction with Ω_m vary from 0.1 to 0.5 with no reduction of final terms and with reduction of one and two terms respectively. Here we fix the reduced Hubble constant at the value predicted by PCA for the simulated data-set, $h_0 = 0.674$. The black line is for comparison and it corresponds to $w(z) = -1$.

2.2.2 Direct Approach

For the direct reconstruction approach, we begin with a polynomial form of $w(z)$ itself. In eqn(3.2), the quantity $w(z)$ is in the exponent, and considering a polynomial form for $w(z)$ implies addition of some non-linear components to our linear analysis in coefficient space. Again we fix the dimension of the initial basis N by computing the correlation coefficients. Here we need to balance available computational power as well as the non-linearity we introduce, with the accuracy we demand to choose the value of N.

In this case too the independent variables are taken to be $(1-a)$, a and z. Here we introduce non-linear terms in the initial coefficients of PCA; here correlation

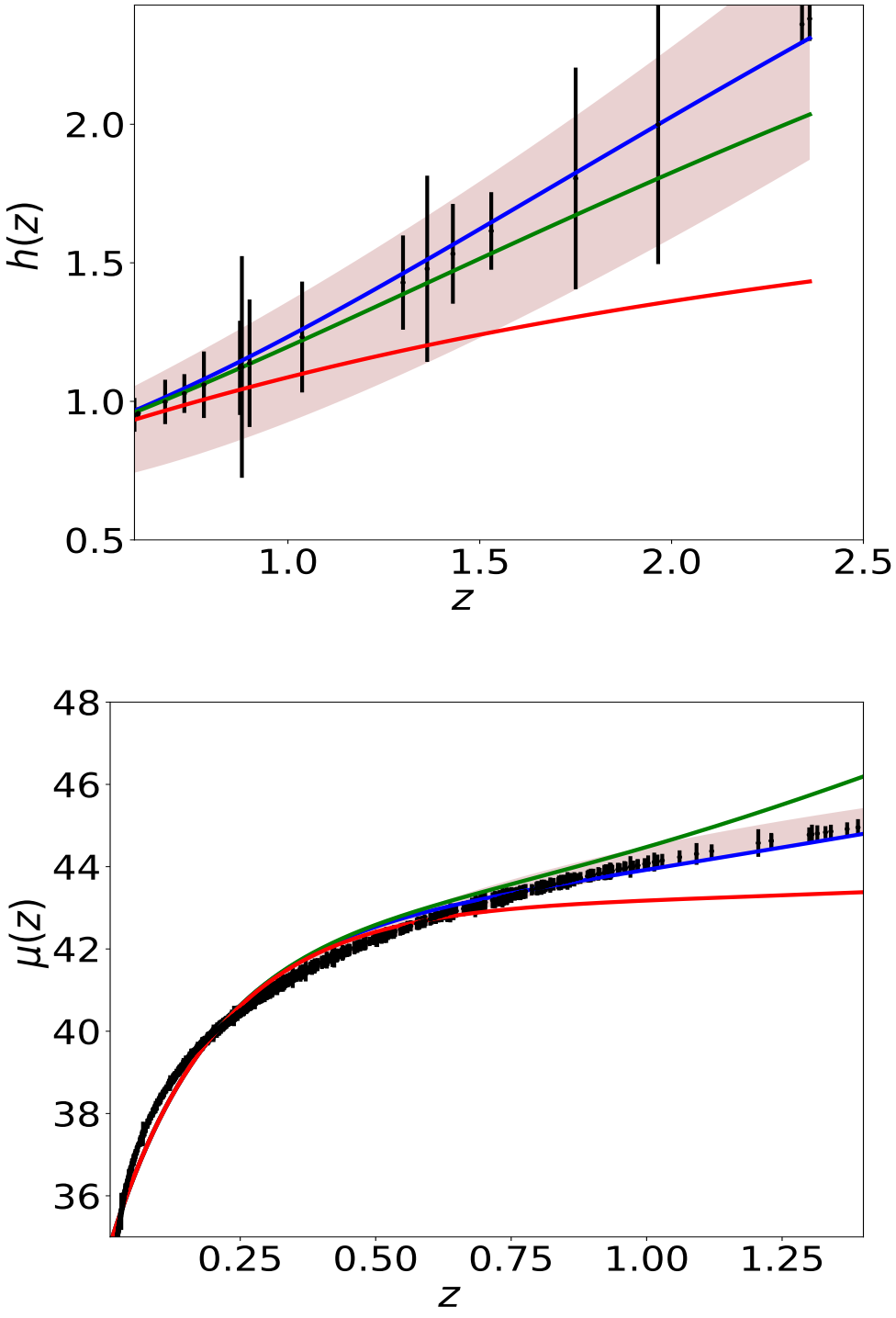

Figure 2.6: The plots show the reconstruction of $h(z)$ and $\mu(z)$ from the simulated Hubble parameter and supernovae data-set with allowed range wCDM cosmology with the initial basis function $(1-a)$. The brown patch is obtained for the variation of w and Ω_m in the range [-1.5 to -0.5] and [0.2 to 0.4] for wCDM cosmology. Solid blue, green and red line are for PCA reconstruction with no-reduction and with one and two terms respectively.

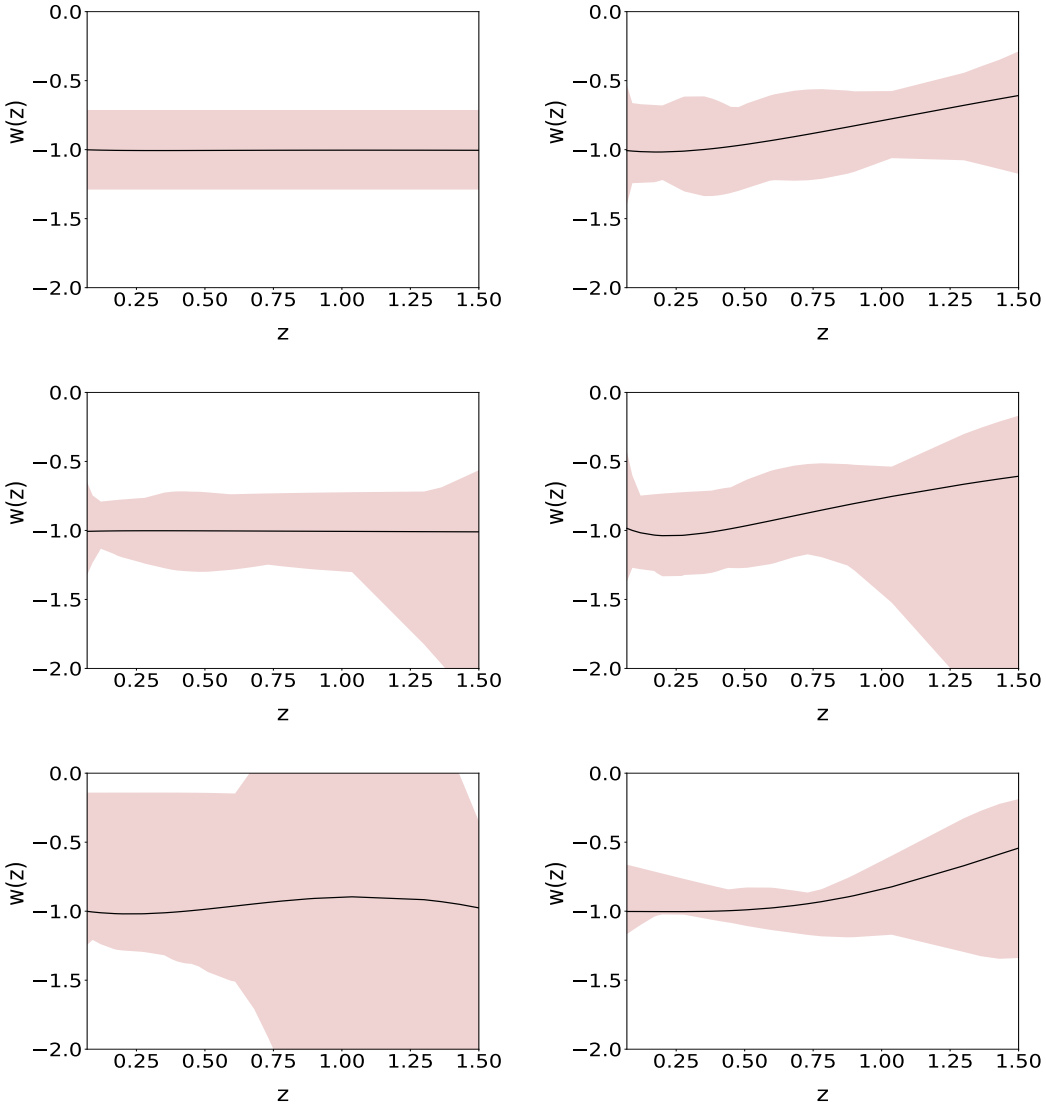

Figure 2.7: Plots of $w(z)$ in the direct approach with simulated data-sets. The left panels are for simulated data with $w(z) = -1$ and the right panels are for $w(z) = -\tanh(1/z)$. The first row is the reconstruction by variable $(1-a)$, second and the third row is the reconstruction by variable a and z, respectively. Black solid line corresponds to the minimum χ^2 and the red shaded region is the reconstruction using the PCA algorithm allowing a deviation of 0.3 from the minimum χ^2 curve.

coefficients calculation is not of assistance as in the case of derived approach 2.2.1 to select M. Due to the risk of compromising different features of the data-set and also due to the complex dynamics of correlation coefficients, we do not reduce any terms in the final basis ($N = M$) of the direct approach.

To test the effectiveness of both the approaches described above, we first work with simulated data-sets for specific models. We create simulated data-points for $w = -1$ (ΛCDM) and $w(z) = -\tanh(1/z)$ [131] where the values of Ω_m and H_0 are fixed at Planck 2018 values [163]. We use eqn(3.2) to calculate $H(z)$ at the same redshift value as in the real Hubble parameter vs redshift data-set [60–64]. Similarly, the distance modulus data points are simulated using equations (2.11),(2.12) and (2.13). Here we evaluate distance modulus $\mu(z)$ at the same redshift values as are there in type Ia supernovae (SNe) Pantheon data-set [80]. We later utilize the observational measurements of Hubble parameter at different redshift [60–64] and the distance modulus measurement of type Ia supernovae (SNe) data [80].

2.3 Reconstruction of late time cosmology by Principal Component Analysis

2.3.1 Correlation table

The correlation coefficients of the first three coefficients of the polynomial expression eqn(2.1) and eqn(2.8) of the reconstructed quantity is shown in table 3.1. PCA breaks the linear correlation of the coefficients, which is evident from table[3.1]. Presence of the non-linear correlation in the initial coefficients complicates the process. As the first three terms of the ultimate expression of the reconstructed quantity contains the dominant trend of the data-points, we only mention the correlation coefficients only for the first three parameters. The reconstruction which can break Pearson Correlation to a greater extent as well as have lesser Spearman and Kendall Correlation coefficients is selected. We can see from table 3.1 that the reconstruction by $(1 - a)$, breaks the correlation to a greater extent than in the case of a and z. Variation of correlation coefficients before and after the application of PCA is similar for both the simulated as well as the real data-set. Difference of Pearson correlation coefficients for simulated and real data-set in case of $(1 - a)$ and a is of the order of 10^{-6} or less. For the variable z,

the difference of Pearson correlation coefficients for real and simulated data is of the order of 10^{-4} or less.

2.3.2 Derived approach

We first reconstruct $H(z)$ and $\mu(z)$ using simulated dataset. The reconstruction with simulated data is a check on the viability of the method. Fig (2.3, 2.4) shows the reconstructed curves of the reduced Hubble parameter $h(z)$ and distance modulus $\mu(z)$ obtained for the simulated data. The reconstructed curves are for three different reconstruction variables $(1-a)$, the scale factor a and the redshift z. It is clear from the plot 2.4, 2.3 that the PCA reconstruction produces a consistent result when $(1-a)$ is chosen as the independent variable. We also plot the difference between the fiducial model and the reconstructed curves along for a comparison. The plots of the residues clearly show that the reconstruction of both $h(z)$ and $\mu(z)$ validates the reconstruction appraoch. The number of terms on the initial basis is fixed at $N = 7$. We also check our results for $N = 8$ and $N = 10$, and find that the results do not vary significantly. Here, we present the reconstruction curves from the variable z only for the simulated data-set. Since in this case, we do not achieve a viable reconstruction, we do not analyse this further for real data.

From table 2.2 we see that both $(1-a)$ and a variables are able to predict the value of h_0 closer to the assumed value of h_0 in simulated data. We calculate the error in the prediction of h_0 from the Covariance matrix of the PCA data-set, where we give a cut off χ^2 value, χ^2_{cutoff} to mask out some patch points which lead to under-fitting [126, 164, 165].

Further, the correlation coefficient calculation suggests that the best choice of number of terms for variable $(1-a)$ in the final polynomial(2.8) is $M = N - 1$, reduction of one term from the initial polynomial expression(2.1). For variable a and z, it is $M = N$, hence there is no reduction of terms.

Fig(2.5) shows that the variable $(1-a)$ reproduces $w = -1$ behaviour when the simulated data is used. Shaded region of fig(2.5) represents all possible $w(z)$ vs z curves produced by PCA for simulated data with a variation of Ω_m from 0.1 to 0.5. Ω_m is one of the free parameters in our methodology, and the methodology does not pick any one curve over another. The polynomial expression of $H(z)$ in $(1-a)$ is effectively an infinite series in terms of z. As the independent variable of the data-sets is z, therefore, $(1-a)$ and a can capture more features than the initial basis z.

Basis	State	Pearson	Spearman	Kendall
(1-a)	$[b_{12}, b_{13}, b_{23}]$	$[-0.99, 0.92, -0.96]$	$[-0.52, 0.55, -0.94]$	$[-0.45, 0.52, -0.85]$
	$[\beta_{12}, \beta_{13}, \beta_{23}]$	$[0.94, 0.219, 0.506]$	$[0.92, 0.69, 0.63]$	$[0.845, 0.69, 0.56]$
a	$[b_{12}, b_{13}, b_{23}]$	$[-0.98, 0.93, -0.98]$	$[-0.68, 0.60, -0.87]$	$[-0.62, 0.53, -0.75]$
	$[\beta_{12}, \beta_{13}, \beta_{23}]$	$[-0.99, 0.99, 1]$	$[-0.30, -0.32, -0.99]$	$[-0.21, -0.23, 0.97]$
z	$[b_{12}, b_{13}, b_{23}]$	$[-0.92, 0.64, -0.86]$	$[-0.31, 0.35, -0.72]$	$[-0.23, 0.35, -0.62]$
	$[\beta_{12}, \beta_{13}, \beta_{23}]$	$[1, -0.96, -0.96]$	$[0.999, -0.01, -0.01]$	$[0.998, 0.09, 0.08]$

Table 2.1: This table shows Pearson, Spearman and Kendall correlation coefficients between the coefficients of the first three terms of the series expansion of the reconstructed quantity for the reconstruction variables $(1-a)$, a and z respectively. This is in the derived approach for simulated Hubble parameter data. Here, b_{ij} is the correlation coefficients of the initial coefficients b_i and b_j, whereas β_{ij} are the correlation coefficients of the final coefficients β_i and β_j. The first, third and fifth rows (b_{12}, b_{13}, b_{23}), in the table, shows the correlation coefficients of the first three coefficients of the initial polynomial we start with, viz b_1,b_2 and b_3 with each other, eqn(2.1) for the basis variables $(1-a)$, a and z respectively. The correlation coefficients of the first three coefficients of the final polynomial, viz β_1, β_2 and β_3, eqn(2.8) given by the PCA algorithm is given in the second, fourth, sixth rows ($\beta_{12}, \beta_{13}, \beta_{23}$) for the basis variables $(1-a)$, a and z respectively. Since the correlation matrix is symmetric, here we only mention the upper diagonal terms. All the diagonal terms b_{ii} and β_{ii} are unity.

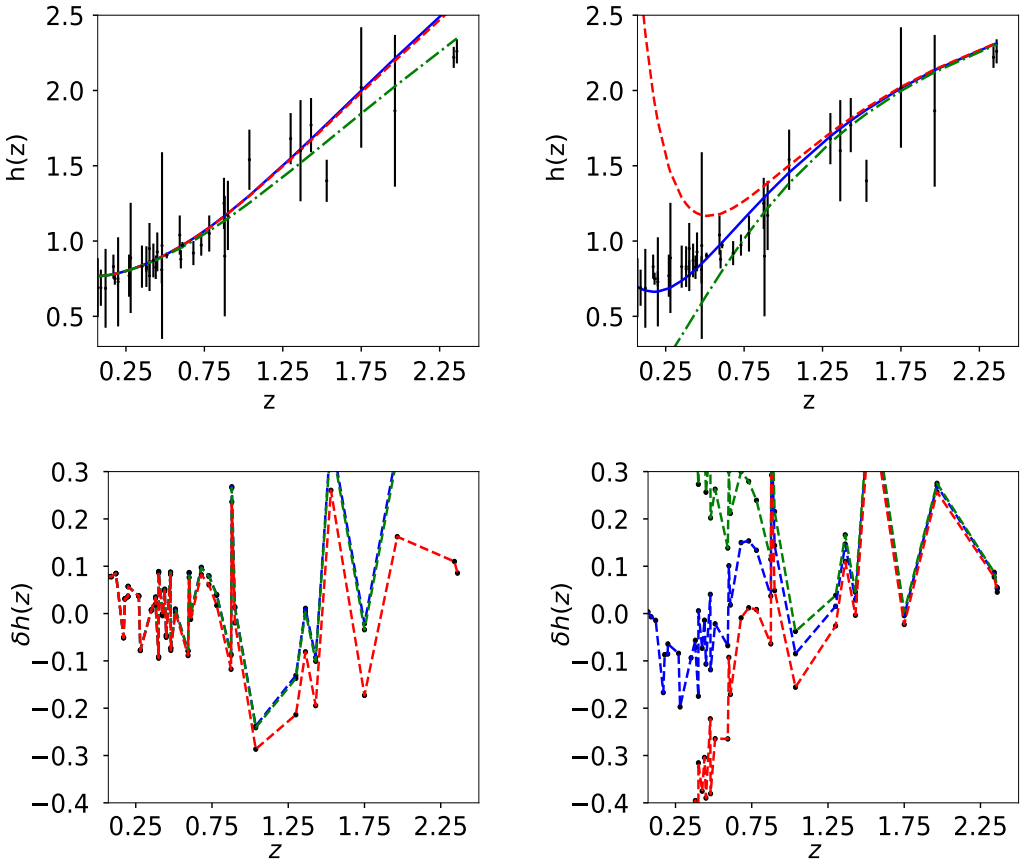

Figure 2.8: The plots in the figure show the reconstructed reduced Hubble parameter $h(z)$ for observed data-sets along with their residues. $\delta\mu(z)$ are the residue in the distance modulus respectively. Residues are calculated as the difference between PCA reconstruction and the corresponding $h(z)$ with the observational data. The left column is for the independent variable $(1-a)$, and the right column is for a. For the blue curves, there is no reduction, that is, $M = N = 7$. The green and red curves are obtained by the reduction of the highest and second-highest Principal Components, respectively.

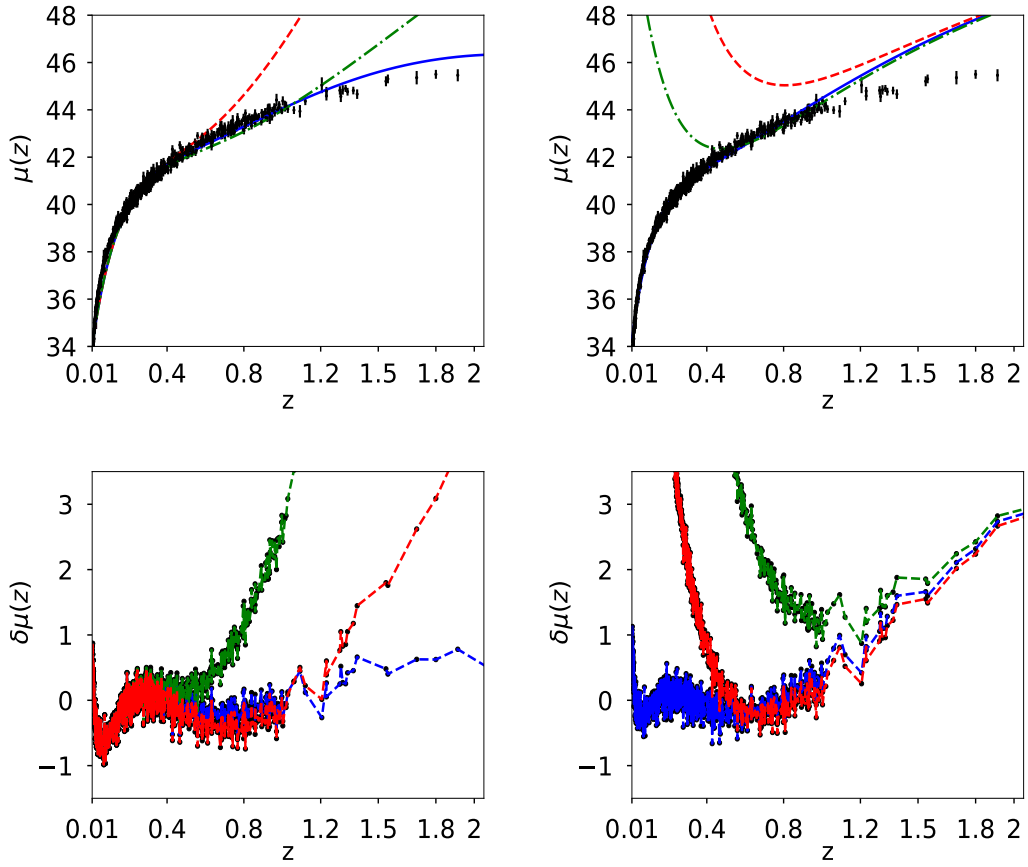

Figure 2.9: The plots in the figure show the reconstructed distance modulus $\mu(z)$ for observed data-sets along with their residues. $\delta\mu(z)$ represents the residue in the distance modulus. Residues are calculated as the difference between PCA reconstruction and the corresponding $\mu(z)$ from the observational data. The left column is for the independent variable $(1-a)$, and the right column is for a. For the blue curves, there is no reduction, that is, $M = N = 7$. The green and red curves are obtained by the reduction of the highest and second-highest Principal Components, respectively.

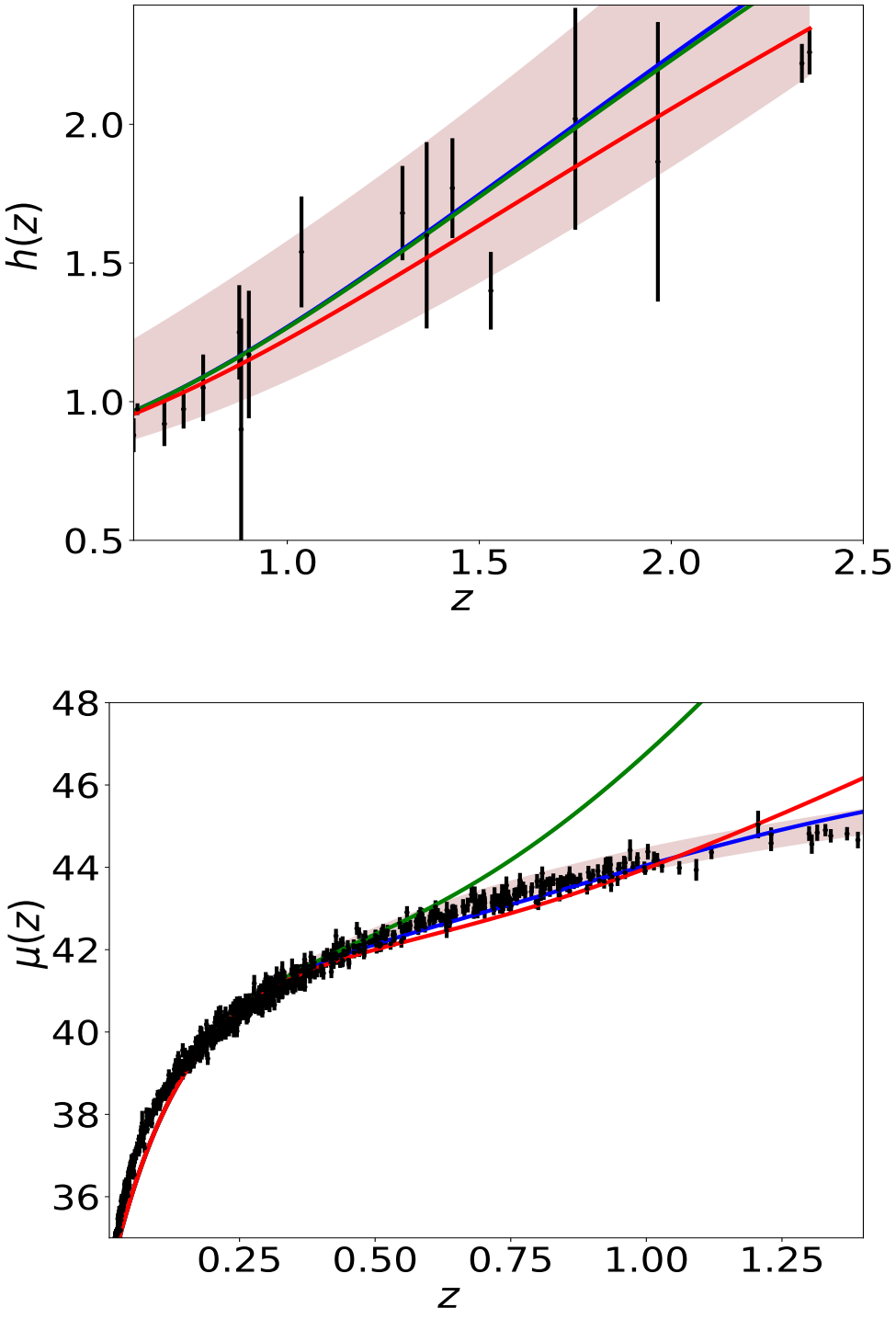

Figure 2.10: The plots show the reconstruction of $h(z)$ and $\mu(z)$ from the observed Hubble parameter and supernovae data-set with allowed range wCDM cosmology with the initial basis function $(1-a)$. The brown patch is obtained for the variation of w and Ω_m in the range [-1.5 to -0.5] and [0.2 to 0.4] for wCDM cosmology. Solid blue, green and red line are for PCA reconstruction with no-reduction and with one and two terms respectively.

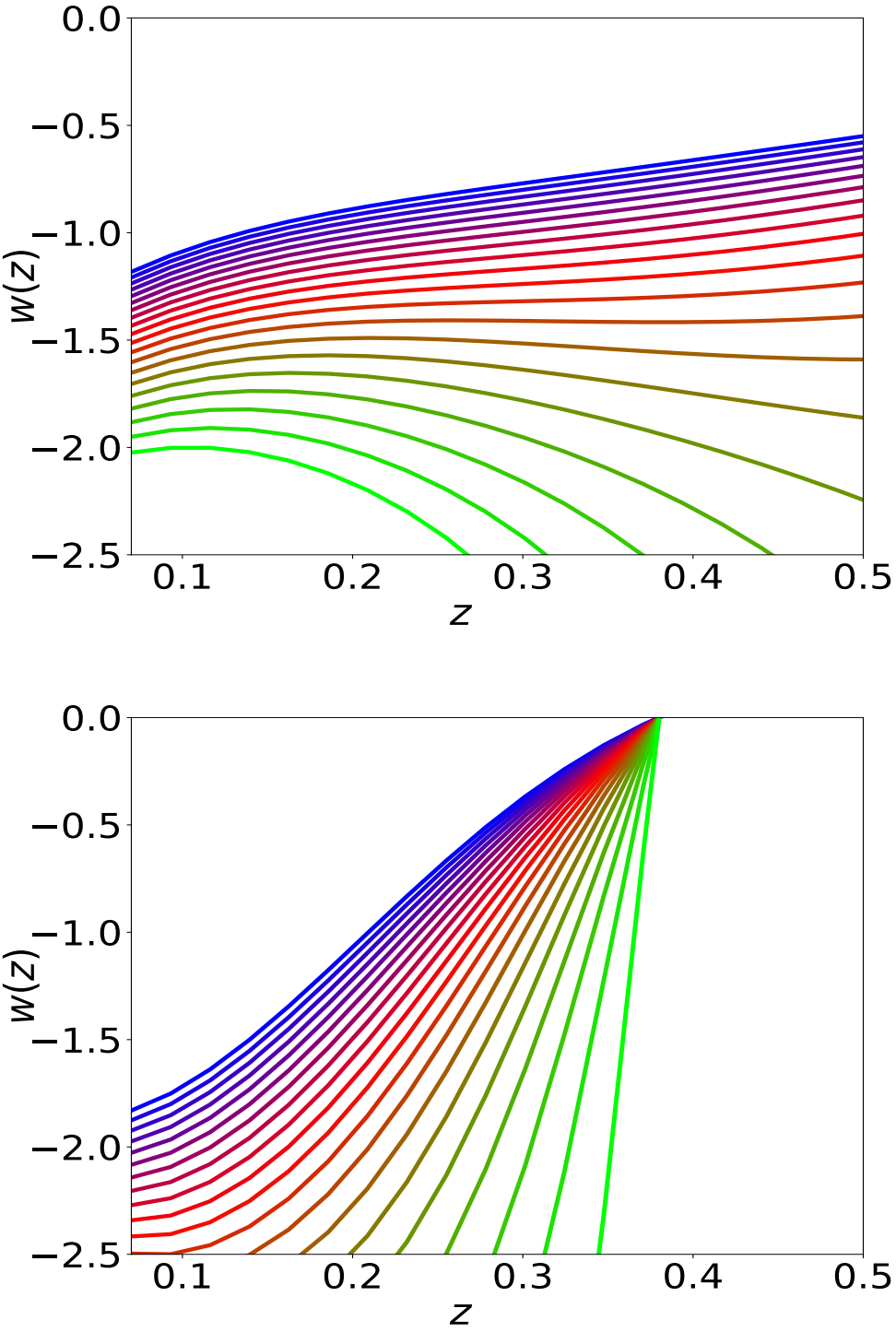

Figure 2.11: The figure shows the reconstructed $w(z)$ curves, obtained in the derived approach using real Hubble parameter data, with variables $(1-a)$ and a. Top figure is for $(1-a)$ and bottom one if for a. Each represents a reconstruction with a fixed value of Ω_m. Going from blue to the green color variation the value of Ω_m varies from 0.1 to 0.4, in a step of 0.015. We fix the reduced Hubble constant h_0 at a value obtained from the PCA algorithm, as mentioned in table 2.2.

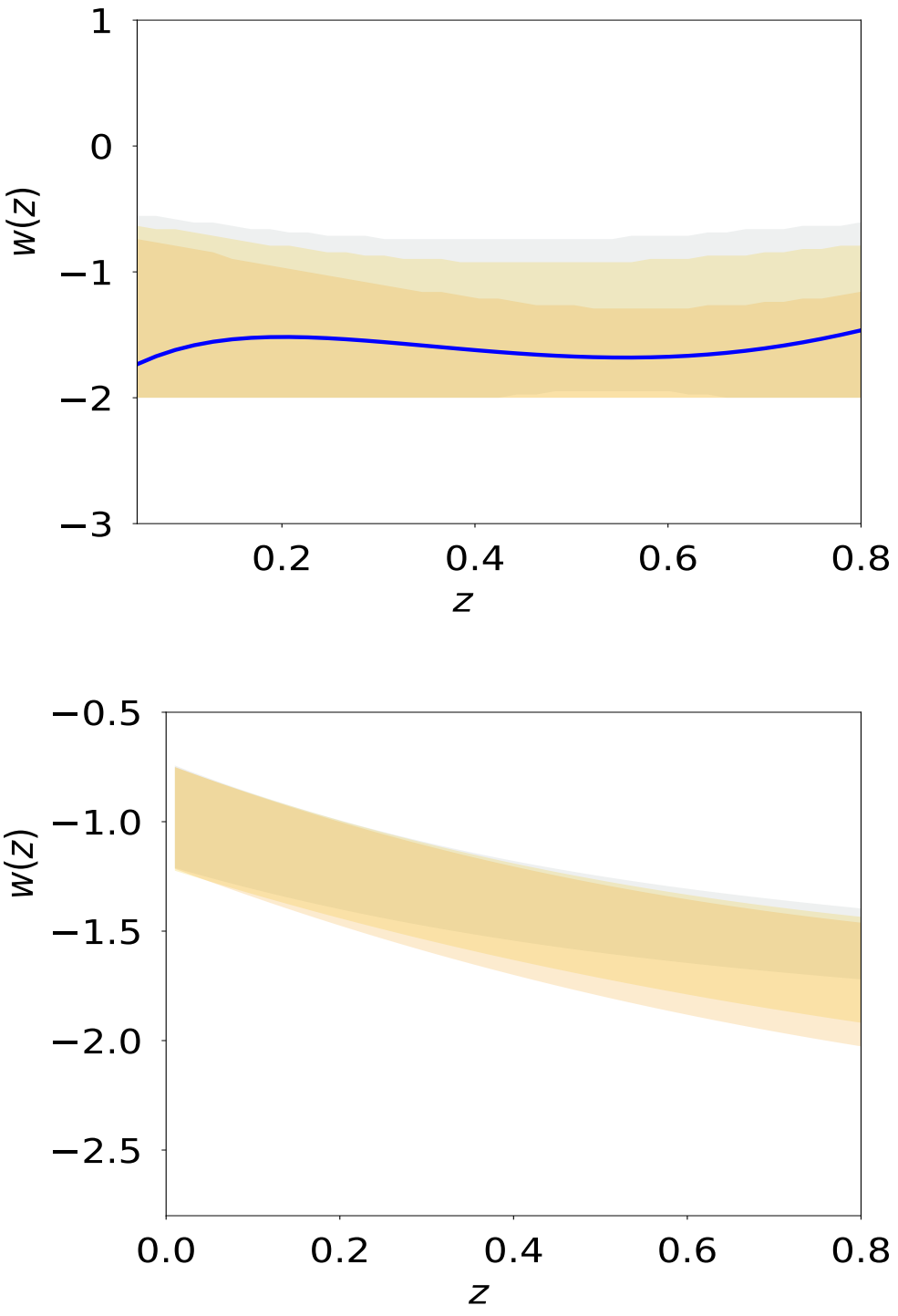

Figure 2.12: top and bottom plots are for real hubble parameter and supernovae data-set respectively. For both the plot Brown, yellow, grey bands are for $\Omega_m = 0.2, 0.3, 0.4$ respectively. In the top plot blue thick line is for the z vs $w(z)$ curve chosen by PCA. Both the plots are for $(1-a)$ and we vary w in the range $[-2, 0.6]$.

Reduced Hubble constant h_0		
Variable	Simulated	Observed
$(1-a)$	0.674 ± 0.118	0.784 ± 0.01157
a	0.664 ± 0.443	0.739 ± 0.103

Table 2.2: The value of reduced Hubble constant estimated for the simulated as well as real date-set using the derived approach. For generation of the simulated data, h_0 is fixed at 0.685. Error associated with the estimation of reduced Hubble constant are also given.

When the observational data-set is used in this polynomial expression, it indicates a time evolving $w(z)$, fig(2.11). The other two variables, namely a and z, could not successfully reproduce the $w = -1$ nature while using the simulated data. In the case of simulated supernovae data-set we see that all the $w(z)$ reconstructions for $h_0 = 0.685$ and Ω_m varying from 0.1 to 0.4 follows a similar trend after we choose a specific basis function. For all the three reconstruction variable $w(z)$ vs z curves fluctuate between phantom and non-phantom regime.

We now construct the equation of state parameter $w(z)$ from the reconstructed $H(z)$ and $\mu(z)$. It is clear from fig(2.5) that the reconstruction by derived approach for the variable $(1-a)$ successfully reproduces the $w(z)$ assumed earlier. On the other hand, the reconstruction variable a and z do not reproduce the $w(z)$ which has been assumed to simulate the data.

Using the reconstructed analytic form of $H(z)$ from derived approach, we estimate the present day value of the Hubble parameter H_0. The EoS parameter $w(z)$ calculated by the derived approach has the free parameter Ω_m, which we vary in the reconstructed $w(z)$ curves, fig(2.11). We present the estimated values of H_0, scaled by 100 $km\ sec^{-1}\ Mpc^{-1}$, for the analysis with simulated and the observational data in table 2.2. We also calculate the present day value of $w(z)$.

We calculate the range of $w(z)$ from eqn(3.2). We assume $w(z)$ to be constant (w) and find out the allowed range of w for the range of $h(z)$ determined by PCA. This range of $w(z)$ is dependent on Ω_m and we do the analysis for $\Omega_m =$

Variable	PCA	ΛCDM	wCDM	Planck(ΛCDM)
(1-a)	78.4001 ± 1.157	67.94 ± 5.15 (Plank+WP+ SDSS+SNLS)	68.07 ± 1.63 (Plank+WP+ WP+JLA)	67.9 ± 2.6 (EE+lowE)
a	73.9271 ± 10.3	69.85 ± 4.44 (Plank+WP +JLA)	68.19 ± 1.33 (WMAP9+JLA +BAO)	67.39 ± 0.54 (TT,TE,EE +lowE+lensing)

Table 2.3: This is the comparison table of the values of Hubble constant in standard units ($km\ s^{-1}\ Mpc^{-1}$), obtained in the present analysis (PCA) and obtained from other model-dependent estimations.

$0.2, 0.3, 0.4$, as shown in fig(2.12). The allowed range of w for $\Omega_m = 0.2, 0.3, 0.4$ are $[-2.73, -0.71]$, $[-3.33, -0.71]$ and $[-4.14, -0.91]$ respectively. We do the analysis for $(1 - a)$ as it is the selected variable by correlation test calculation. For supernovae data-set we find out the allowed range of $w(z)$, which lies within the error bar of the data-set by considering a polynomial with variable $(1-a)$. Range of $w(0)$ for $\Omega_m = 0.2, 0.3, 0.4$ are $[-1.2112, -0.7431]$, $[-1.224, -0.751]$ and $[-1.215, -0.7496]$ respectively.

Fig(2.6) indicates that the PCA reconstructions of $h(z)$ is well within the range of wCDM paramters for the simulated data. We vary Ω_m and equation of state parameter in $wCDM$ cosmology (w) in the range $[0.2,\ 0.4]$ and $[-1.5,\ -0.5]$ respectively. The ability of our methodology to reconstruct $h(z)$ and $\mu(z)$ reflects in the reconstruction of $w(z)$ for the simulated data.

To quantify the efficiency of our algorithm in picking up the underlying theory, we create an error function by the method of interpolation with the errors of observational data and use χ^2 with a data-set constructed from the final reconstruction curve of PCA. For this testing purpose we assume $w(z)$ and Ω_m as parameters, therefore constants for a particular data-set produced from PCA reconstruction. We find out that PCA reconstruction for both simulated and observed data-set, if we take ΛCDM as our model, the value $\Omega_m = 0.3$ and $w(z) = -1$ lies well within the 1σ range.

We now do the same analysis using observed data. Fig(2.8, 2.9) shows the reconstructed curves of reduced Hubble parameter $h(z)$ and $\mu(z)$ obtained for the real Hubble parameter and supernovae data-sets. It is evident from the plot

that PCA reconstruction with $(1-a)$ variable produces consistent results for observational data-set also. Fig(2.11) shows the final reconstruction of $w(z)$ from the observed Hubble parameter data-set with the reduced Hubble constant fixed at the value predicted by PCA. Reconstruction of the functional form of $h(z)$ by choosing a point from coefficient space (eqn(2.8)) is the first step of derived approach, which eventually gives us the value of h_0 from the same point. We do not vary the value of h_0 in the $w(z)$ reconstruction curves to ensure that both $h(z)$ and h_0 are from the same point of coefficient space. The values obtained from the observational data-set are higher as compared to the other model-dependent estimations. Table 2.3 presents the values of h_0, obtained, along with model-dependent estimations of h_0 from other studies [163, 166, 167] for a comparison.

2.3.3 Direct approach

For the direct approach, we have considered only the Hubble parameter data-set. Reconstruction is carried out for all the three independent variables $(1-a)$, a and z. As in the case of derived approach, we first use simulated data-set. The results obtained for the simulated data-sets are shown in fig(2.7). In this case, all three independent variables reproduce the nature of the equation of state parameter. In the direct approach, using the correlation test calculation, we find $N = 5$ to be the best choice for the number of terms in the initial polynomial eqn(2.1). As the number of terms on initial basis is comparatively low and we assume $M = N$ as our final basis number, the uncertainties which PCA poses in predicting the best patch-point is relatively low. The tiny non-linearity we introduced in the $H(z)$ by considering a polynomial form of $w(z)$ will be amplified in the case of supernovae data-set. Hence it makes the reconstruction much more unstable in the case of reconstruction of $w(z)$ through distance modulus calculation.

For the observed Hubble parameter data-set too we reproduce the curves using the same algorithm. In the case of direct approach, PCA cannot predict the value of H_0 and Ω_m; therefore, these two parameters have to be fixed prior to the analysis.

For real data-set, all the $w(z)$ plots for the variation of Ω_m from 0.2 to 0.4 after fixing reduced Hubble constant at $h_0 = 0.685$ have the similar trend. We also check the $w(z)$ plot for the variation of h_0 from 0.6 to 0.8 after fixing Ω_m at 0.30. Direct approach is more susceptible to model biasing as in the case of direct approach we have to select the value of Ω_m and h_0. Correlation coefficient

calculation also indicates that derived approach have more potential of breaking the correlations of the coefficients of the polynomial than the direct approach.

In the direct approach, though the reconstruction of the fiducial $w(z)$ is consistent (fig(2.7)), the correlation test calculation for the direct approach shows that the algorithm is not able to break the Pearson Correlation as it breaks down in the case of the derived approach. In the case of direct approach, for $(1-a)$ reconstruction, the magnitude of Pearson correlation coefficients decreases after applying PCA but changes signs for the first two principal components, whereas Kendall and Spearman correlation coefficient of $(1-a)$ for these two principal components assume higher negative value. Again, for reconstruction by the variable a, the Pearson Correlation decreases, though both Spearman and Kendall Correlation coefficients decrease in magnitude, it changes sign for the first two principal components. For the variable z, up to the first two principal components, Pearson correlation coefficients decrease, but Spearman and Kendall correlation coefficients assume large negative value. From the correlation coefficient calculation the derived approach is selected over the direct approach and selects the reconstruction by the independent variable $(1-a)$ as compared to variables a and z.

2.4 Summary

In this chapter, we reconstruct late-time cosmology using the Principal Component Analysis, which is a model independent and non-parametric approach. There are very few prior assumptions about nature and distribution of different components contributing to the energy of the Universe. Observational Hubble parameter and distance modulus measurements of type Ia supernovae are the observable quantities that are taken into account in the present analysis. We proceed in two different ways to do the reconstruction. The first one is a derived approach where the observable quantities are reconstructed from the data using PCA, and then $w(z)$ is obtained from the reconstructed quantities using Friedman equation. The other approach is a direct one. In this case, $w(z)$ is reconstructed directly from the observational data using PCA without any intermediate reconstruction. Based on the efficiency of the method to break the correlation among the coefficients we can select one reconstruction curve over the other. We achieve a better reconstruction in the derived approach as compared to the direct approach, even though the direct approach has lesser uncertainties than the derived approach in predicting the patch of the best coefficient point from the N dimensional coefficient space due to

the lower number of initial and final bases.

We have adopted the simulated as well as observed data-sets for our analysis. Simulated data-sets are used to check the efficiency. For the reconstruction of $w(z)$ the analysis produces consistent result only for the Hubble parameter data. Though the reconstruction of $\mu(z)$ through the derived approach is consistent and reconstruction of $\mu(z)$ is within the error bars of the data-set, the result for the reconstructed $w(z)$ deviates drastically from the physically acceptable range. The increase in the order of differentiation to connect $w(z)$ with $\mu(z)$ is a possible reason for this inconsistency. Here we are focusing on the $w(z)$ reconstruction only from $H(z) - z$ data-set. The reconstructed $w(z)$ by the variable $(1 - a)$, obtained in the derived approach for $H(z) - z$ data-set shows a phantom like nature, that is $w(z) < -1$ at present and a non-phantom nature in the past for most of the values of Ω_m and h_0. In the case of direct approach, $w(z)$ curves show oscillations in the phantom and non-phantom regime. The calculation of the correlation coefficients clearly shows a preference for the derived approach. PCA lacks the efficiency of breaking the correlation in the initial basis in case of the direct approach. This probably causes the inconsistency between the results obtained in the derived and direct approaches.

The other important factor is the variable of reconstruction. In the present analysis, we have adopted three different reconstruction variables, namely $(1 - a)$, a and z, in both direct and derived approaches. Values of correlation coefficients after PCA select the reconstruction variable $(1 - a)$ over the other two. We should emphasize the result obtained for variable $(1 - a)$ by derived approach. Since we have a finite number of terms in the initial polynomial, due to the constraints set by computational power, to some extent the results depends on the assumption of polynomial expression of the observables. One of our future plans is to develop an algorithm which can inclusively select the most suitable initial basis form for a fix computational power and a given observational data-set. The reconstructed curves, obtained for $(1 - a)$, show that $w(z)$ shows a phantom nature at present epoch and it was in non-phantom nature in the past. The model-independent reconstruction indicates an evolution of the dark energy equation of state parameter.

Chapter 3

Principal Component Analysis and Markov Chain Monte Carlo Method- A combined analysis

In this chapter, we show that a combination of Principal Component Analysis (PCA) and Markov Chain Monte Carlo (MCMC) is a competent method to determine cosmological parameters. We use the *No U Turn Sampler* (NUTS) to run the MCMC chains in the model parameter space. We test our methodology on simulated data and subsequently apply the same to the observed dataset. Assuming a polynomial expansion as the parametrization of the dark energy equation of state parameter of dark energy(EoS), we apply the algorithm to the real dataset and calculate the allowed range of EoS parameter.

3.1 Introduction

Likelihood analysis is the most commonly used technique in cosmological parameter estimation([168–173]). Increasing availability of observational datasets has tightened the constrains on the parameters of theoretical models [19–28]. These parametric methods are essential to understand the Universe and update our theoretical knowledge. Though it is crucial to determine the theory parameters, we have the observational data dependencies in the core of these methods, and new datasets reject or accept a model with a quantified precision.

As explained earlier in Chapters 1 and 2, using methods like the Principal

Component Analysis (PCA), we can determine the functional form of the observable of a dataset in a model independent manner [126–130, 133–137, 174–176]. If PCA brings the inherent functional form of the dataset then to constrain the parameters of a theoretical model we can use the data points derived from the functional form provided by the Principal Component Analysis.

3.2 Methodology and the results

In this section we first discuss the methodology of reconstruction of the functional form of the dependent variable in terms of the independent variable. We then explain the maximum likelihood method being used and the modification due to PCA.

3.2.1 Reconstruction of functional form of the dependent variable in terms of the independent variable

In our earlier work Chapter(2), we combined correlation coefficient calculation with PCA to quantitatively reconstruct the best fit cosmological model. We start by calculating the functional form of the reduced Hubble parameter $h(z)$ directly from the dataset, using Principal Component Analysis [174]. The steps of the PCA reconstruction mechanism are summarized again here :

1) The observable of the dataset is expressed as a polynomial over an initial basis function, which creates a coefficient space. The dimension of the coefficient space is same as the number of initial basis function.

2) We select different patches in the coefficient space and do a χ^2 calculation on each patch. For each patch, we get a minimum value of χ^2. These minimum χ^2 values for each patch give us the PCA data-matrix($\mathcal{D}$).

3) We calculate covariance matrix $\mathcal{C}$ of $\mathcal{D}$, from which the eigenvector matrix $\mathcal{E}$ is calculated. $\mathcal{E}$ is used to diagonalize $\mathcal{C}$ and omit the linear correlation of the data matrix. It also creates a new set of basis functions.

4) The observable are then expressed in terms of the final basis function.

5) With the help of these new basis functions, we create the new data-matrix $\mathcal{D}'$. To select the value of the final basis number M, we compare the correlation

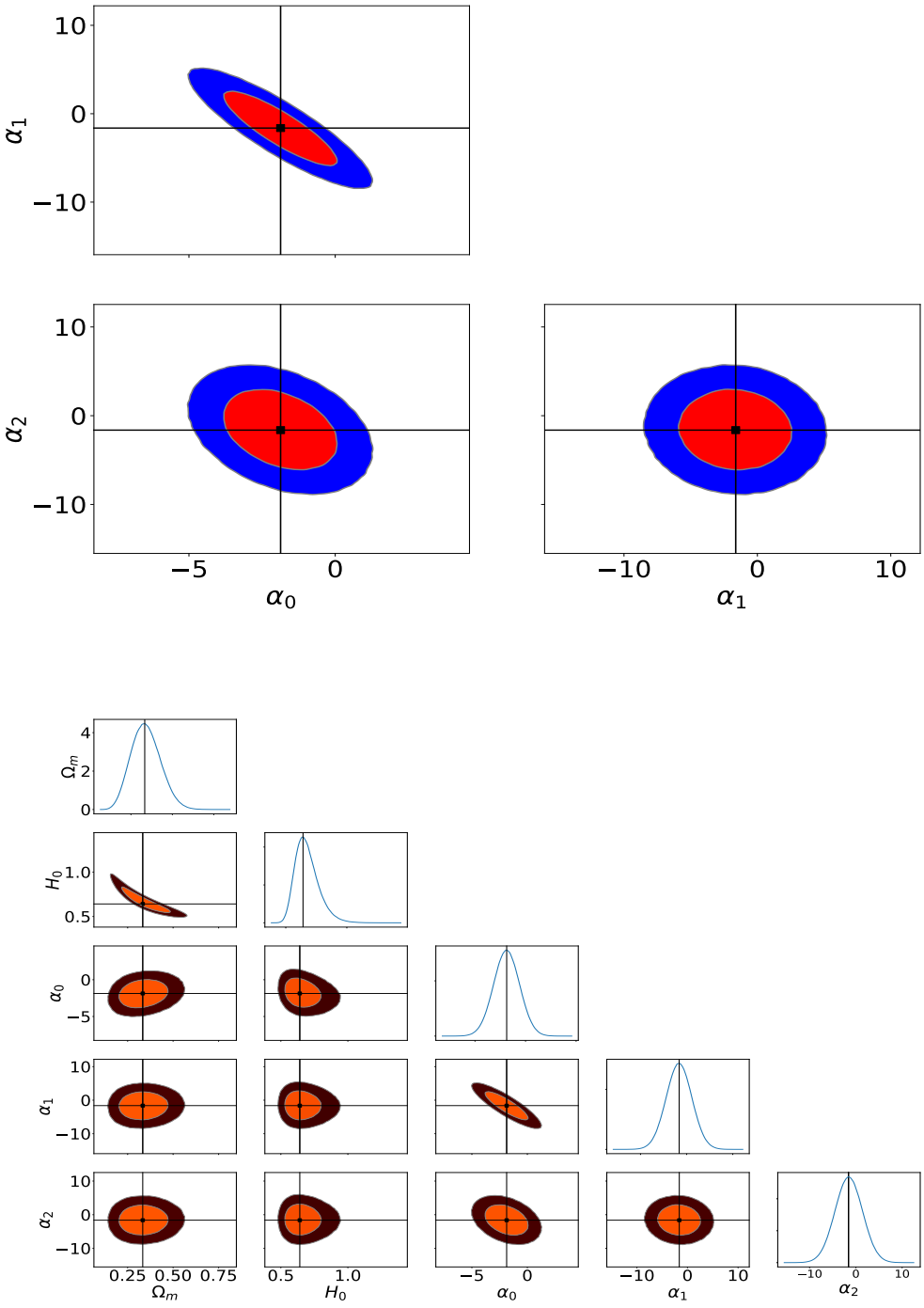

Figure 3.1: In this figure, the plot at the top shows the 1σ and 2σ contours for the three parameters $\vec{\alpha}$ in the equation of state parameter of dark energy, $w(z') = \sum_{i=0}^{2} \alpha_i \mathcal{F}(z')^i$ with $\mathcal{F}(z) = \frac{z}{(1+z)}$ in the case of simulated dataset. The figure at the bottom represents the 1σ, 2σ and 3σ contours for all the parameters present in the dataset for the simulated dataset.

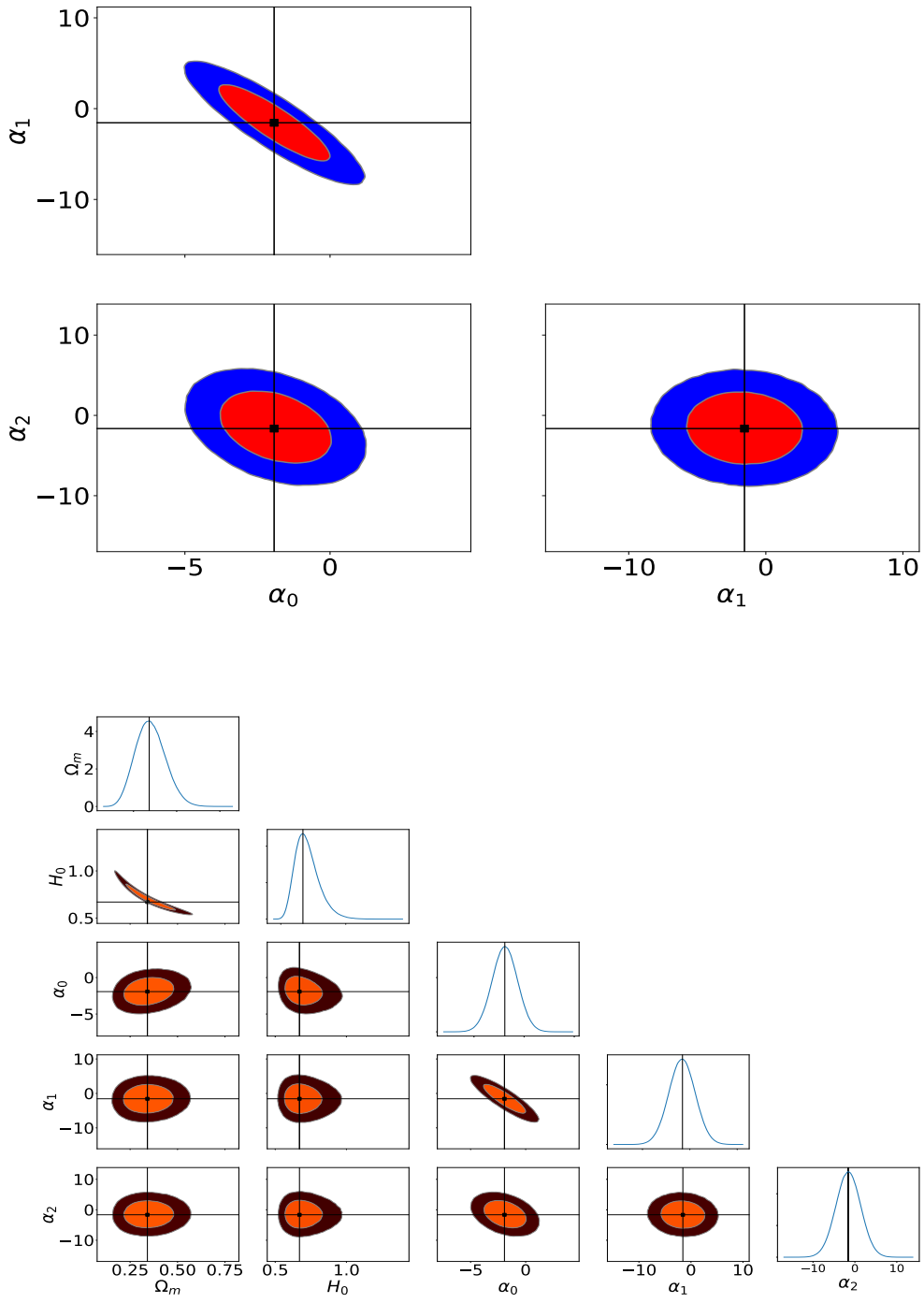

Figure 3.2: The plot on the top shows the 1σ and 2σ contours for the three parameters $\vec{\alpha}$ of $w(z') = \sum_{i=0}^{2} \alpha_i \mathcal{F}(z')^i$ with $\mathcal{F}(z) = \frac{z}{(1+z)}$ in the case of simulated dataset. The lower plot represents the 1σ, 2σ, 3σ contours for all the parameter presents in the dataset for the real, observed dataset.

matrix of $\mathcal{D}$ and $\mathcal{D}'$. Comparison of correlation matrix also helps us to choose the better initial basis variable.

If the initial basis function is given by $G = (f_1(z), f_2(z), ..., f_N(z))$ with $f_i(z) = f(z)^{(i-1)}$, the expression of reduced Hubble parameter is given by,

$$h(z) = \sum_{i=1}^{N} \beta_i f(z)^{(i-1)}$$

. The value of N is the number of terms in the polynomial expression of $h(z)$; it is also the dimension of coefficient space $\vec{\beta}$.

The value of N is determined by the correlation coefficient calculation [157, 174]. The value should be large enough such that the function can capture most of the features from the dataset. To select the value of N, we calculate Pearson, Spearman and Kendall correlation coefficients for the data-matrix $\mathcal{D}$ [157, 177]. As explained in the sec(2.1), the Pearson correlation coefficient gives the linear correlation exists in the dataset. Spearman and Kendall correlation coefficients give the non-linear correlations of the dataset at hand. For the Spearman correlation coefficient, we calculate the rank of the dataset. In our case, we arrange the ranks according to the numerical value, that is, we give rank 1 to the highest numerical value of the PCA dataset, and rank 2 to the second highest and so on. Spearson correlation coefficient is the Pearson correlation coefficient of the rank of the dataset. For Kendall correlation coefficient we find the concordant and disconcordant pairs. Kendall correlation gives the information about whether the dependent and independent variables are monotonically increasing or decreasing.

We choose the smallest value of N from the set of which the PCA data-matrix give us a higher value of Pearson Correlation coefficient compared to the Spearman and Kendall correlation coefficients. Only if the expression of the Hubble parameter $h(z)$ in terms of the polynomial is exact, there would no correlation in between the coefficients of the polynomial expression. Our motive is to break the correlation of the coefficient and make the polynomial expression of $h(z)$ as closer as possible to the actual $h(z)$. Again, PCA can only break the linear correlation; this is the reason we have to make sure that the value of non-linear correlation is negligible in comparison to the linear correlation, which is done by choosing appropriate values of N.

After reduction of the higher order Principal Component(PC)s the number of the terms in the polynomial of $h(z)$ is M. In case of Hubble parameter the final

data	parameter	1σ	2σ	3σ
simulated	h_0	[0.244, 0.415]	[0.176, 0.504]	[0.12, 0.597]
	Ω_m	[0.567, 0.739]	[0.511, 0.864]	[0.47, 1.03]
	α_0	[-1.42, 1.64]	[-2.9, 3.14]	[-4.5, 4.6]
	α_1	[-2.76, 2.84]	[-5.64, 5.55]	[-8.3, 8.4]
	α_2	[-2.972, 2.96]	[-5.84, 5.02]	[-8.8, 8.9]
real	h_0	[0.26, 0.42]	[0.19, 0.51]	[0.135, 0.603]
	Ω_m	[0.598, 0.77]	[0.545, 0.888]	[0.503, 1.05]
	α_0	[-1.48, 1.44]	[-2.89, 2.87]	[-4.35, 4.34]
	α_1	[-2.797, 2.778]	[-5.48, 5.49]	[-8.23, 8.31]
	α_2	[-2.98, 2.92]	[-5.795, 5.837]	[-8.85, 8.773]

Table 3.1: The table gives 1σ, 2σ and 3σ ranges for the cosmological parameters, h_0, Ω_m, α_0, α_1 and α_2. $\vec{\alpha}$ are the parameters of dark energy equation of state.

functional form is,

$$h(z) = \sum_{i=1}^{M} \alpha_i u_i(z)$$

where, $(u_1(z), u_2(z), ..., u_N(z)$, and $U = G\mathcal{E}$. After the application of PCA the dimension of the coefficient space $\vec{\alpha}$ is M.

From the functional form of Hubble parameter, we can reconstruct the EoS $w(z)$, but the presence of a differentiation term in the equation to relate EoS with $h(z)$ increases the errors of reconstruction. In this work we address this problem. We suggest a new approach to bypass the differentiation in the process of calculating EoS from the PCA reconstructed Hubble parameter function. This has been done by combining PCA with the Maximum Likelihood technique (MLE), using Markov Chain Monte Carlo (MCMC). In the next section we explain the No-U-Turn sampler which is our choice of step selection in MCMC run. Then we introduce the method of selecting the data points from PCA reconstruction. Finally we explain the errors use in the MLE calculation.

3.2.2 No-U-Turn sampler

As discussed in sec(1.7.4), No-U-Turn sampler(NUTS) is a modification of the Hamiltonian Monte Carlo(HMC), where the algorithm intrinsically selects the Leapfrog steps. Selection of leapfrog steps are crucial to solve the Hamiltonian differential equations of the HMC. NUTS is very effective in choosing the best parameter region. To assess the MCMC methods we have to measure how good the MCMC estimates are, which could be done using autocorrelation time, or by the variance of the estimate, or the effective sample size. Autocorrelation of a variable measures the relationship between its present value with any of the past value which we can access. If instead of one value we compare the current series of values with the past historical data it is called autocorrelation time series. The classical sample techniques like Metropolis-Hasting or Hamiltonian Monte Carlo create autocorrelated samples if the number of continuous parameters are very large. NUTS works very effectively in the case of parameter space which consists of large number of continuous variables [125, 178, 179].

We use publicly available code PyMC3 for the implementation of MCMC. PyMC3 works more efficiently with the No-U-Turn sampler method. NUTS is especially useful on models that have many continuous parameters. For the models with many continuous parameters other MCMC algorithms are not very efficient.

Based on the gradient of the log posterior-density, NUTS takes advantage of where the regions of higher probability lies [125, 178]. This is the reason NUTS achieves the convergence faster on large problem sets than the traditional sample technique.

At every step, NUTS proceeds by creating a binary tree. In this binary tree, two particles which represent the progress in the forward and backward direction are created. If these two particles are represented as $(\mathbf{q_n^+}, \mathbf{p_n^+})$ and $(\mathbf{q_n^-}, \mathbf{p_n^-})$ then the NUTS can be given by,

$$(\mathbf{q}_n^+ - \mathbf{q}_n^-).\mathbf{p}_n^- < 0$$
$$(\mathbf{q}_n^+ - \mathbf{q}_n^-).\mathbf{p}_n^+ < 0$$

NUTS is an improvement of Hamiltonian Monte Carlo sampling, where we move in the phase space of $\mathbf{q}$ and $\mathbf{p}$ in the elliptical path [125, 179]. As discussed in sec(1.7.4) of Chapter(1) the motivation of introducing the momentum variable $\mathbf{p}$ is to ensure that we are exploring the greater area of the parameter space. This is done by moving in a elliptical contours, which we get after solving the dynamical Hamiltonian equation. In NUTS when we move half way of the elliptical path, the sign of the momentum and the position variables are changed and we stop, sec(1.7.4). This makes the NUTS more efficient than HMC, where there is no way to ascertain if we are moving in the already explored region of parameter space.

We choose the value of the total sample points M_s by checking the convergence limit using Gelman-Rubin statistic [178]. Gelman-Rubin statistic for convergence is based on the notion that multiple convergence chain appears to be similar to each other; otherwise, they will not converge. It is a standard method to run multiple MCMC chains to test for convergence. Scale reduction factor $\hat{r_o}$ is used to check the Gelman-Rubin convergence. There are two main ways in which the sequences of MCMC iterations can fail to converge. In one case, the chains run in the different parts which have drastic difference in posterior probability densities of the target distribution and in the another, the chains fails to attain the stationarity. We change the value of M_s until we get $\hat{r_o} = 1$.

3.2.3 Maximum likelihood calculation with PCA data-points

Here we replace the observational part of the Maximum Likelihood Estimation(MLE) calculation with PCA. This method also omits the dependencies on the number of observational data-points. MLE gives us a machinery to produce the most probable value of model parameters by constraining the theory with the observational data. The χ^2 is given by,

$$\chi^2_o(\vec{\beta}) = \sum_{i=1}^{n_d} \left(\frac{h^i_{th}(\vec{\beta}) - h^i_{obs}}{\sigma^i_{obs}} \right)^2 \tag{3.1}$$

where, $h(z)$ is the reduced Hubble parameter, n_d is the total number of data-points which we select from the PCA reconstructed curve and $\vec{\beta}$ is the parameter vector, which have all the parameters of the EoS along with reduced Hubble constant h_0 and density parameter Ω_m, $\vec{\beta} = \{h_0, \Omega_m, \vec{\alpha}\}$. h^i_{th} is the theoretical reduced Hubble parameter. For a spatially flat Universe, composed of dark energy and non-relativistic matter it is given by,

$$h^2(z) = h_0 \left[\Omega_m (1+z)^3 + \Omega_x e^{3\int_0^z \frac{1+w(z')}{1+z'} dz'} \right]^{1/2} \tag{3.2}$$

$$w(z') = \sum_{i=0}^{m} \alpha_i \mathcal{F}(z')^{(i-1)}, \quad \mathcal{F}(z) = \frac{z}{(1+z)} \tag{3.3}$$

To introduce PCA we replace the h_{obs} in eqn(3.1) with data-points selected from PCA reconstructed curve. Here, n_d is the total number of points being selected. Therefore, the final expression of χ^2 will be,

$$\chi^2_p(\vec{\beta}) = \sum_{i=1}^{n_d} \left(\frac{h^i_{th}(\vec{\beta}) - h^i_{pca}}{\sigma^i_{pca}} \right)^2 \tag{3.4}$$

In eqn(3.4), we replace the observed reduce Hubble parameter (h_{obs}) of Eqn(3.1) by the reconstructed functional form of PCA (h_{pca}). For the error part, we use

error-functions which are created from the co-variance matrix [126, 127, 174]. We use the analysis first for simulated data and then apply it to real datasets. The simulated dataset is created using the same parameter values as is fixed by [163]. For the simulated ΛCDM dataset we have fixed the values of cosmological parameters as, $\omega_m = 0.3$ and $h_0 = 0.684$. For the real dataset we use the Hubble parameter and redshift dataset [60–64].

In the present case, to get the reconstructed curve of reduced Hubble parameter for both simulated and real dataset we use $f(z) = \frac{z}{(1+z)}$ as initial basis function. This initial basis function gives the best reconstruction as has been shown in the chapter(2). Here in eqn(3.4), we have the freedom to choose the value of n_d, which is the number of data points in the observed part of MLE of eqn(3.1). We run the Markov Chain Monte Carlo (MCMC) chain to serch for minimum χ^2, which give us the likelihood of the PCA dataset. For this purpose, we use the PyMC3 program [178] with the No-U turn sampler method (NUTS) [125]. In the MCMC analysis we use normal priors $\mathcal{N}(0.70, 0.2)$ and $\mathcal{N}(0.35, 0.1)$ for reduced hubble constant h_0 and Ω_m respectively. For the DE parameters, $\vec{\alpha}$ we take $\mathcal{N}(0, 3)$. Here, $\mathcal{N}(x_{mean}, x_{mode})$ represents the normal probability density function with x_{mean} and spread of x_{mode}.

We choose the largest possible value for n_d which is limited by the computing power. We then check the results for different values of n_d and M_s and find out the mean, median and mode of the posterior distribution. For $m = 3$ eqn(3.3), we do the analysis for different values of n_d and M_s. $m = 3$ is the CPL parametrization with the next order term [180, 181]. n_d is varied in the range 100 to 800 whereas M_s in the range 1000 to 800000 and find out mean, median, mode as well as 1σ, 2σ, 3σ range of ω_m, h_0, $\vec{\alpha}$.

In Figures 3.2, 3.1, we show results for $n_d = 600$, where we fix the number of sample points at $M_s = 80,0000$. This particular choice of n_d and M_s gives us the closest approximation of the model parameters for the simulated data and we see that about this value of n_d and M_s we get the smallest variation in 1σ, 2σ and 3σ ranges of the model parameters. In particular for $(n_d, M_s) = (600, 800000)\&(1000, 50000)$ the difference in 1σ, 2σ and 3σ ranges are of the order of $\mathcal{O}(-1)$ for $\vec{\alpha}$ and $\mathcal{O}(-2)$ or less for Ω_m and h_0. To create the simulated data we assume $h_0 = 0.685$ and $\Omega_m = 0.3$, while the mean of the posterior of h_0 and Ω_m from the algorithm are $h_0 = 0.68$ and $\Omega_m = 0.34$, which are very close to the assumed values, $h_0 = 0.685$ and $\Omega_m = 0.3$. In table(3.1) we show the 1σ, 2σ, 3σ ranges for the parameters of the theory, eqn(3.2). Mean of the posterior of h_0 and

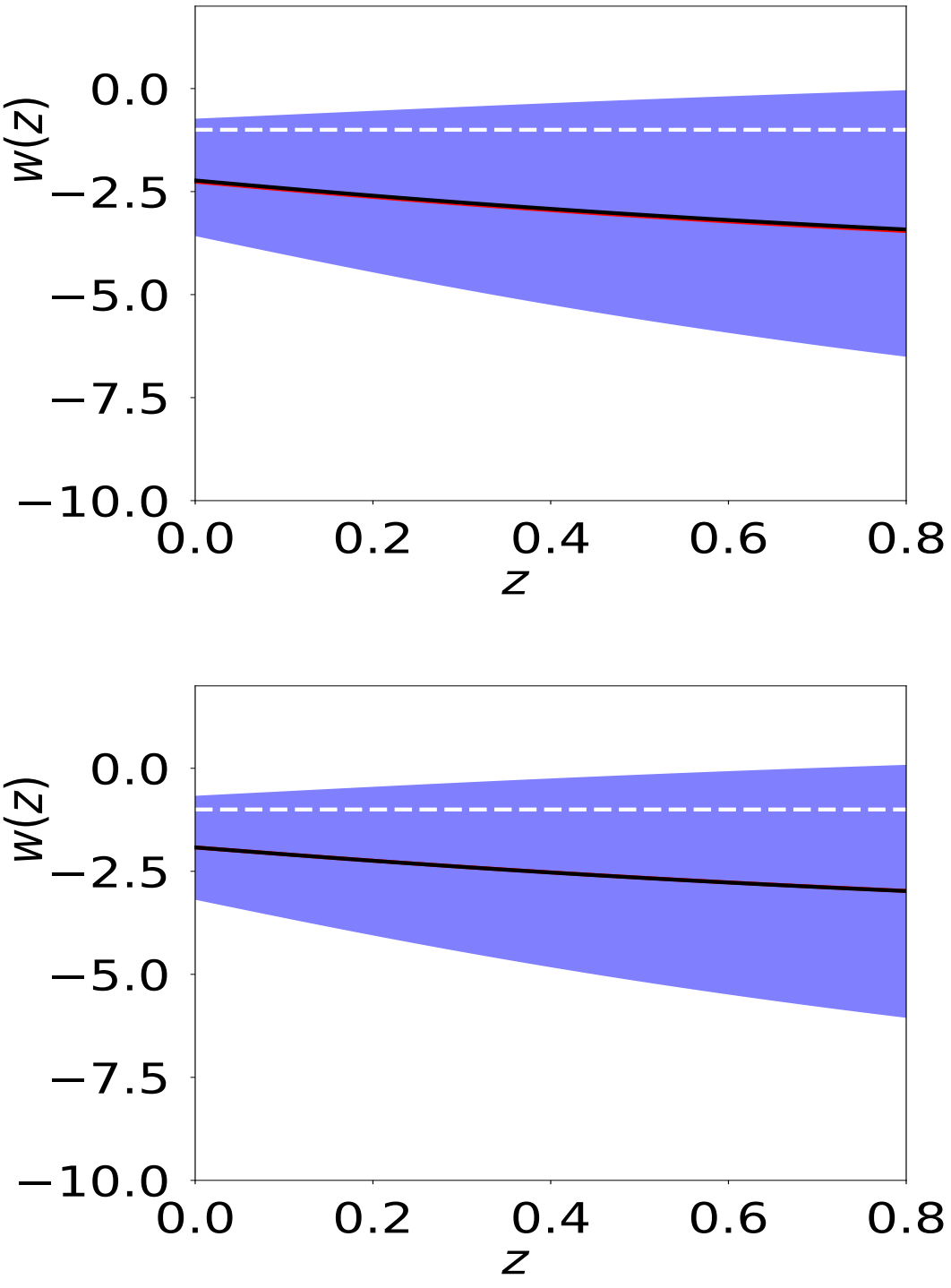

Figure 3.3: In this Figure, the blue bands are 1σ confidence level for the dark energy equation of state parameter $w(z)$. The upper plot is for the simulated dataset, and the lower one is for the real dataset. The value of observational points n_d and sample points M_s are 600 and 800000, respectively. The black and red curve are median and mean of the posterior density function. In both the curves, the white dotted line represents the $w = -1$ line.

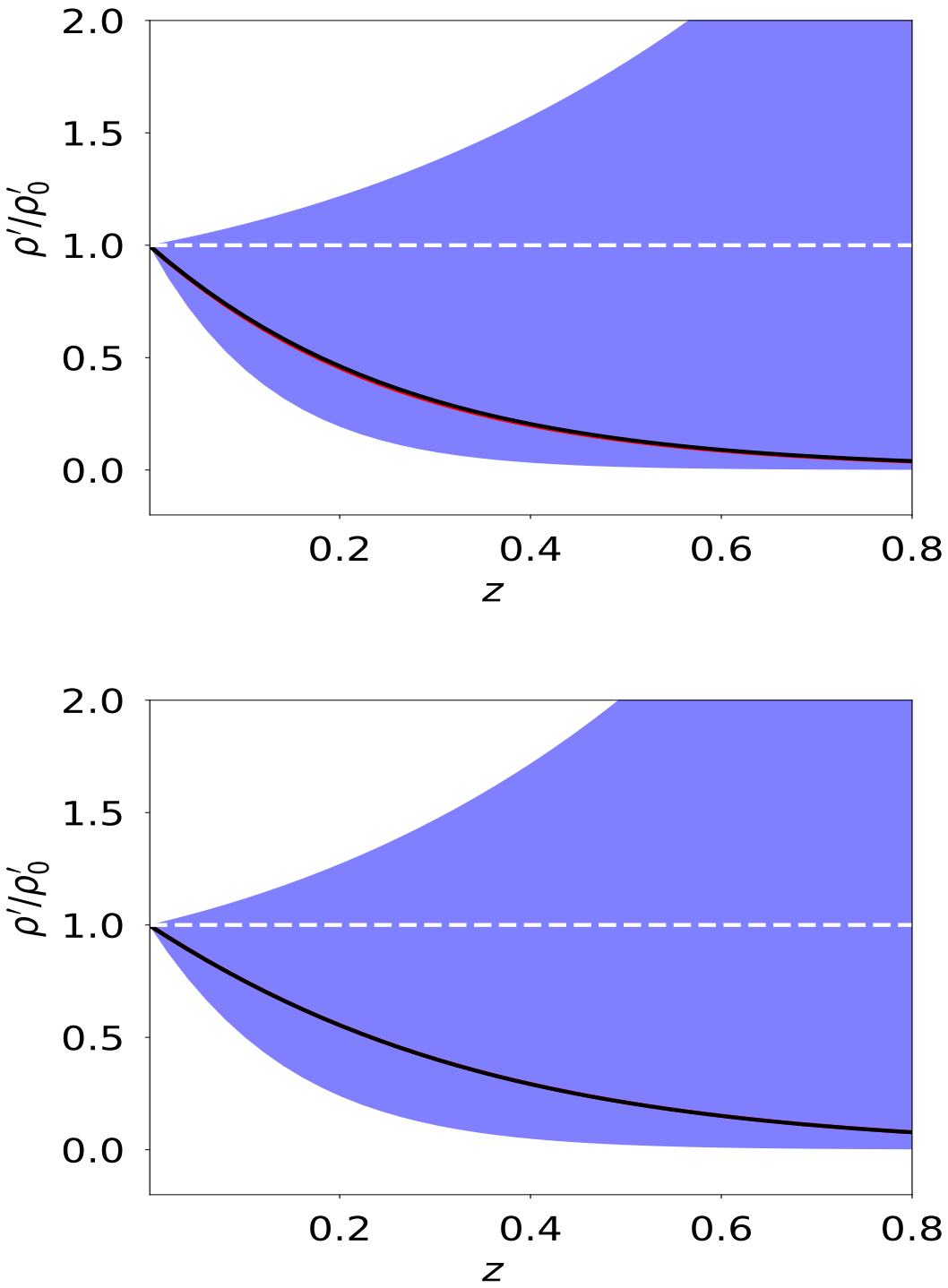

Figure 3.4: Plots represent the dark energy density ratio $\rho'(z)/\rho'_0$ as a function of redshift z. The upper plot is for the simulated data and the lower one is for the real dataset. In both the plots, blue patch represents the 1σ confidence range for $\rho'(z)/\rho'_0$. The white dotted line represents the $\rho'(z)/\rho'_0 = 1$ for the cosmological constant model. Number of data-points and number of sample points are, 600 and 800000 respectively.

Ω_m for the real data from the algorithm are $h_0 = 0.71$ and $\Omega_m = 0.35$ respectively.

It is also evident from the fig(3.3) that $w(z) = -1$ is well within the 1σ range of $w(z)$ parameters($\vec{\alpha}$). The plot of $w(z)$ and $\rho(z)/\rho_0$ are similar for both real and simulated dataset. Difference in $w(z)$ and $\rho(z)/\rho_0$ curve between simulated and real data are 0.442 and 0.024 respectively, fig(3.3, 3.4). The dark energy density plot fig(3.4), $\rho'(z)/\rho'_0$ vs z, for simulated and real dataset are also similar and the maximum difference between them is 0.36. The variation of 1σ, 2σ and 3σ ranges are negligible in the case of h_0, ω_m and $\vec{\alpha}$ when $n_d \geq 600$ and $M_s \geq 50000$.

For each MCMC run, we calculate the Gelman-Rubin convergence factor $\hat{r_o}$. We find that for the polynomial expansion in terms of $z/(1+z)$ as parametrization when $M_s \geq 10000$ gives $\hat{r_o} = 1$. In the PyMC3 run for both the real and simulated dataset, with $(n_d, M_s) = (600, 800000)$, the value of $\hat{r_o}$ is 1. To check the convergence we not only check the $\hat{r_o}$ factor and eliminate those iterations which do not satisfy the $\hat{r_o} \approx 1$ criteria but we also check the trace plots, rank bar plots and the rank vertical bar plots of the posterior sampling for visual confirmations [179, 182, 183].

Fig 3.5, 3.6, and 3.7 shows the convergence of the MCMC chains for the simulated dataset. These plots are created for $(n_d, M_s) = (600, 800000)$. For comparison we also show the same set of plots for $(n_d, M_s) = (100, 100)$, fig(3.8, 3.9, 3.10). The convergence and the ability to draw successful samples from the parameter space is apparent for $(n_d, M_s) = (600, 800000)$ set. For the $(n_d, M_s) = (100, 100)$ from the smoothed histogram plot we see that for each MCMC chains get different picks in MLE model. This means the low convergence of the MCMC chain using NUTS with $(n_d, M_s) = (100, 100)$. Figures 3.11, 3.12 and 3.13 shows same set of plots with real dataset.

In the likelihood analysis the error contribution comes from PCA algorithm, which is composed by the eigenvalues and eigenfunctions of the covariance matrix [126, 127, 174]. The eignevalues of the covariance matrix quantifies the error in the reconstruction of $h(z)$. If λ_i are the eigenvalues of the covariance matrix $\mathcal{C}$, then the error associated with each of the components is $\sigma(\alpha_i) = \lambda_i^{1/2}$. For M number of final terms we have the final error as,

$$\sigma(h(z_a)) = \left[\sum_{i=1}^{M} \sigma^2(\alpha_i) e_i^2(z_a)\right]^{1/2} \tag{3.5}$$

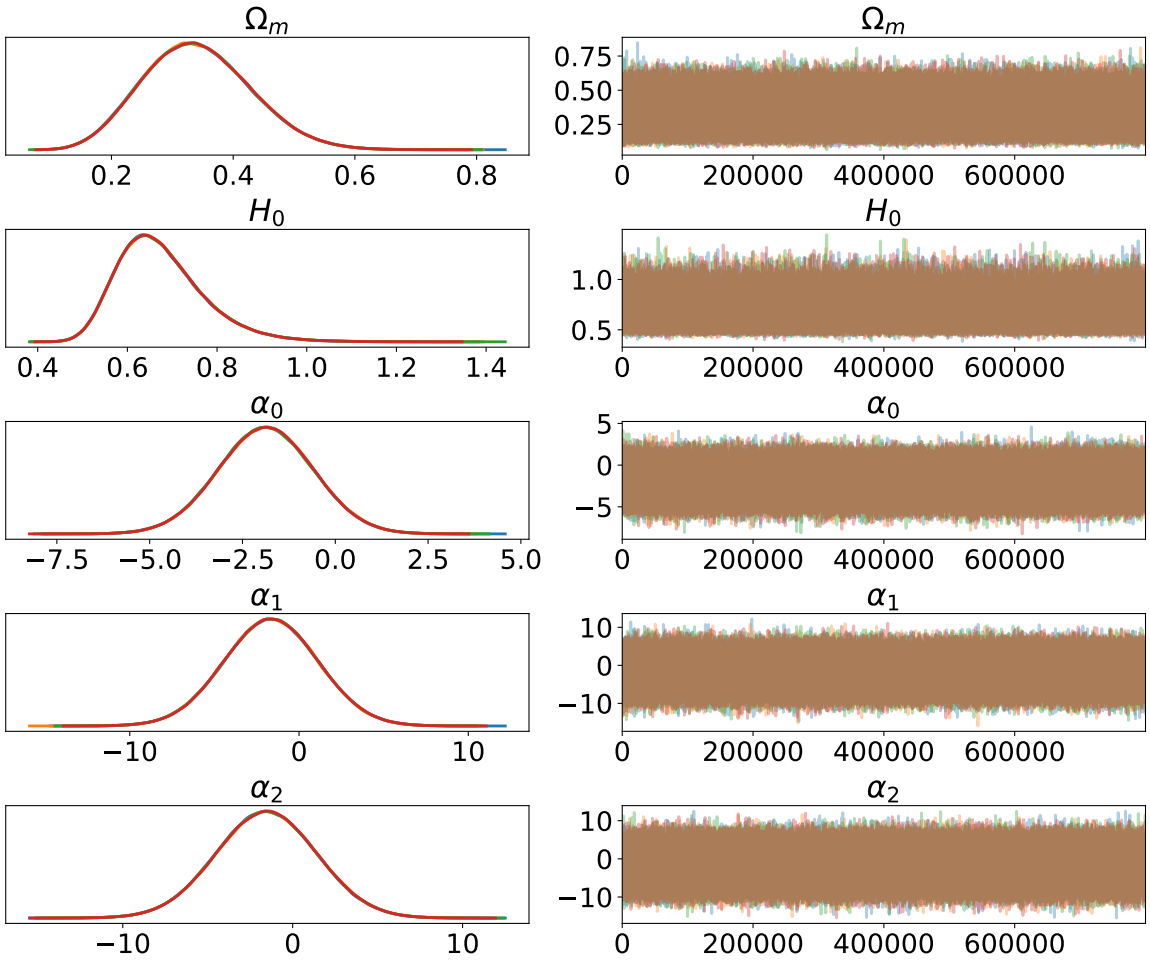

Figure 3.5: The left column consists of a smoothed histogram, using kernel density estimation of the marginal posteriors of each stochastic random variable. From the top to bottom the random variables are density parameter for matter Ω_m, reduced Hubble constant h_0 and the parameters of the equation of state of dark energy α_i. The right column contains the samples of the Markov chain plotted in sequential order. There are four MCMC chains which are plotted in different colours. These plots are created with $(n_d, M_s) = (600, 800000)$ and all are for simulated dataset.

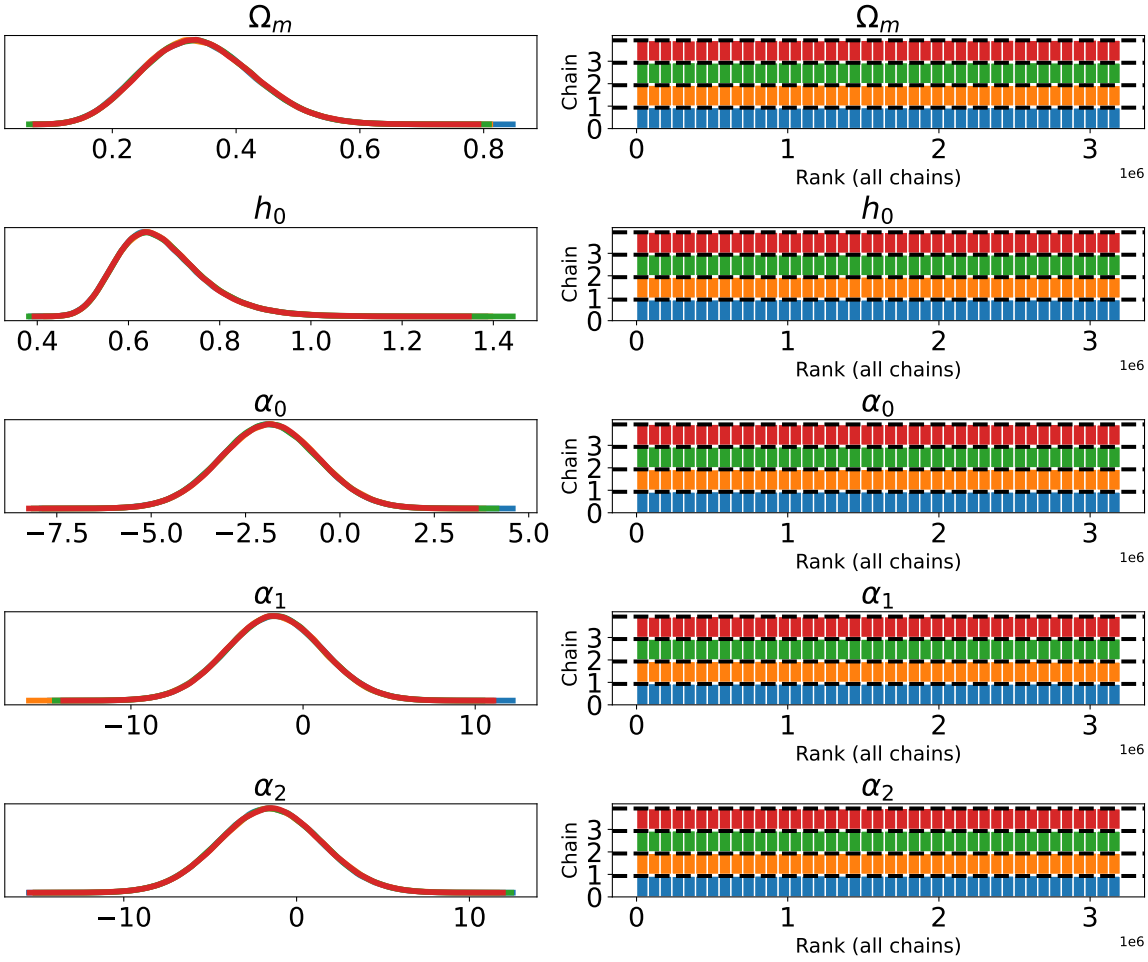

Figure 3.6: As in fig(3.5) the left column consists of a smoothed histogram, using kernel density estimation of the marginal posteriors of each stochastic random variable. From the top to bottom, the random variables are density parameter for matter Ω_m, reduced Hubble constant h_0 and the parameters of the equation of state of dark energy α_i. The right column shows the number of successful draws from the parameter space, which depends upon the sample size chosen as well as the prior theory. The four MCMC chains are plotted in different color and all are independent to each other. Simulated dataset is used to generate the plot and the number of sample point as well as the simulated points taken from the PCA curve are $(n_d, M_s) = (600, 800000)$.

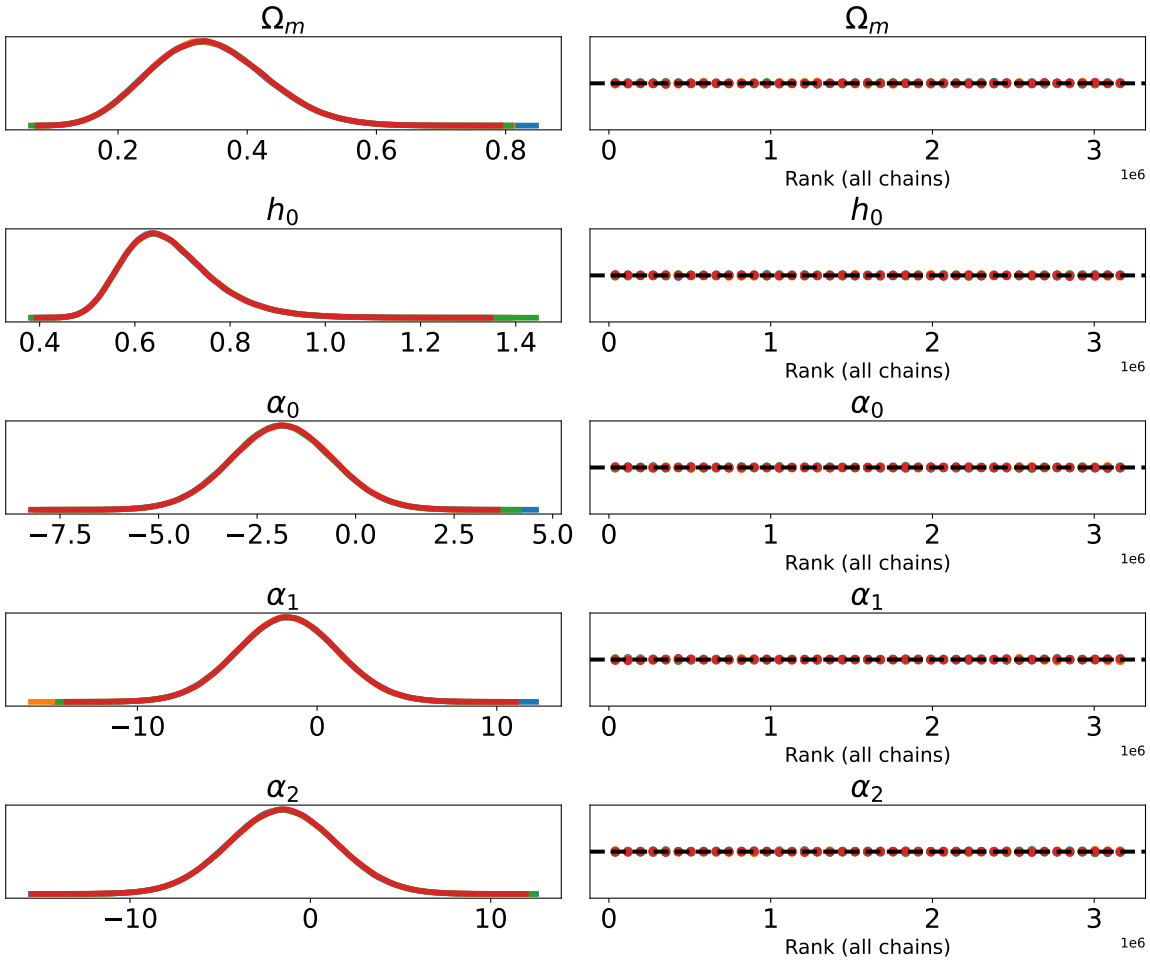

Figure 3.7: As in fig(3.5) the left column consists of a smoothed histogram, using kernel density estimation of the marginal posteriors of each stochastic random variable. As in the previous figures, the random variables are density parameter for matter Ω_m, reduced Hubble constant h_0 and the parameters of the equation of state of dark energy α_i. The right hand column gives the auto-correlation for all the random variables for all the four independent chains, which are depicted with the vertical lines. Simulated dataset is used to generate the plot and the number of sample point as well as the simulated points taken from the PCA curve are $(n_d, M_s) = (600, 800000)$.

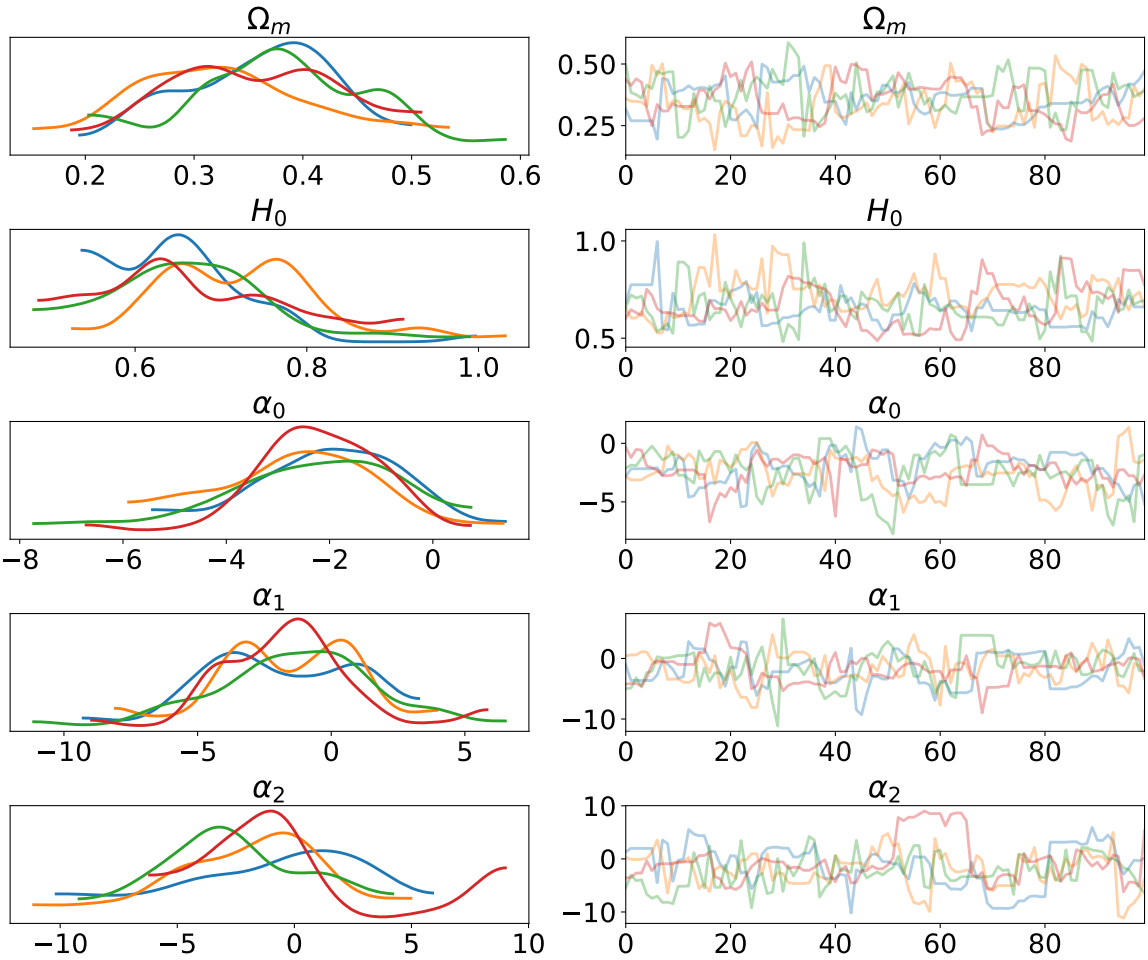

Figure 3.8: The left column consists of a smoothed histogram, using kernel density estimation of the marginal posteriors of each stochastic random variable. From the top to bottom the random variables are density parameter for matter Ω_m, reduced Hubble constant h_0 and the parameters of the equation of state of dark energy α_i. The right column contains the samples of the Markov chain plotted in sequential order. There are four MCMC chains which are plotted in different colours. These plots are created with $(n_d, M_s) = (100, 100)$ and all are for simulated dataset.

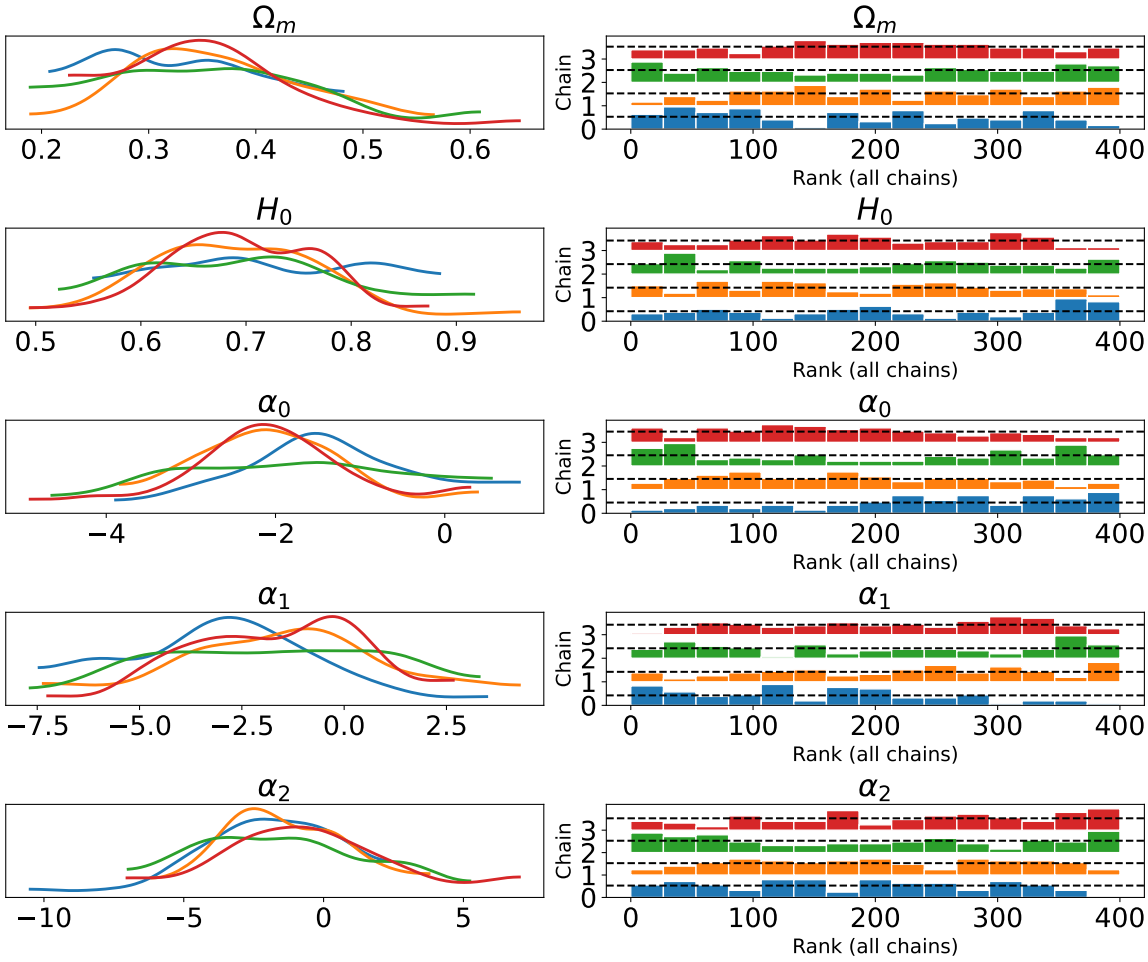

Figure 3.9: As in fig(3.8) the left column consists of a smoothed histogram, using kernel density estimation of the marginal posteriors of each stochastic random variable. The random variables plotted here are same as in the previous figures and in the same order. The right column shows the number of successful draws from the parameter space, which depends upon the sample size chosen as well as the prior theory. Simulated dataset is used to generate the plot and the number of sample point as well as the simulated points taken from the PCA curve are $(n_d, M_s) = (100, 100)$.

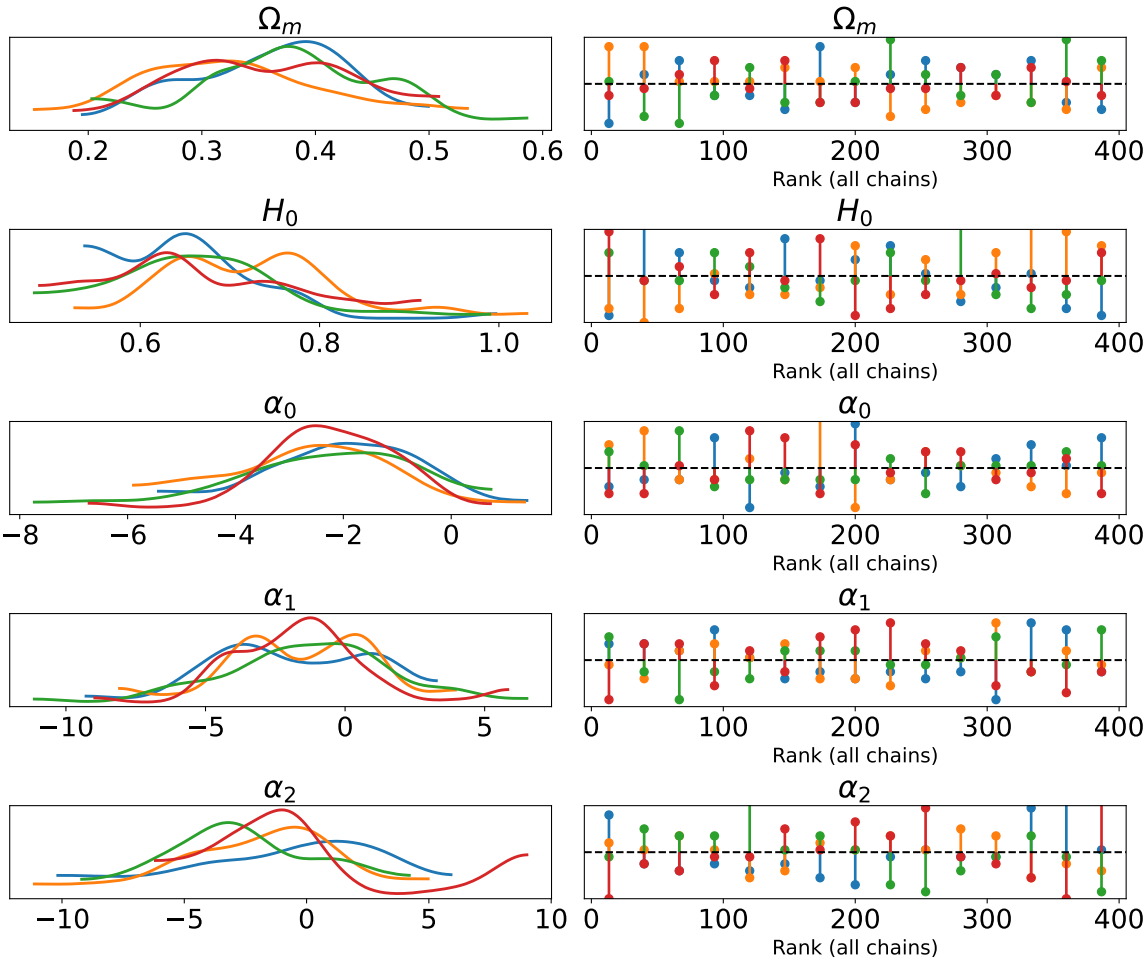

Figure 3.10: As in fig(3.8) the left column consists of a smoothed histogram, using kernel density estimation of the marginal posteriors of each stochastic random variable. The right hand column gives the auto-correlation for all the random variables for all the four independent chains, which are depicted with the vertical lines. Simulated dataset is used to generate the plot and the number of sample point as well as the simulated points taken from the PCA curve are $(n_d, M_s) = (100, 100)$.

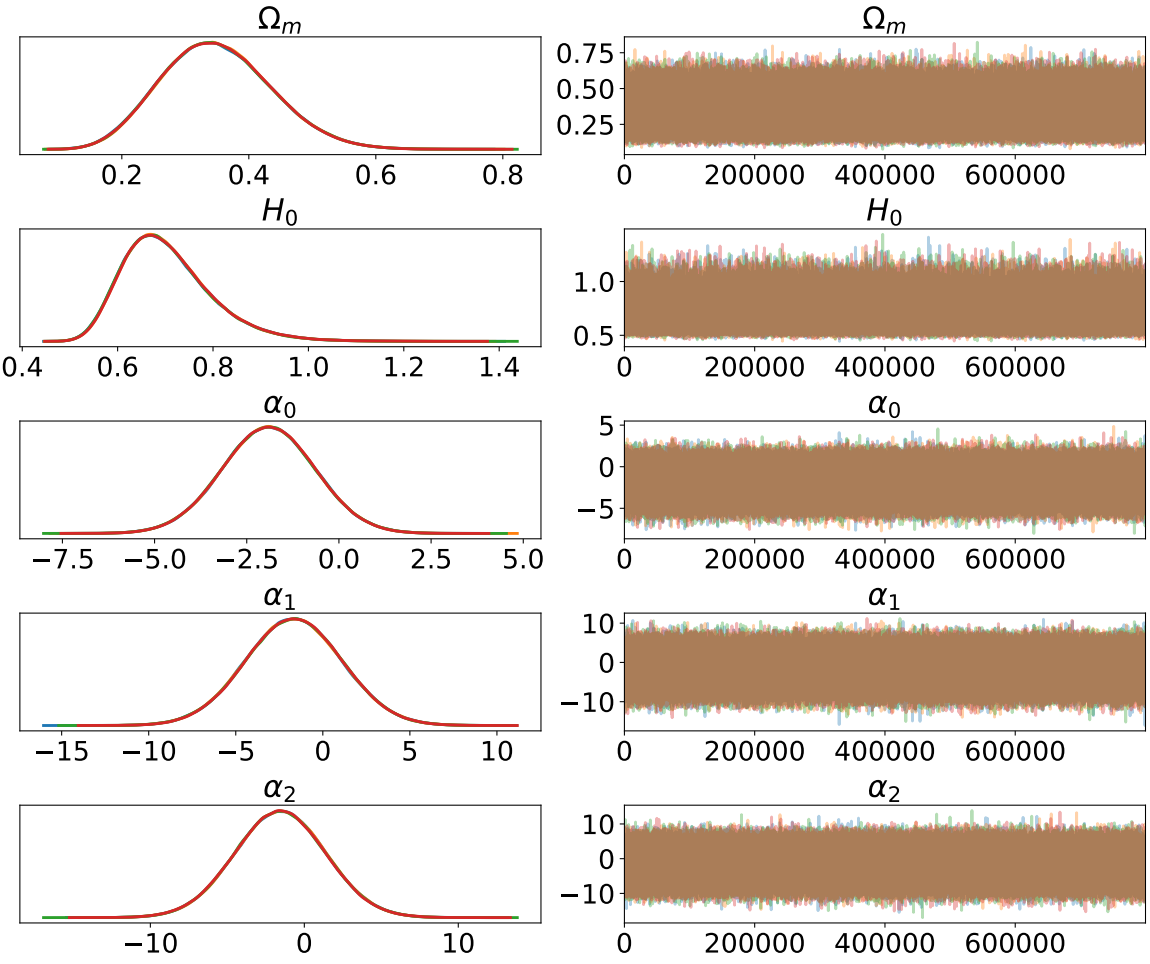

Figure 3.11: The left column consists of a smoothed histogram, using kernel density estimation of the marginal posteriors of each stochastic random variable. The right column contains the samples of the Markov chain plotted in sequential order. These plots are created with $(n_d, M_s) = (600, 800000)$ and all are for real Hubble parameter dataset.

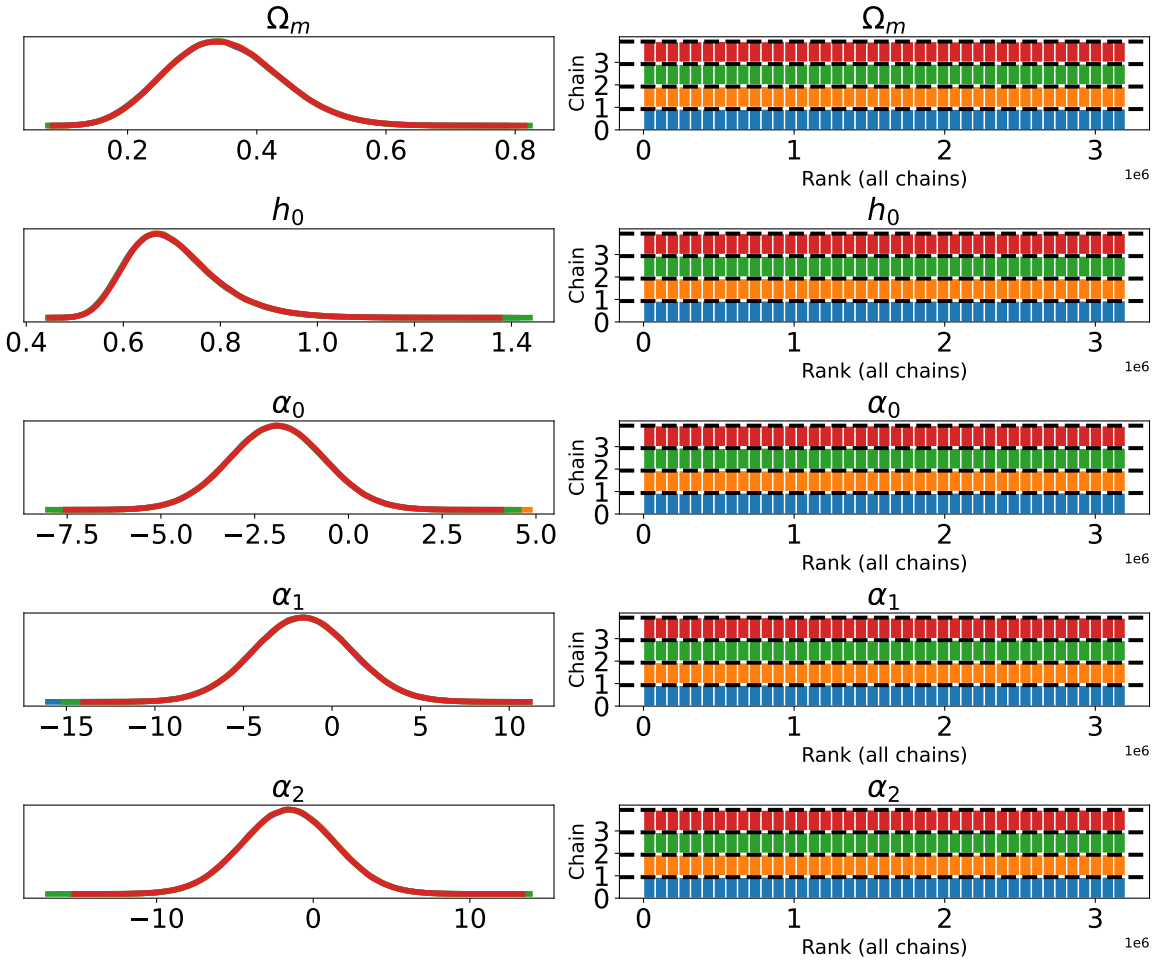

Figure 3.12: As in fig(3.6) the left column consists of a smoothed histogram, using kernel density estimation of the marginal posteriors of each stochastic random variable. The random variables plotted here are same as in the previous figures and in the same order. The right column shows the number of successful draws from the parameter space, which depends upon the sample size chosen as well as the prior theory. The four MCMC chain plotted in different color and all are independent to each other. Real Hubble parameter dataset is used to generate the plot and the number of sample point as well as the simulated points taken from the PCA curve are $(n_d, M_s) = (600, 800000)$.

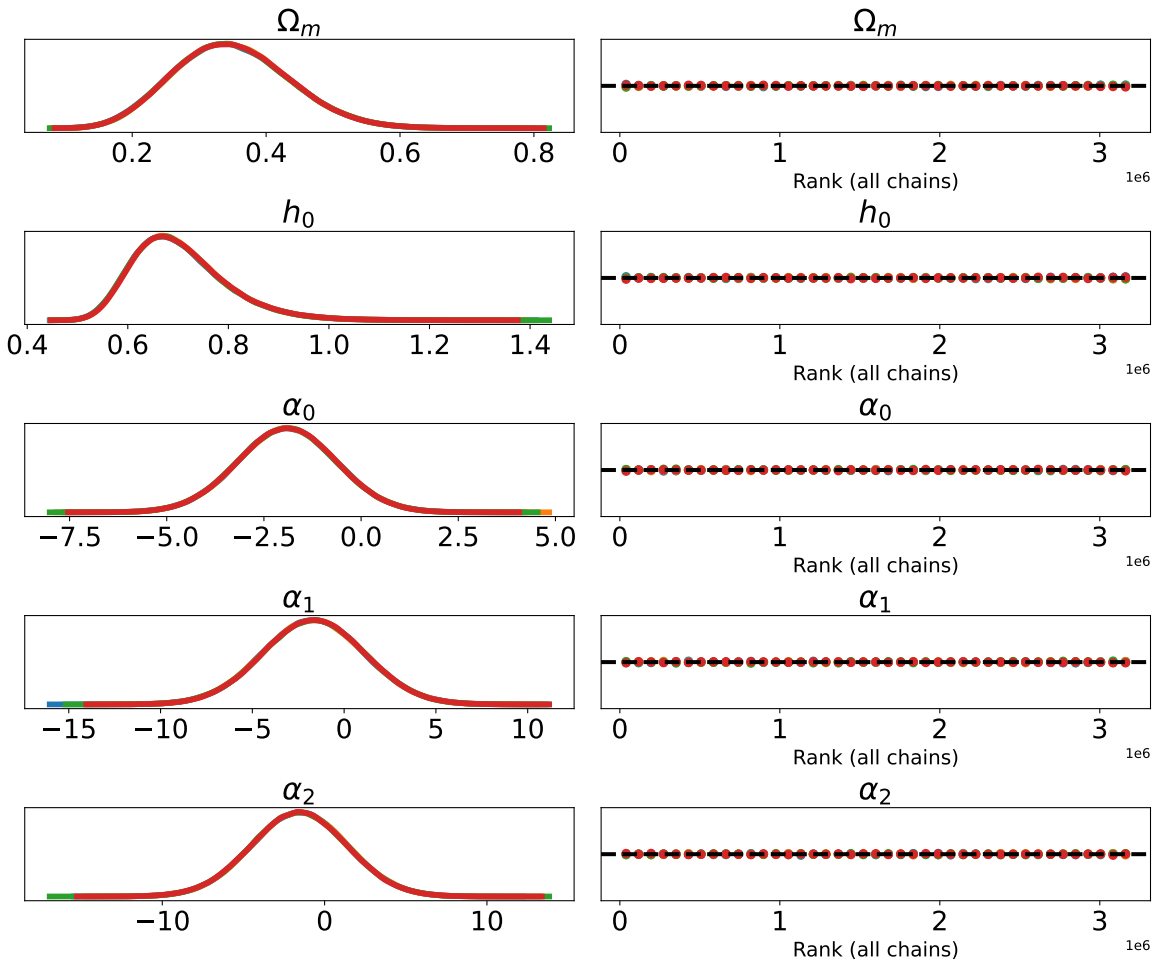

Figure 3.13: As in fig(3.5) the left column consists of a smoothed histogram, using kernel density estimation of the marginal posteriors of each stochastic random variable. The right hand column gives the auto-correlation for all the random variables for all the four independent chains, which are depicted with the vertical lines. In this case, real Hubble parameter dataset is used to generate the plot and the number of sample points as well as the simulated points taken from the PCA curve are $(n_d, M_s) = (600, 800000)$.

Eqn(3.5) gives the error function for a particular reconstructed curve. We have the error as a function of redshift z_a. We use this error function in the likelihood analysis.

From the figure (A.1 - A.7) we see that NUTS and Hamiltonain Monte Carlo sampler (HMC) are better than Matropolis Hasting sampler (MH). For HMC and MH, we take same number of simulated datapoints and sample points as in the case of NUTS $(n_d, M_s) = (600, 800000)$. In between HMC and NUTS, NUTS is better than HMC as NUTS picks up the leapfrog steps and it automatically stops when the NUTS conditions are satisfied, sec(1.7.4). For comparison we use the same number of simulated datapoints n_d as well as the sample points M_s as in NUTS simulation, these are $(n_d, M_s) = (600, 800000)$ A.

3.3 Conclusion

When the method of PCA reconstruction is combined with MCMC tool, we have the freedom of selecting the number of points in the observational part of maximum likelihood estimation. This gives us a reasonable prediction of the parameters of a model. Here we use NUTS sampling technique with a specific parametrization form of DE. Also, we utilise the combined PCA and MCMC only on the Hubble parameter dataset. We show that the parameter estimation is independent of the prior probability assumption, and the idea can be generalized to other datasets as well as different sampling techniques. The input of PCA reconstuction part of the methodology is only the observational dataset. We need to do the PCA reconstruction before the Maximum Likelihood Estimation(MLE) calculation. Combination of PCA reconstruction with MCMC (MCMC + PCA), for the MLE is independent of any errors that may appear due to differentiation of the PCA reconstructed quantity, particularly the first-order differentiation of $h(z)$ to infer the value of $w(z)$. Here we only use the error function that comes from the PCA algorithm, and one can use different error functions in the error part of the MLE as well. It can be used as a model selection tool and can be used in those dataset which has a fewer data-points.

Chapter 4

Summary and Future Directions

With the development of sophisticated theoretical models and also the increasing availability of large observational datasets, the dark energy study has taken a big leap. Along with the theoretical and observational aspects, statistical methods are being developed, created and applied in the dark energy study. In this thesis, we employ Principal Component Analysis(PCA), which is a model-independent, non-parametric method to cosmic chronometer and distance modulus datasets. We develop a variant of PCA which can reconstruct the functional form of the reconstructed quantity from the tabulated dataset of the same. This functional form can also help us in constraining the parameter space of different dark energy models.

In the second chapter, we reconstruct the late-time cosmological quantities using PCA. We reconstruct the observables of cosmic chronometer and distance modulus datasets, which are Hubble parameter $H(z)$ and distance modulus $\mu(z)$. The input of our methodology is the dataset of the quantity we want to reconstruct. Both $H(z)$ and $\mu(z)$ dataset give us tabulated data for $H(z)$ and $\mu(z)$, where we have different values of $H(z)$ and $\mu(z)$ for different redshifts(z). For the application of PCA we do not need any prior information on the distribution of different quantities of the dataset. PCA is a model-independent technique, and it is used to separate the noise of the data from the signal part. The method is non-parametric in the sense that no additional parameters are needed for its application in datasets.

Principal Component Analysis is an application of linear algebra, and we need only the tabulated dataset of the observational quantity as our input. As an output, we get the functional form of the observable in terms of the independent

variable of the dataset. It is crucial in our PCA methodology to find the correlations of the dataset. We start with a polynomial expression of the observable over an independent basis variable. We use $(1-a)$, a and z as our initial basis variable, where a and z are the scale factor and redshift, respectively. Selection of one basis variable over the other is done by the correlation coefficient calculation (CCC). We calculate Pearson, Spearman, and Kendall correlation coefficients to check the linear and non-linear correlation of the datasets. We show that a combination of CCC and PCA (PCA + CCC) can be used as a potential reconstruction tool. The polynomial expression over a particular variable creates the coefficients space. The dimension of this coefficient space N is equal to the number of terms in the polynomial expression of the dependent variable. CCC determines the dimension of the coefficient space. We choose that value of N for which the linear correlation is larger than the non-linear correlation. For a particular independent variable, the dimension of the coefficient space also depends upon the computational power we have. After the selection of the number of terms of the polynomial, we divide the whole coefficient space into patches and apply χ^2 minimization in each of these patches. For each patch, we get the best-fit point of coefficient space. We apply PCA in this set of points. CCC also quantifies how efficiently PCA can break the linear correlation for a particular independent variable. (PCA + CCC) gives an algorithm for selecting the number of final principal components which are sufficient to reconstruct the observable quantity. First, we apply our algorithm in the simulated dataset to check the efficiency of our algorithm. There are two approaches to our PCA mechanism. The first one is a derived approach, where we reconstruct the observable quantity using PCA and subsequently construct the dark energy equation of state parameter $w(z)$. The other approach is the direct reconstruction of $w(z)$. We use different initial basis variables to reconstruct the observable quantities and use CCC to select one particular initial basis variable over the other. Given the dataset, we use CCC to choose one approach over the other. The derived approach is selected over the direct approach as well as $(1-a)$ over the variables a and z as the better-reconstructed variable. The reconstruction of the equation of state indicates a slowly varying equation of state of dark energy.

In the Chapter 3, we combine PCA and Markov Chain Monte Carlo (MCMC) to infer the model parameters of a particular model. We first find out the functional form of the observable $H(z)$ from the Cosmic Chronometer dataset, using the (PCA + CCC) method. In the reconstruction part of the PCA, we assume a polynomial form of $H(z)$ over the variable $(1-a)$. The CCC analysis determines the number of terms in the polynomial. (PCA + CCC) gives us the functional form of the dependent variable in terms of the independent variable in a non-

parametric manner. We select several points from the functional form of $H(z)$. Error in PCA reconstruction is dependent upon the eigenvalues and eigenvectors of the covariance matrix. In the error part of the MLE calculation we use the error comes intrinsically from the PCA analysis. We then use *No U Turn Sampler* (NUTS) as a sampling technique to run the MCMC chains in the model parameter space. Here we try to constrain the parameters of a particular dark energy model with the functional form of $H(z)$ that comes from the PCA reconstruction. We assume a test model for the dark energy equation of state parameter ($w(z)$), which is a polynomial over the variable $(1 - a)$. For simplicity, we take only the initial three terms of the polynomial expression of $w(z)$ over $(1 - a)$. We aim to replace the usual observational part of the MLE calculation with the PCA part. When the method of (PCA + CCC) reconstruction is combined with MCMC tool, we have the freedom of selecting the number of points in the PCA part of MLE. We see that the predictions for the model parameters are reasonable.

Here we utilize the combined (PCA + CCC + MCMC) algorithm only on the Hubble parameter dataset. We show that the parameter estimation is independent of the prior probability assumption, and the idea can be generalized to other datasets. The relation between the Hubble parameter and the equation of state of dark energy also contains the first differentiation of the Hubble parameter, which introduce some unwanted error in the equation of state predictions in (PCA + CCC) method. (PCA + CCC + MCMC) method eliminates the error that appears from the first-order differentiation of the Hubble parameter to infer the value and ranges of the Equation of State of dark energy. In this work, we only use the error function that comes directly from the PCA algorithm. (PCA + CCC + MCMC) can be used as a model selection tool and can be used in those datasets which has fewer number of data-points.

The methods discussed here are effective in constraining the cosmological parameters as well as applicable to diverse datasets. One of our future goals is to find an algorithm that can inclusively select the best initial basis variable over a set of variables for a fixed computational power and a fix dataset. Another direction is the use of different cosmological data and their combination to find the combined contours of the cosmological parameters.

Appendix A

Maximum Likelihood Estimation with Hamiltonian Monte Carlo and Metropolis Hasting sampling technique on the reconstruction of Principal Component Analysis

In this section we add the figures using the same method of chapter(3.3) of sec(3.2), but with Hamiltonian Monte Carlo(HMC) and Metropolis Hasting(MH) sampling technique. MH and HMC are described in sec(1.7.4). Here we add the trace figures with the rank bar and auto-correlation plots. Plots are for the same number of simulated datapoints n_d as well as the sample points M_s as in NUTS simulation, which are $(n_d, M_s) = (600, 800000)$. Below we brief the HMC and MH methods.

Metropolis Hasting (MH) : Due to the simplicity it is one of the most popular sampling technique. It is a kind of Markovian accept reject algorithm. In general if the $\vec{\theta}$ are the set of parameters then in MH we start with a proposal distribution $q(\theta_{i+1}|\theta_i)$, which gives the probability of getting the parameter point θ_{i+1} when the current position θ_i is given. The acceptance probability is given by $\alpha(\theta_{i+1}|\theta) = min\{1, r\}$, where

$$r \equiv \frac{\mathcal{P}(\theta_{i+1})q(\theta_i|\theta_{i+1})}{\mathcal{P}(\theta_i)q(\theta_{i+1}|\theta_i)}$$

r is called the Hasting ratio and in the symmetry case $q(\theta_i|\theta_{i+1}) = (\theta_{i+1}|\theta_i)$. We start the sampler by the maximum a posteriori (MAP) value calculated using PyMC3, where MAP is found out using numerical optimization methods.

Hamiltonian Monte Carlo(HMC): In HMC with the regular variables, which is called the position variables $\mathbf{p}$, we introduce the auxilary field variable, called the momentum variable $\mathbf{p}$. These two variables create the Hamiltonain variable $H(\mathbf{p}, \mathbf{q}) = U(\mathbf{q}) + K(\mathbf{p})$. We move in the parameter space in the path, which we get by solving the Hamiltonian canonical equations of $\mathbf{q}$ and $\mathbf{p}$, sec(1.7.4). In this case also we start the sampler with the maximum a posteriori (MAP) value calculated using PyMC3.

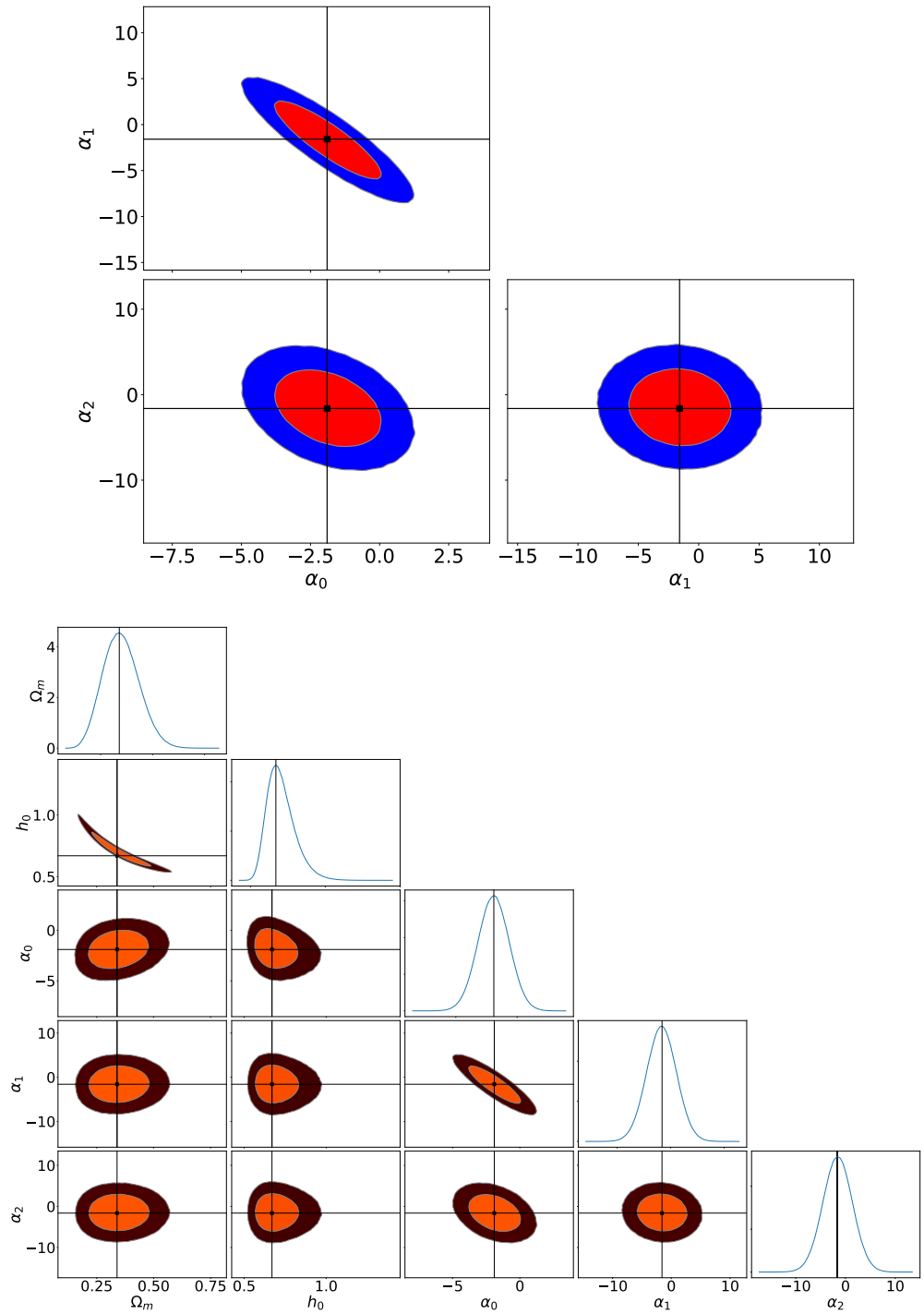

Figure A.1: This plots are done using the Hamiltonian Monte Carlo sampler(HMC). Figure in the top shows the 1σ, 2σ and 3σ for the three parameters of equation of state parameter (EoS)in the case of simulated dataset. Bottom figure represents the 1σ, 2σ and 3σ contours for all the parameter presents in the dataset along with their marginal probability density plots for the real dataset.

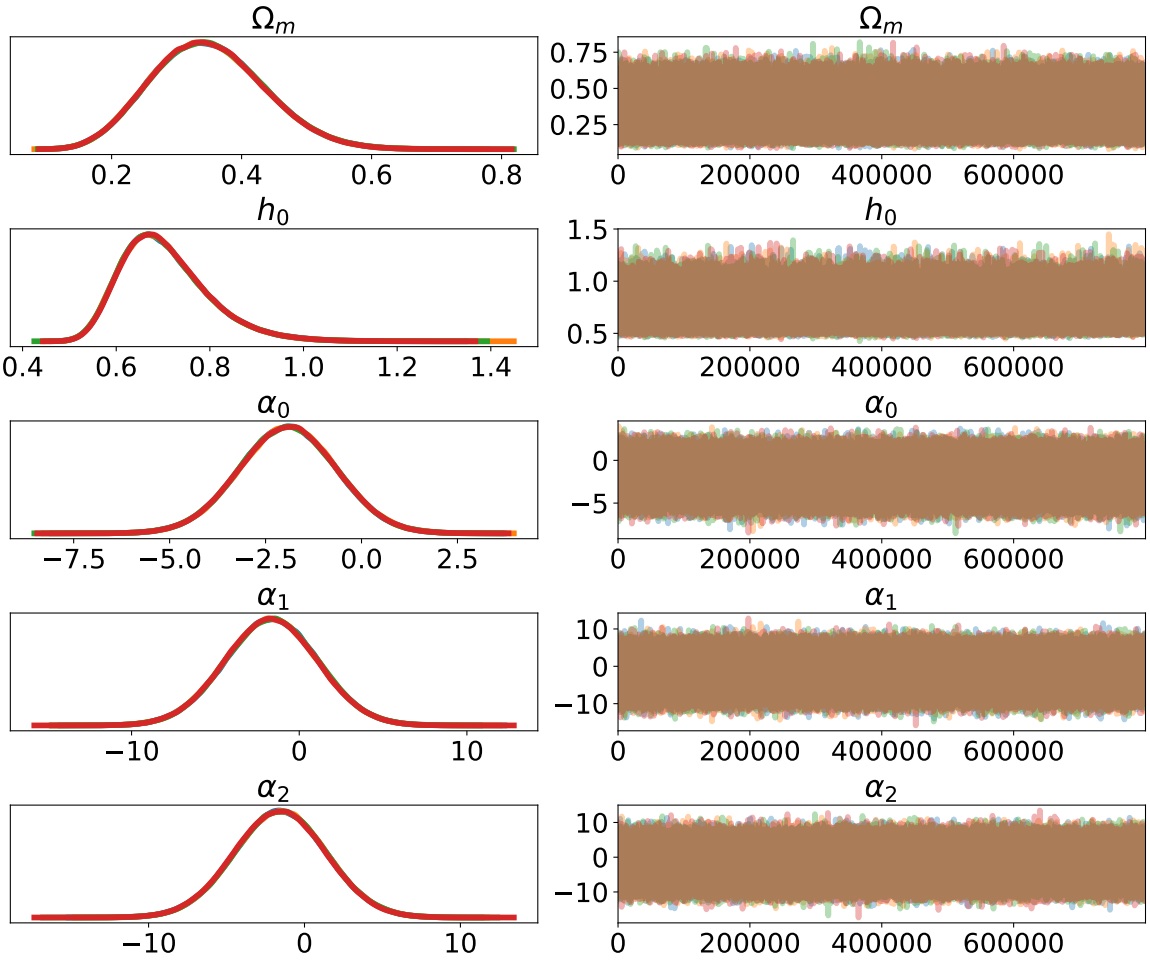

Figure A.2: This plots are done using the Hamiltonian Monte Carlo sampler(HMC). The left column consists of a smoothed histogram, using kernel density estimation of the marginal posteriors of each stochastic random variable. From the top to bottom the random variables are density parameter for matter Ω_m, reduced Hubble constant h_0 and the parameters of the equation of state of dark energy α_i. The right column contains the samples of the Markov chain plotted in sequential order. There are four MCMC chains which are plotted in different colours. These plots are created with $(n_d, M_s) = (600, 800000)$ and all are for real Hubble parameter dataset.

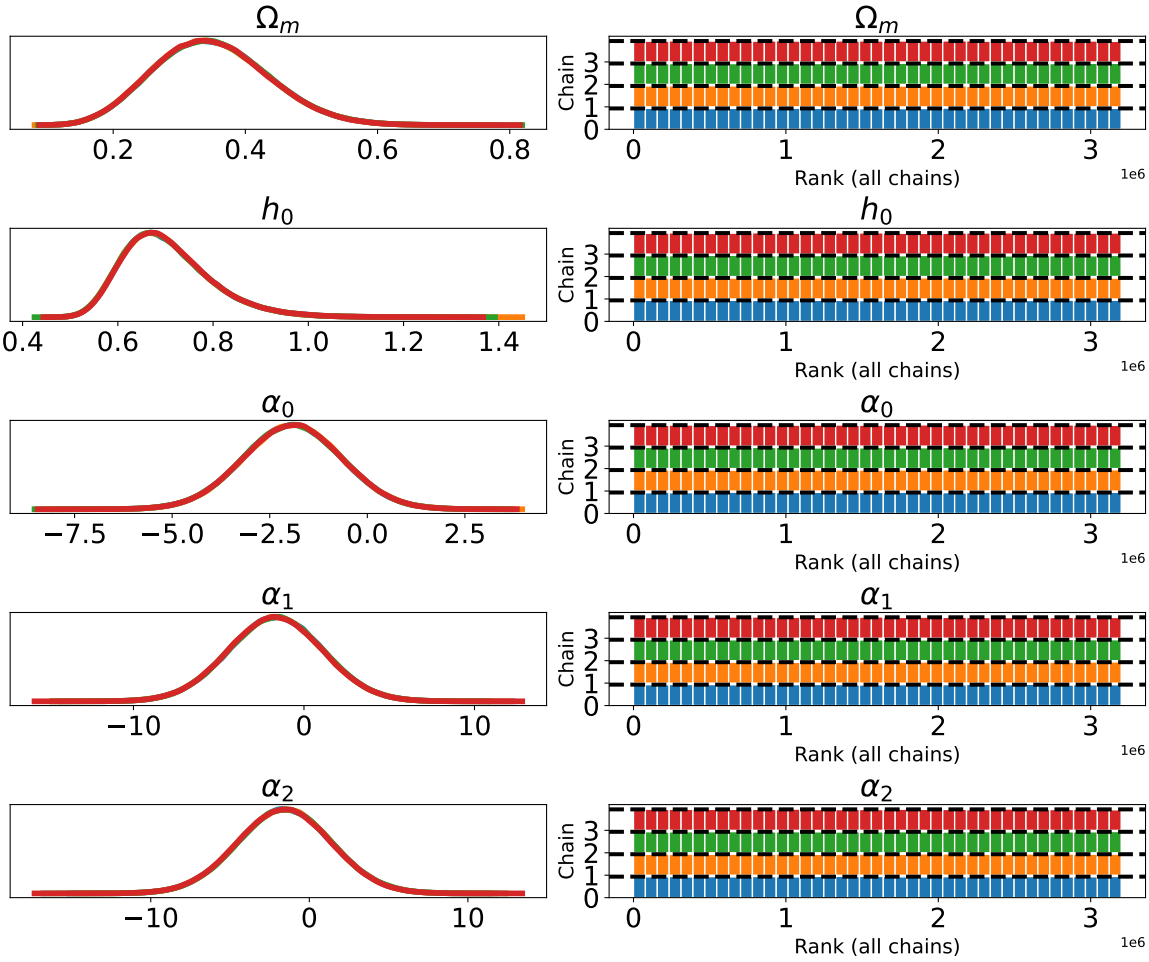

Figure A.3: This plots are done using the Hamiltonian Monte Carlo sampler(HMC). As in fig(3.6) the left column consists of a smoothed histogram, using kernel density estimation of the marginal posteriors of each stochastic random variable. From the top to bottom the random variables are density parameter for matter Ω_m, reduced Hubble constant h_0 and the parameters of the equation of state of dark energy α_i. The right column shows the number of successful draws from the parameter space, which depend upon the sample size chosen as well as the prior theory. The four MCMC chain plotted in different color and all are independent to each other. Real Hubble parameter dataset is used to generate the plot and the number of sample point as well as the simulated points taken from the PCA curve are $(n_d, M_s) = (600, 800000)$.

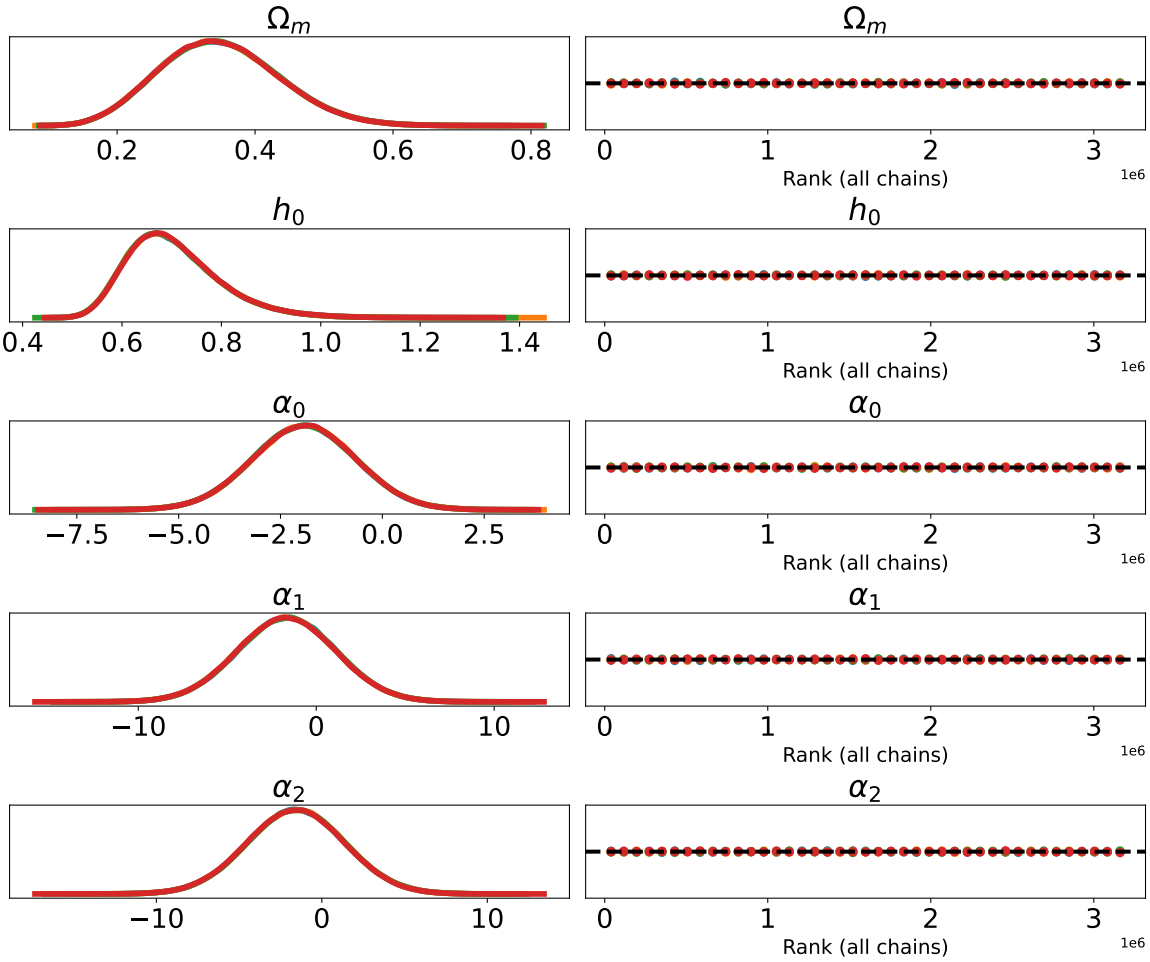

Figure A.4: This plots are done using the Hamiltonian Monte Carlo sampler(HMC). As in fig(3.5) the left column consists of a smoothed histogram, using kernel density estimation of the marginal posteriors of each stochastic random variable. The random variables plotted here are same as in the previous figures and in the same order. The right hand column gives the auto-correlation for all the random variables for all the four independent chains, which are depicted with the vertical lines. Real Hubble parameter dataset is used to generate the plot and the number of sample points as well as the simulated points taken from the PCA curve are $(n_d, M_s) = (600, 800000)$.

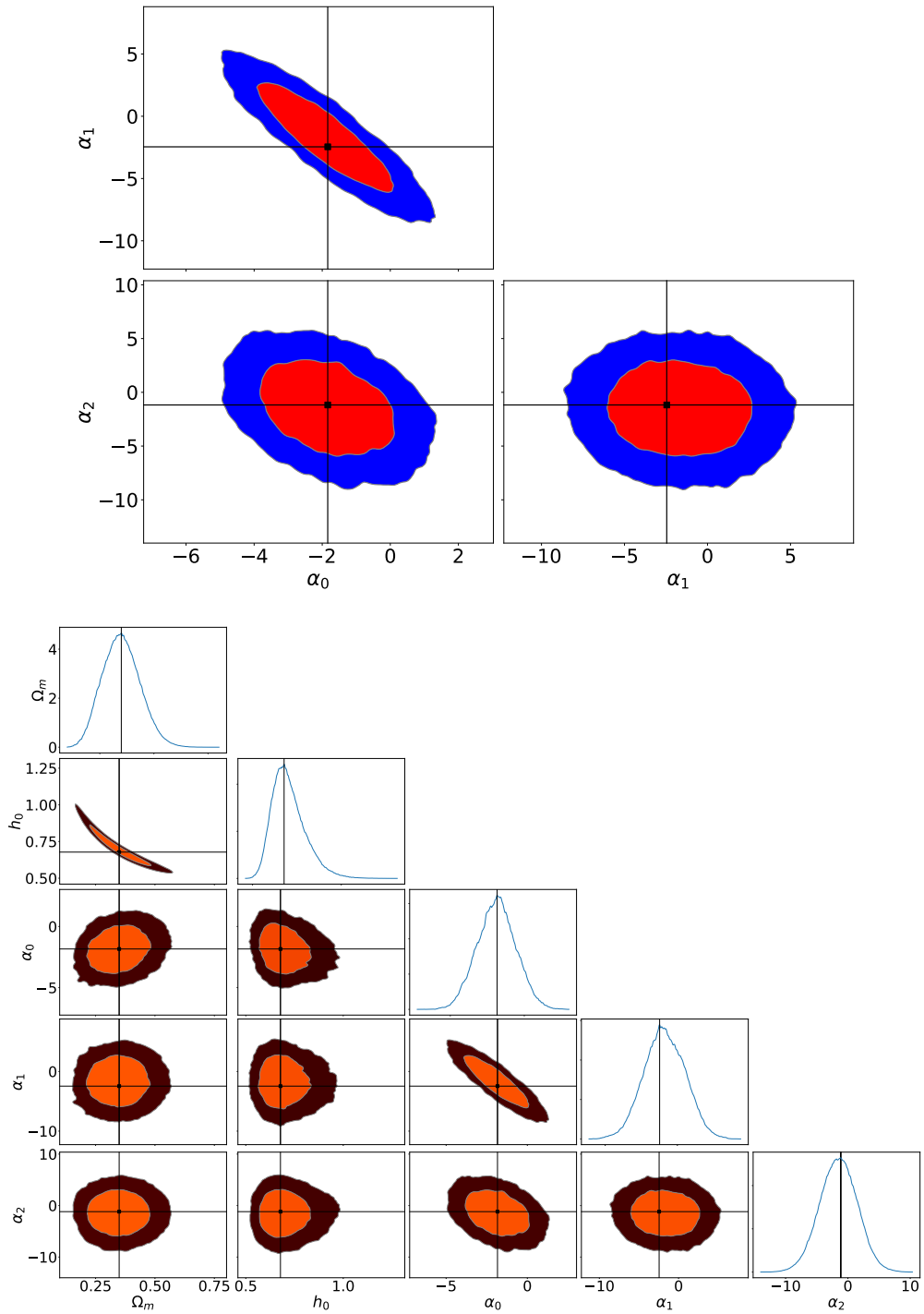

Figure A.5: This plots are done using the Metropolis Hasting sampling technique (MH) Figure in the top shows the 1σ, 2σ and 3σ contours for the three parameters of equation of state parameter(EoS) in the case of simulated dataset. Bottom figure represents the 1σ, 2σ and 3σ contours for all the parameter presents in the dataset along with their marginal probability density plots for the real dataset.

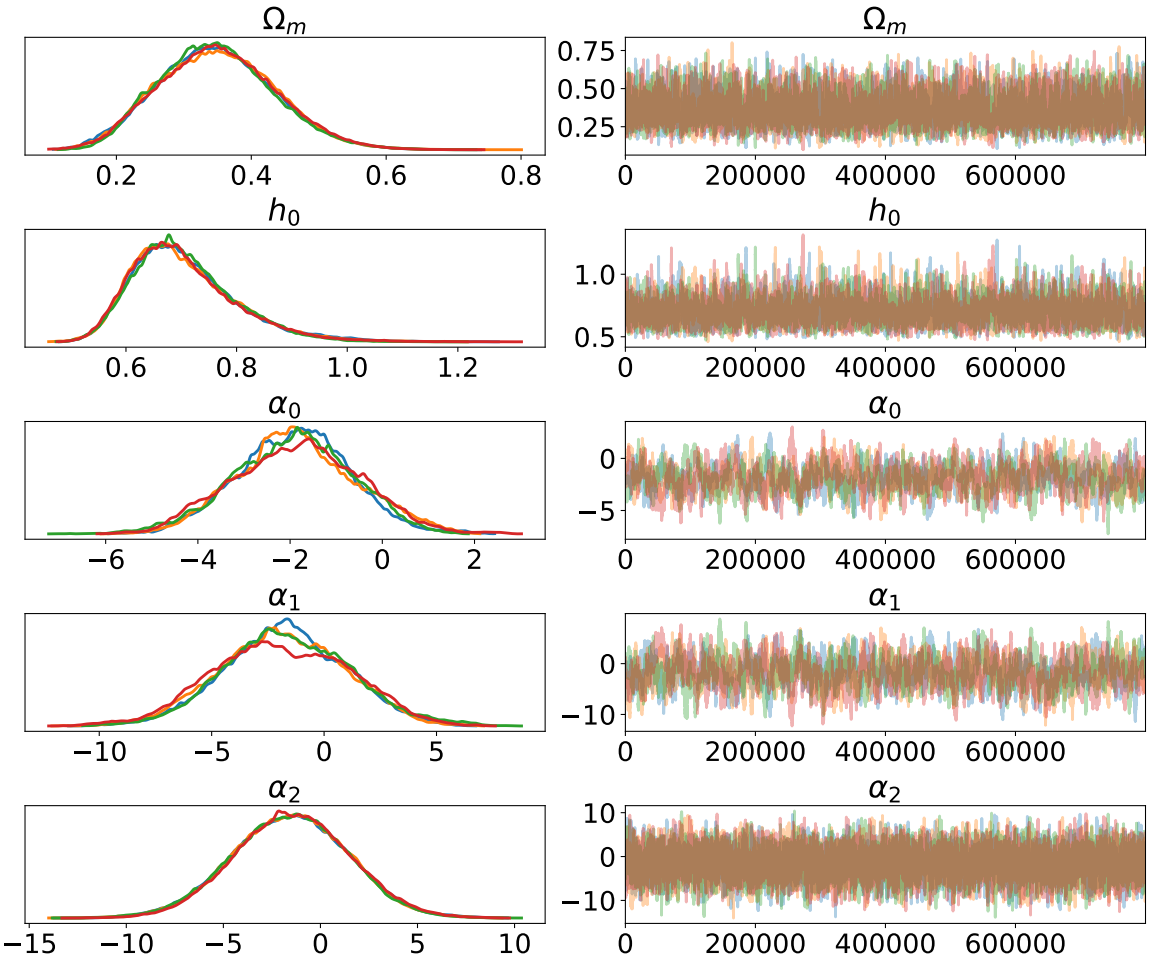

Figure A.6: This plots are done using the Metropolis Hasting sampling technique (MH) The left column consists of a smoothed histogram, using kernel density estimation of the marginal posteriors of each stochastic random variable. The right column contains the samples of the Markov chain plotted in sequential order. There are four MCMC chains which are plotted in different colours. These plots are created with $(n_d, M_s) = (600, 800000)$ and all are for real Hubble parameter dataset.

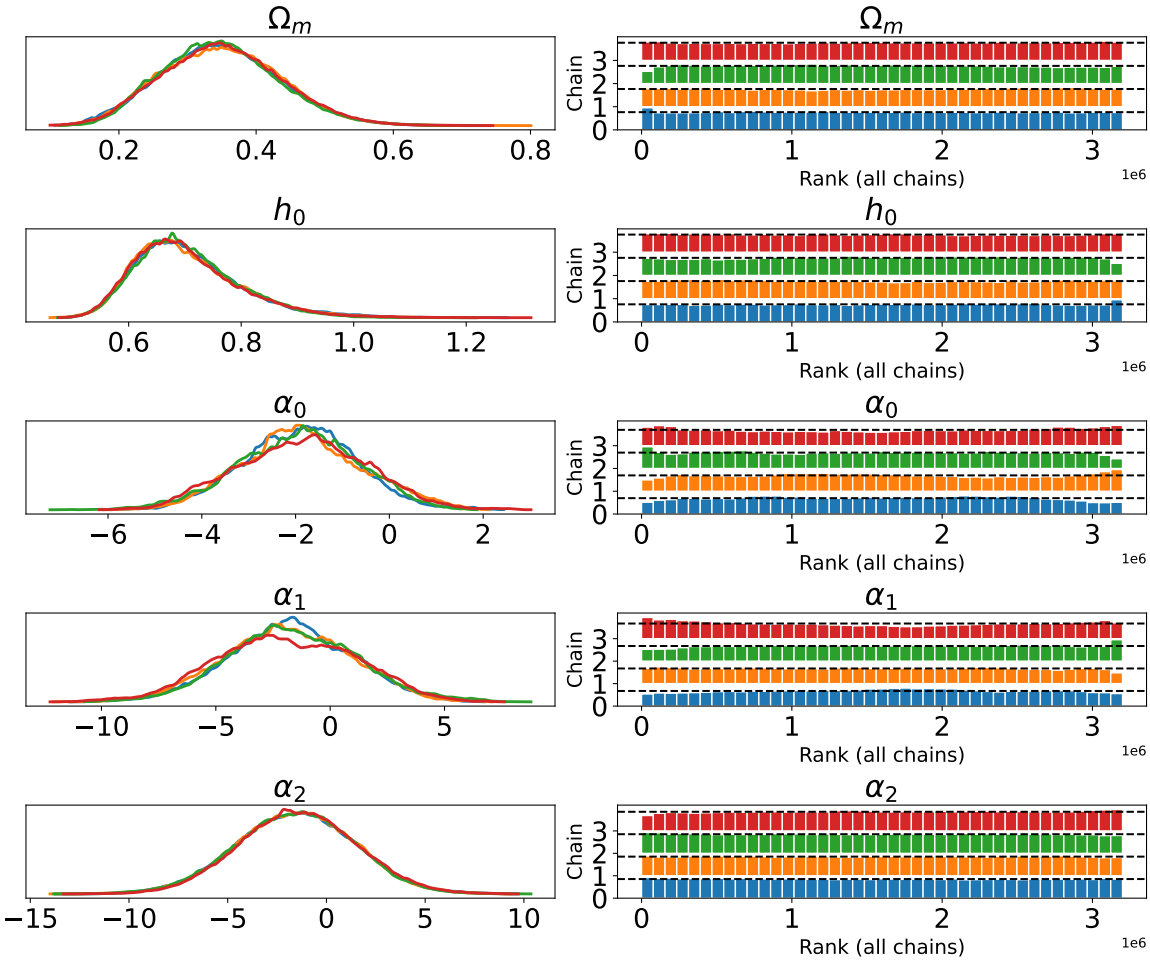

Figure A.7: This plots are done using the Metropolis Hasting sampling technique (MH) As in fig(3.6) the left column consists of a smoothed histogram, using kernel density estimation of the marginal posteriors of each stochastic random variable. The right column shows the number of successful draws from the parameter space, which depend upon the sample size chosen as well as the prior theory. The four MCMC chain plotted in different color and all are independent to each other. Real Hubble parameter dataset is used to generate the plot and the number of sample point as well as the simulated points taken from the PCA curve are $(n_d, M_s) = (600, 800000)$.

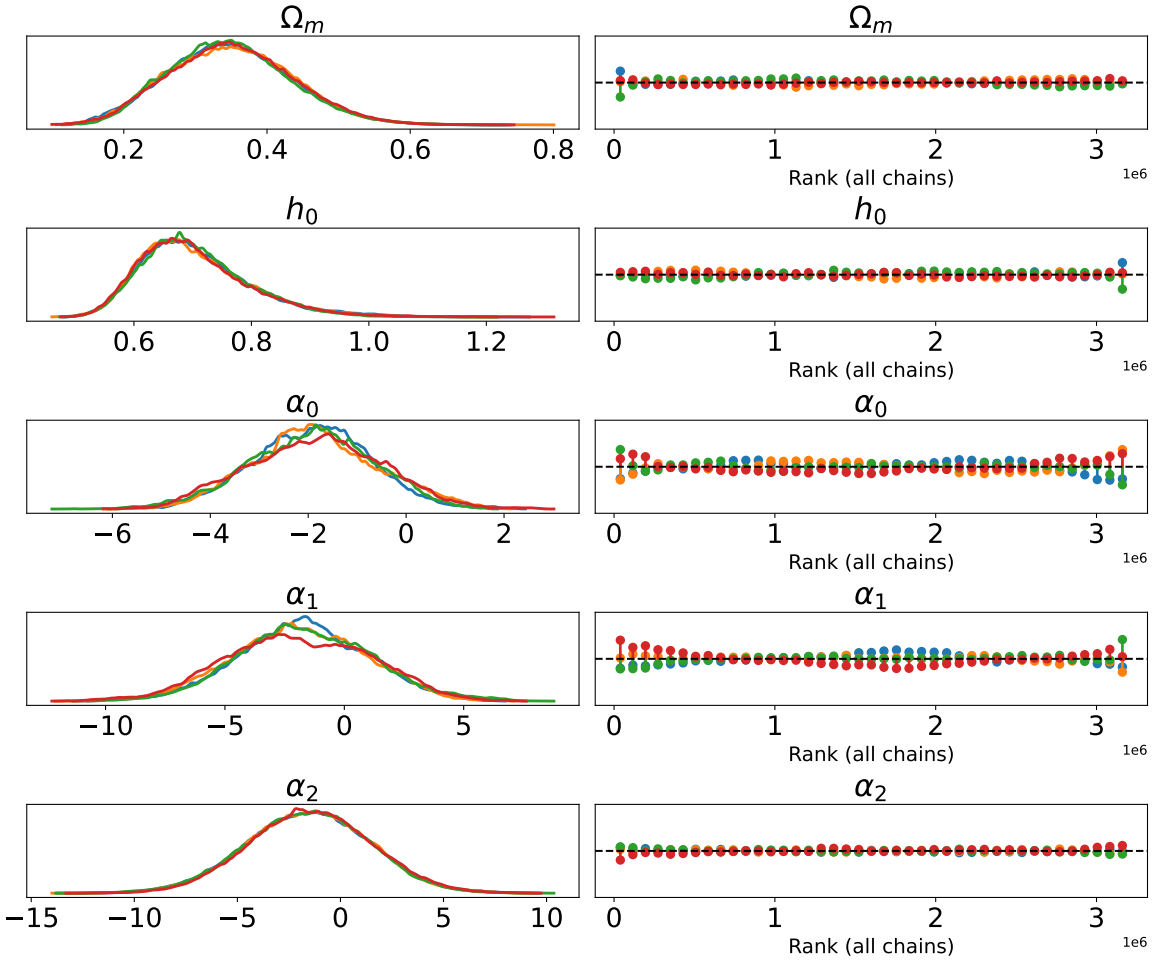

Figure A.8: This plots are done using the Metropolis Hasting sampling technique (MH). As in fig(3.5) the left column consists of a smoothed histogram, using kernel density estimation of the marginal posteriors of each stochastic random variable. The right hand column gives the auto-correlation for all the random variables for all the four independent chains, which are depicted with the vertical lines. Real Hubble parameter dataset is used to generate the plot and the number of sample points as well as the simulated points taken from the PCA curve are $(n_d, M_s) = (600, 800000)$.

Bibliography

[1] A. Einstein, *Cosmological considerations on the general theory of relativity*, pp. 175–188. 1952.

[2] A. Einstein, *The Field Equations of Gravitation*, *Sitzungsber. Preuss. Akad. Wiss. Berlin (Math. Phys.)* **1915** (1915) 844.

[3] V. M. Slipher, *Spectrographic Observations of Nebulae*, *Popular Astronomy* **23** (1915) 21.

[4] E. Hubble, *A relation between distance and radial velocity among extra-galactic nebulae*, *Proceedings of the National Academy of Sciences* **15** (1929) 168 [https://www.pnas.org/content/15/3/168.full.pdf].

[5] A. A. Penzias and R. W. Wilson, *A Measurement of Excess Antenna Temperature at 4080 Mc/s.*, *ApJ* **142** (1965) 419.

[6] R. H. Dicke, P. J. E. Peebles, P. G. Roll and D. T. Wilkinson, *Cosmic Black-Body Radiation*, *Astrophys. J.* **142** (1965) 414.

[7] G. Lemaitre, *A Homogeneous Universe of Constant Mass and Growing Radius Accounting for the Radial Velocity of Extragalactic Nebulae*, *Annales Soc. Sci. Bruxelles A* **47** (1927) 49.

[8] A. Friedman, *On the Curvature of space*, *Z. Phys.* **10** (1922) 377.

[9] G. F. Smoot, *Nobel lecture: Cosmic microwave background radiation anisotropies: Their discovery and utilization*, *Rev. Mod. Phys.* **79** (2007) 1349.

[10] F. Zwicky, *Die Rotverschiebung von extragalaktischen Nebeln*, *Helv. Phys. Acta* **6** (1933) 110.

[11] A. G. Riess, A. V. Filippenko, P. Challis, A. Clocchiatti, A. Diercks, P. M. Garnavich et al., *Observational Evidence from Supernovae for an*

Accelerating Universe and a Cosmological Constant, *The Astronomical Journal* **116** (1998) 1009 [astro-ph/9805201].

[12] S. Perlmutter, G. Aldering, G. Goldhaber, R. A. Knop, P. Nugent, P. G. Castro et al., *Measurements of Ω and Λ from 42 High-Redshift Supernovae*, *ApJ* **517** (1999) 565 [astro-ph/9812133].

[13] S. M. Carroll, W. H. Press and E. L. Turner, *The cosmological constant*, *Annual Review of Astronomy and Astrophysics* **30** (1992) 499.

[14] S. M. Carroll, *The Cosmological constant*, *Living Rev. Rel.* **4** (2001) 1 [astro-ph/0004075].

[15] M. S. Turner and M. White, *CDM models with a smooth component*, *prd* **56** (1997) R4439 [astro-ph/9701138].

[16] T. Padmanabhan, *Cosmological constant: The Weight of the vacuum*, *Phys. Rept.* **380** (2003) 235 [hep-th/0212290].

[17] P. J. E. Peebles and B. Ratra, *The Cosmological constant and dark energy*, *Rev. Mod. Phys.* **75** (2003) 559 [astro-ph/0207347].

[18] E. J. Copeland, M. Sami and S. Tsujikawa, *Dynamics of dark energy*, *Int. J. Mod. Phys.* **D15** (2006) 1753 [hep-th/0603057].

[19] M. Chevallier and D. Polarski, *Accelerating universes with scaling dark matter*, *Int. J. Mod. Phys.* **D10** (2001) 213 [gr-qc0009008].

[20] E. V. Linder, *Exploring the expansion history of the universe*, *Phys. Rev. Lett.* **90** (2003) 091301 [astro-ph/0208512].

[21] H. K. Jassal, J. S. Bagla and T. Padmanabhan, *WMAP constraints on low redshift evolution of darkenergy*, *Mon. Not. Roy. Astron. Soc.* **356** (2005) L11 [astro-ph/0404378].

[22] Y.-G. Gong and A. Wang, *Reconstruction of the deceleration parameter and the equation of state of dark energy*, *Phys. Rev.* **D75** (2007) 043520 [astro-ph/0612196].

[23] A. Mukherjee, *Acceleration of the universe: a reconstruction of the effective equation of state*, *Mon. Not. Roy. Astron. Soc.* **460** (2016) 273 [1605.08184].

[24] S. Vagnozzi, S. Dhawan, M. Gerbino, K. Freese, A. Goobar and O. Mena, *Constraints on the sum of the neutrino masses in dynamical dark energy models with w (z)≥-1 are tighter than those obtained in Λ CDM*, *Phys. Rev. D* **98** (2018) 083501 [1801.08553].

[25] E. Di Valentino, A. Melchiorri, E. V. Linder and J. Silk, *Constraining Dark Energy Dynamics in Extended Parameter Space*, *Phys. Rev.* **D96** (2017) 023523 [1704.00762].

[26] N. Bellomo, J. L. Bernal, G. Scelfo, A. Raccanelli and L. Verde, *Beware of commonly used approximations. Part I. Errors in forecasts*, *Journal of Cosmology and Astroparticle Physics* **2020** (2020) 016 [2005.10384].

[27] J. L. Bernal, N. Bellomo, A. Raccanelli and L. Verde, *Beware of commonly used approximations. Part II. Estimating systematic biases in the best-fit parameters*, *Journal of Cosmology and Astroparticle Physics* **2020** (2020) 017 [2005.09666].

[28] L. Verde, P. Protopapas and R. Jimenez, *Planck and the local Universe: Quantifying the tension*, *Physics of the Dark Universe* **2** (2013) 166 [1306.6766].

[29] Y. Fujii, *Origin of the gravitational constant and particle masses in a scale-invariant scalar-tensor theory*, *Phys. Rev. D* **26** (1982) 2580.

[30] R. D. Peccei, J. Solà and C. Wetterich, *Adjusting the cosmological constant dynamically: Cosmons and a new force weaker than gravity*, *Physics Letters B* **195** (1987) 183.

[31] L. H. Ford, *Cosmological-constant damping by unstable scalar fields*, *Phys. Rev. D* **35** (1987) 2339.

[32] C. Wetterich, *Cosmology and the Fate of Dilatation Symmetry*, *Nucl. Phys. B* **302** (1988) 668 [1711.03844].

[33] B. Ratra and P. J. E. Peebles, *Cosmological consequences of a rolling homogeneous scalar field*, *Phys. Rev. D* **37** (1988) 3406.

[34] Y. Fujii and T. Nishioka, *Model of a decaying cosmological constant*, *Phys. Rev. D* **42** (1990) 361.

[35] T. Chiba, N. Sugiyama and T. Nakamura, *Cosmology with x-matter*, *MNRAS* **289** (1997) L5 [astro-ph/9704199].

[36] P. G. Ferreira and M. Joyce, *Structure formation with a self-tuning scalar field*, *Phys. Rev. Lett.* **79** (1997) 4740.

[37] P. G. Ferreira and M. Joyce, *Cosmology with a primordial scaling field*, *Phys. Rev. D* **58** (1998) 023503 [astro-ph/9711102].

[38] R. R. Caldwell, R. Dave and P. J. Steinhardt, *Cosmological imprint of an energy component with general equation of state*, *Phys. Rev. Lett.* **80** (1998) 1582.

[39] S. M. Carroll, *Quintessence and the Rest of the World: Suppressing Long-Range Interactions*, *Phys. Rev. Lett.* **81** (1998) 3067 [astro-ph/9806099].

[40] E. J. Copeland, A. R. Liddle and D. Wands, *Exponential potentials and cosmological scaling solutions*, *Phys. Rev. D* **57** (1998) 4686.

[41] I. Zlatev, L. Wang and P. J. Steinhardt, *Quintessence, cosmic coincidence, and the cosmological constant*, *Phys. Rev. Lett.* **82** (1999) 896.

[42] P. J. Steinhardt, L. Wang and I. Zlatev, *Cosmological tracking solutions*, *Phys. Rev. D* **59** (1999) 123504.

[43] A. Hebecker and C. Wetterich, *Natural quintessence?*, *Physics Letters B* **497** (2001) 281 [hep-ph/0008205].

[44] T. Chiba, T. Okabe and M. Yamaguchi, *Kinetically driven quintessence*, *Phys. Rev. D* **62** (2000) 023511.

[45] C. Armendariz-Picon, V. Mukhanov and P. J. Steinhardt, *Dynamical Solution to the Problem of a Small Cosmological Constant and Late-Time Cosmic Acceleration*, *Phys. Rev. Lett.* **85** (2000) 4438 [astro-ph/0004134].

[46] C. Armendariz-Picon, V. Mukhanov and P. J. Steinhardt, *Essentials of k-essence*, *Phys. Rev. D* **63** (2001) 103510.

[47] A. Kamenshchik, U. Moschella and V. Pasquier, *An alternative to quintessence*, *Physics Letters B* **511** (2001) 265 [gr-qc/0103004].

[48] M. C. Bento, O. Bertolami and A. A. Sen, *Generalized chaplygin gas, accelerated expansion, and dark-energy-matter unification*, *Phys. Rev. D* **66** (2002) 043507.

[49] S. Capozziello and L. Z. Fang, *Curvature Quintessence*, *International Journal of Modern Physics D* **11** (2002) 483 [gr-qc/0201033].

[50] S. Capozziello, V. F. Cardone, S. Carloni and A. Troisi, *Curvature Quintessence Matched with Observational Data*, *International Journal of Modern Physics D* **12** (2003) 1969 [astro-ph/0307018].

[51] S. M. Carroll, V. Duvvuri, M. Trodden and M. S. Turner, *Is cosmic speed-up due to new gravitational physics?*, *Phys. Rev. D* **70** (2004) 043528 [astro-ph/0306438].

[52] L. Amendola, *Scaling solutions in general nonminimal coupling theories*, *Phys. Rev. D* **60** (1999) 043501 [astro-ph/9904120].

[53] J.-P. Uzan, *Cosmological scaling solutions of nonminimally coupled scalar fields*, *Phys. Rev. D* **59** (1999) 123510 [gr-qc/9903004].

[54] T. Chiba, *Quintessence, the gravitational constant, and gravity*, *Phys. Rev. D* **60** (1999) 083508 [gr-qc/9903094].

[55] N. Bartolo and M. Pietroni, *Scalar-tensor gravity and quintessence*, *Phys. Rev. D* **61** (1999) 023518 [hep-ph/9908521].

[56] F. Perrotta, C. Baccigalupi and S. Matarrese, *Extended quintessence*, *Phys. Rev. D* **61** (1999) 023507 [astro-ph/9906066].

[57] G. Dvali, G. Gabadadze and M. Porrati, *4D gravity on a brane in 5D Minkowski space*, *Physics Letters B* **485** (2000) 208 [hep-th/0005016].

[58] V. Sahni and Y. Shtanov, *Braneworld models of dark energy*, *Journal of Cosmology and Astroparticle Physics* **2003** (2003) 014 [astro-ph/0202346].

[59] N. Suzuki, D. Rubin, C. Lidman, G. Aldering, R. Amanullah, K. Barbary et al., *The Hubble Space Telescope Cluster Supernova Survey. V. Improving the Dark-energy Constraints above z > 1 and Building an Early-type-hosted Supernova Sample*, *ApJ* **746** (2012) 85 [1105.3470].

[60] C. Zhang, H. Zhang, S. Yuan, S. Liu, T.-J. Zhang and Y.-C. Sun, *Four new observational H(z) data from luminous red galaxies in the Sloan Digital Sky Survey data release seven*, *Research in Astronomy and Astrophysics* **14** (2014) 1221 [1207.4541].

[61] J. Simon, L. Verde and R. Jimenez, *Constraints on the redshift dependence of the dark energy potential*, *Phys. Rev.* **D71** (2005) 123001 [astro-ph/0412269].

[62] M. Moresco, L. Verde, L. Pozzetti, R. Jimenez and A. Cimatti, *New constraints on cosmological parameters and neutrino properties using the expansion rate of the Universe to z 1.75*, *JCAP* **1207** (2012) 053 [1201.6658].

[63] A. L. Ratsimbazafy, S. I. Loubser, S. Crawford, C. M. Cress, B. A. Bassett and P. Nichol, R. C.and Väisänen, *Age-dating Luminous Red Galaxies observed with the Southern African Large Telescope*, *Mon. Not. Roy. Astron. Soc.* **467** (2017) 3239 [1702.00418].

[64] M. Moresco, *Raising the bar: new constraints on the Hubble parameter with cosmic chronometers at z 2*, *Mon. Not. Roy. Astron. Soc.* **450** (2015) L16 [1503.01116].

[65] T. G. Brainerd, R. D. Blandford and I. Smail, *Weak Gravitational Lensing by Galaxies*, *ApJ* **466** (1996) 623 [astro-ph/9503073].

[66] I. P. dell'Antonio and J. A. Tyson, *Galaxy Dark Matter: Galaxy-Galaxy Lensing in the Hubble Deep Field*, *ApJL* **473** (1996) L17 [astro-ph/9608043].

[67] B. Geiger and P. Schneider, *Constraining the mass distribution of cluster galaxies by weak lensing*, *Monthly Notices of the Royal Astronomical Society* **295** (1998) 497 [https://academic.oup.com/mnras/article-pdf/295/3/497/18408309/295-3-4

[68] P. Natarajan, J.-P. Kneib and I. Smail, *Evidence for Tidal Stripping of Dark Matter Halos in Massive Cluster Lenses*, *ApJL* **580** (2002) L11 [astro-ph/0207049].

[69] T. Erben, H. Hildebrandt, L. Miller, L. van Waerbeke, C. Heymans, H. Hoekstra et al., *CFHTLenS: the Canada-France-Hawaii Telescope Lensing Survey - imaging data and catalogue products*, *MNRAS* **433** (2013) 2545 [1210.8156].

[70] H. Gao, Z. Li and B. Zhang, *FAST RADIO BURST/GAMMA-RAY BURST COSMOGRAPHY*, *The Astrophysical Journal* **788** (2014) 189.

[71] Z.-W. Zhao, Z.-X. Li, J.-Z. Qi, H. Gao, J.-F. Zhang and X. Zhang, *Cosmological Parameter Estimation for Dynamical Dark Energy Models with Future Fast Radio Burst Observations*, *ApJ* **903** (2020) 83 [2006.01450].

[72] B. Zhou, X. Li, T. Wang, Y.-Z. Fan and D.-M. Wei, *Fast radio bursts as a cosmic probe?*, *Phys. Rev. D* **89** (2014) 107303 [1401.2927].

[73] L. Verde, *Statistical Methods in Cosmology*, vol. 800, pp. 147–177. 2010. 10.1007/978-3-642-10598-2_4.

[74] D. N. Spergel, L. Verde, H. V. Peiris, E. Komatsu, M. R. Nolta, C. L. Bennett et al., *First-Year Wilkinson Microwave Anisotropy Probe (WMAP) Observations: Determination of Cosmological Parameters*, *ApJS* **148** (2003) 175 [astro-ph/0302209].

[75] D. N. Spergel, R. Bean, O. Doré, M. R. Nolta, C. L. Bennett, J. Dunkley et al., *Three-Year Wilkinson Microwave Anisotropy Probe (WMAP) Observations: Implications for Cosmology*, *ApJS* **170** (2007) 377 [astro-ph/0603449].

[76] E. Komatsu, J. Dunkley, M. R. Nolta, C. L. Bennett, B. Gold, G. Hinshaw et al., *Five-Year Wilkinson Microwave Anisotropy Probe Observations: Cosmological Interpretation*, *ApJS* **180** (2009) 330 [0803.0547].

[77] Planck Collaboration, N. Aghanim, Y. Akrami, M. Ashdown, J. Aumont, C. Baccigalupi et al., *Planck 2018 results. VI. Cosmological parameters*, *A&A* **641** (2020) A6 [1807.06209].

[78] E. Hubble, *A Relation between Distance and Radial Velocity among Extra-Galactic Nebulae*, *Proceedings of the National Academy of Science* **15** (1929) 168.

[79] M. Guidry and B. Messer, *The physics and astrophysics of type ia supernova explosions*, *Frontiers of Physics* **8** (2013) 111.

[80] D. M. Scolnic, D. O. Jones, A. Rest, Y. C. Pan, R. Chornock, R. J. Foley et al., *The Complete Light-curve Sample of Spectroscopically Confirmed SNe Ia from Pan-STARRS1 and Cosmological Constraints from the Combined Pantheon Sample*, *ApJ* **859** (2018) 101 [1710.00845].

[81] D. O. Jones, D. M. Scolnic, A. G. Riess, A. Rest, R. P. Kirshner, E. Berger et al., *Measuring Dark Energy Properties with Photometrically Classified Pan-STARRS Supernovae. II. Cosmological Parameters*, *ApJ* **857** (2018) 51 [1710.00846].

[82] A. G. Riess, R. P. Kirshner, B. P. Schmidt, S. Jha, P. Challis, P. M. Garnavich et al., *BVRI Light Curves for 22 Type IA Supernovae*, *The Astronomical Journal* **117** (1999) 707 [astro-ph/9810291].

[83] S. Jha, R. P. Kirshner, P. Challis, P. M. Garnavich, T. Matheson, A. M. Soderberg et al., *iUBVRI/ilight curves of 44 type ia supernovae*, *The Astronomical Journal* **131** (2006) 527.

[84] M. Hicken, P. Challis, S. Jha, R. P. Kirshner, T. Matheson, M. Modjaz et al., *CfA3: 185 TYPE ia SUPERNOVA LIGHT CURVES FROM THE CfA*, *The Astrophysical Journal* **700** (2009) 331.

[85] C. Contreras, M. Hamuy, M. M. Phillips, G. Folatelli, N. B. Suntzeff, S. E. Persson et al., *THE CARNEGIE SUPERNOVA PROJECT: FIRST PHOTOMETRY DATA RELEASE OF LOW-REDSHIFT TYPE ia SUPERNOVAE*, *The Astronomical Journal* **139** (2010) 519.

[86] G. Folatelli, M. M. Phillips, C. R. Burns, C. Contreras, M. Hamuy, W. L. Freedman et al., *THE CARNEGIE SUPERNOVA PROJECT: ANALYSIS OF THE FIRST SAMPLE OF LOW-REDSHIFT TYPE-ia SUPERNOVAE*, *The Astronomical Journal* **139** (2009) 120.

[87] M. D. Stritzinger, M. M. Phillips, L. N. Boldt, C. Burns, A. Campillay, C. Contreras et al., *THE CARNEGIE SUPERNOVA PROJECT: SECOND PHOTOMETRY DATA RELEASE OF LOW-REDSHIFT TYPE ia SUPERNOVAE*, *The Astronomical Journal* **142** (2011) 156.

[88] M. Ganeshalingam, W. Li and A. V. Filippenko, *Constraints on dark energy with the LOSS SN Ia sample*, *MNRAS* **433** (2013) 2240 [1307.0824].

[89] G. Miknaitis, G. Pignata, A. Rest, W. M. Wood-Vasey, S. Blondin, P. Challis et al., *The ESSENCE Supernova Survey: Survey Optimization, Observations, and Supernova Photometry*, *ApJ* **666** (2007) 674 [astro-ph/0701043].

[90] W. M. Wood-Vasey, G. Miknaitis, C. W. Stubbs, S. Jha, A. G. Riess, P. M. Garnavich et al., *Observational constraints on the nature of dark energy: First cosmological results from the ESSENCE supernova survey*, *The Astrophysical Journal* **666** (2007) 694.

[91] G. Narayan, A. Rest, B. E. Tucker, R. J. Foley, W. M. Wood-Vasey, P. Challis et al., *Light Curves of 213 Type Ia Supernovae from the ESSENCE Survey*, *ApJS* **224** (2016) 3 [1603.03823].

[92] A. Conley, J. Guy, M. Sullivan, N. Regnault, P. Astier, C. Balland et al., *Supernova Constraints and Systematic Uncertainties from the First Three Years of the Supernova Legacy Survey*, *ApJS* **192** (2011) 1 [1104.1443].

[93] M. Sullivan, J. Guy, A. Conley, N. Regnault, P. Astier, C. Balland et al., *SNLS3: Constraints on Dark Energy Combining the Supernova Legacy Survey Three-year Data with Other Probes*, *ApJ* **737** (2011) 102 [1104.1444].

[94] J. A. Frieman, B. Bassett, A. Becker, C. Choi, D. Cinabro, F. DeJongh et al., *The Sloan Digital Sky Survey-II Supernova Survey: Technical Summary*, *The Astronomical Journal* **135** (2008) 338 [0708.2749].

[95] R. Kessler, A. C. Becker, D. Cinabro, J. Vanderplas, J. A. Frieman, J. Marriner et al., *First-Year Sloan Digital Sky Survey-II Supernova Results: Hubble Diagram and Cosmological Parameters*, *ApJS* **185** (2009) 32 [0908.4274].

[96] M. Sako, B. Bassett, A. C. Becker, P. J. Brown, H. Campbell, R. Wolf et al., *The Data Release of the Sloan Digital Sky Survey-II Supernova Survey*, *PASP* **130** (2018) 064002 [1401.3317].

[97] A. Rest, D. Scolnic, R. J. Foley, M. E. Huber, R. Chornock, G. Narayan et al., *Cosmological Constraints from Measurements of Type Ia Supernovae Discovered during the First 1.5 yr of the Pan-STARRS1 Survey*, *ApJ* **795** (2014) 44 [1310.3828].

[98] D. Scolnic, A. Rest, A. Riess, M. E. Huber, R. J. Foley, D. Brout et al., *Systematic Uncertainties Associated with the Cosmological Analysis of the First Pan-STARRS1 Type Ia Supernova Sample*, *ApJ* **795** (2014) 45 [1310.3824].

[99] N. Suzuki, D. Rubin, C. Lidman, G. Aldering, R. Amanullah, K. Barbary et al., *The Hubble Space Telescope Cluster Supernova Survey. V. Improving the Dark-energy Constraints above z > 1 and Building an Early-type-hosted Supernova Sample*, *ApJ* **746** (2012) 85 [1105.3470].

[100] A. G. Riess, L.-G. Strolger, J. Tonry, S. Casertano, H. C. Ferguson, B. Mobasher et al., *Type ia supernova discoveries atiz/i&gt 1 from theihubble space telescope/i: Evidence for past deceleration and constraints on dark energy evolution*, *The Astrophysical Journal* **607** (2004) 665.

[101] A. G. Riess, L.-G. Strolger, S. Casertano, H. C. Ferguson, B. Mobasher, B. Gold et al., *New Hubble Space Telescope Discoveries of Type Ia Supernovae at z >= 1: Narrowing Constraints on the Early Behavior of Dark Energy*, *ApJ* **659** (2007) 98 [astro-ph/0611572].

[102] S. A. Rodney, A. G. Riess, L.-G. Strolger, T. Dahlen, O. Graur, S. Casertano et al., *TYPE ia SUPERNOVA RATE MEASUREMENTS TO REDSHIFT 2.5 FROM CANDELS: SEARCHING FOR PROMPT EXPLOSIONS IN THE EARLY UNIVERSE*, *The Astronomical Journal* **148** (2014) 13.

[103] O. Graur, S. A. Rodney, D. Maoz, A. G. Riess, S. W. Jha, M. Postman et al., *Type-Ia Supernova Rates to Redshift 2.4 from CLASH: The Cluster Lensing And Supernova Survey with Hubble*, *ApJ* **783** (2014) 28 [1310.3495].

[104] A. G. Riess, S. A. Rodney, D. M. Scolnic, D. L. Shafer, L.-G. Strolger, H. C. Ferguson et al., *Type Ia Supernova Distances at Redshift >1.5 from the Hubble Space Telescope Multi-cycle Treasury Programs: The Early Expansion Rate*, *ApJ* **853** (2018) 126 [1710.00844].

[105] O. Farooq, F. R. Madiyar, S. Crandall and B. Ratra, *Hubble parameter measurement constraints on the redshift of the deceleration-acceleration transition, dynamical dark energy, and space curvature*, *The Astrophysical Journal* **835** (2017) 26.

[106] O. Farooq and B. Ratra, *Hubble parameter measurement constraints on the cosmological deceleration-acceleration transition redshift*, *The Astrophysical Journal Letters* **766** (2013) L7.

[107] O. Farooq, D. Mania and B. Ratra, *Hubble parameter measurement constraints on dark energy*, *The Astrophysical Journal* **764** (2013) 138.

[108] L. Samushia and B. Ratra, *Cosmological constraints from hubble parameter versus redshift data*, *The Astrophysical Journal Letters* **650** (2006) L5.

[109] D. Stern, R. Jimenez, L. Verde, M. Kamionkowski and S. A. Stanford, *Cosmic chronometers: constraining the equation of state of dark energy. I: H (z) measurements*, *Journal of Cosmology and Astroparticle Physics* **2010** (2010) 008.

[110] M. Moresco, L. Pozzetti, A. Cimatti, R. Jimenez, C. Maraston, L. Verde et al., *A 6% measurement of the hubble parameter at z∼0.45: direct evidence of the epoch of cosmic re-acceleration*, *Journal of Cosmology and Astroparticle Physics* **2016** (2016) 014.

[111] M. Moresco, *Raising the bar: new constraints on the Hubble parameter with cosmic chronometers at $z \sim 2$* , *Monthly Notices of the Royal Astronomical Society: Letters* **450** (2015) L16.

[112] M. Moresco, A. Cimatti, R. Jimenez, L. Pozzetti, G. Zamorani, M. Bolzonella et al., *Improved constraints on the expansion rate of the universe up to $z \sim 1.1$ from the spectroscopic evolution of cosmic chronometers*, *Journal of Cosmology and Astroparticle Physics* **2012** (2012) 006.

[113] C.-H. Chuang and Y. Wang, *Modelling the anisotropic two-point galaxy correlation function on small scales and single-probe measurements of $H(z)$, $DA(z)$ and $f(z)\sigma_8(z)$ from the sloan digital sky survey DR7 luminous red galaxies*, *Monthly Notices of the Royal Astronomical Society* **435** (2013) 255.

[114] Y. Chen and B. Ratra, *Hubble parameter data constraints on dark energy*, *Physics Letters B* **703** (2011) 406 .

[115] R. Jimenez and A. Loeb, *Constraining Cosmological Parameters Based on Relative Galaxy Ages*, *ApJ* **573** (2002) 37 [astro-ph/0106145].

[116] J. Peacock, R. Jimenez, J. Dunlop, I. Waddington, H. Spinrad, D. Stern et al., *Old high-redshift galaxies and primordial density fluctuation spectra*, *Monthly Notices of the Royal Astronomical Society* **296** (1998) 1089 [https://academic.oup.com/mnras/article-pdf/296/4/1089/18408369/296-4

[117] J. S. Alcaniz and J. A. S. Lima, *Dark energy and the epoch of galaxy formation*, *The Astrophysical Journal* **550** (2001) L133.

[118] J. V. Wall and C. R. Jenkins, *Practical Statistics for Astronomers*, Cambridge Observing Handbooks for Research Astronomers. Cambridge University Press, 2003, 10.1017/CBO9780511536618.

[119] *Bayesian Methods in Cosmology*. Cambridge University Press, 2009, 10.1017/CBO9780511802461.

[120] R. Trotta, *Applications of Bayesian model selection to cosmological parameters*, *Monthly Notices of the Royal Astronomical Society* **378** (2007) 72 [https://academic.oup.com/mnras/article-pdf/378/1/72/3961005/mnras037

[121] A. R. Liddle, *Information criteria for astrophysical model selection*, *Monthly Notices of the Royal Astronomical Society: Letters* **377** (2007) L74 [https://academic.oup.com/mnrasl/article-pdf/377/1/L74/4044139/377-1-

[122] N. Metropolis, A. W. Rosenbluth, M. N. Rosenbluth, A. H. Teller and E. Teller, *Equation of State Calculations by Fast Computing Machines*, **21** (1953) 1087.

[123] W. K. Hastings, *Monte Carlo sampling methods using Markov chains and their applications*, *Biometrika* **57** (1970) 97 [https://academic.oup.com/biomet/article-pdf/57/1/97/23940249/57-1-97.pdf]

[124] A. Joseph, *Markov Chain Monte Carlo Methods in Quantum Field Theories: A Modern Primer*, SpringerBriefs in Physics, Springer, 12, 2019, 1912.10997, DOI.

[125] M. D. Hoffman and A. Gelman, *The No-U-Turn Sampler: Adaptively Setting Path Lengths in Hamiltonian Monte Carlo*, *arXiv e-prints* (2011) arXiv:1111.4246 [1111.4246].

[126] D. Huterer and G. Starkman, *Parametrization of Dark-Energy Properties: A Principal-Component Approach*, *Phys. Rev. Lett.* **90** (2003) 031301 [astro-ph/0207517].

[127] C. Clarkson and C. Zunckel, *Direct Reconstruction of Dark Energy*, *Phys. Rev. Lett.* **104** (2010) 211301 [1002.5004].

[128] D. Huterer and A. Cooray, *Uncorrelated estimates of dark energy evolution*, *Phys. Rev. D* **71** (2005) 023506 [astro-ph/0404062].

[129] W. Zheng and H. Li, *Constraints on parameterized dark energy properties from new observations with principal component analysis*, *Astropart. Phys.* **86** (2017) 1.

[130] E. E. O. Ishida and R. S. de Souza, *Hubble parameter reconstruction from a principal component analysis: minimizing the bias*, *A&A* **527** (2011) A49 [1012.5335].

[131] H.-F. Qin, X.-B. Li, H.-Y. Wan and T.-J. Zhang, *Reconstructing equation of state of dark energy with principal component analysis*, 1501.02971.

[132] Z.-E. Liu, H.-R. Yu, T.-J. Zhang and Y.-K. Tang, *Direct reconstruction of dynamical dark energy from observational Hubble parameter data*, *Phys. Dark Univ.* **14** (2016) 21 [1501.04176].

[133] S. Nesseris and J. García-Bellido, *Comparative analysis of model-independent methods for exploring the nature of dark energy*, *Phys. Rev. D* **88** (2013) 063521 [1306.4885].

[134] R. G. Crittenden, L. Pogosian and G.-B. Zhao, *Investigating dark energy experiments with principal components*, *JCAP* **0912** (2009) 025 [astro-ph/0510293].

[135] V. Miranda and C. Dvorkin, *Model-independent predictions for smooth cosmic acceleration scenarios*, *Phys. Rev. D* **98** (2018) 043537 [1712.04289].

[136] L. Hart and J. Chluba, *Improved model-independent constraints on the recombination era and development of a direct projection method*, *arXiv e-prints* (2019) arXiv:1912.04682 [1912.04682].

[137] A. Hojjati, G.-B. Zhao, L. Pogosian, A. Silvestri, R. Crittenden and K. Koyama, *Cosmological tests of general relativity: A principal component analysis*, *Phys. Rev. D* **85** (2012) 043508 [1111.3960].

[138] R. Nair and S. Jhingan, *Is dark energy evolving?*, *Journal of Cosmology and Astroparticle Physics* **2013** (2013) 049 [1212.6644].

[139] L. Hart and J. Chluba, *Varying fundamental constants principal component analysis: additional hints about the Hubble tension*, 2107.12465.

[140] H.-R. Yu, S. Yuan and T.-J. Zhang, *Nonparametric reconstruction of dynamical dark energy via observational Hubble parameter data*, *Phys. Rev. D* **88** (2013) 103528 [1310.0870].

[141] D. S. Sivia and J. Skilling, *Data Analysis - A Bayesian Tutorial*, Oxford Science Publications. Oxford University Press, 2nd ed., 2006.

[142] C. L. Steinhardt and A. S. Jermyn, *Nonparametric Methods in Astronomy: Think, Regress, Observe—Pick Any Three*, *PASP* **130** (2018) 023001 [1801.06545].

[143] A. Montiel, R. Lazkoz, I. Sendra, C. Escamilla-Rivera and V. Salzano, *Nonparametric reconstruction of the cosmic expansion with local regression smoothing and simulation extrapolation*, *Phys. Rev. D* **89** (2014) 043007 [1401.4188].

[144] J. E. González, J. S. Alcaniz and J. C. Carvalho, *Non-parametric reconstruction of cosmological matter perturbations*, *Journal of Cosmology and Astroparticle Physics* **2016** (2016) 016 [1602.01015].

[145] P. L. Taylor, T. D. Kitching and J. D. McEwen, *Nonparametric cosmology with cosmic shear*, *Phys. Rev. D* **99** (2019) 043532 [1810.10552].

[146] N. Porqueres, T. A. Enßlin, M. Greiner, V. Böhm, S. Dorn, P. Ruiz-Lapuente et al., *Cosmic expansion history from SNe Ia data via information field theory: the charm code*, *A&A* **599** (2017) A92 [1608.04007].

[147] A. Diaz Rivero, V. Miranda and C. Dvorkin, *Observable predictions for massive-neutrino cosmologies with model-independent dark energy*, *Phys. Rev. D* **100** (2019) 063504 [1903.03125].

[148] R. Arjona and S. Nesseris, *What can machine learning tell us about the background expansion of the Universe?*, *Phys. Rev. D* **101** (2020) 123525 [1910.01529].

[149] A. Gómez-Valent and L. Amendola, *H_0 from cosmic chronometers and Type Ia supernovae, with Gaussian Processes and the novel Weighted Polynomial Regression method*, *Journal of Cosmology and Astroparticle Physics* **2018** (2018) 051 [1802.01505].

[150] M. Sahlen, A. R. Liddle and D. Parkinson, *Direct reconstruction of the quintessence potential*, *Phys. Rev.* **D72** (2005) 083511 [astro-ph/0506696].

[151] T. Holsclaw, U. Alam, B. Sansó, H. Lee, K. Heitmann, S. Habib et al., *Nonparametric Dark Energy Reconstruction from Supernova Data*, *prl* **105** (2010) 241302 [1011.3079].

[152] A. Shafieloo, A. G. Kim and E. V. Linder, *Gaussian process cosmography*, *prd* **85** (2012) 123530 [1204.2272].

[153] F. Gerardi, M. Martinelli and A. Silvestri, *Reconstruction of the Dark Energy equation of state from latest data: the impact of theoretical priors*, *Journal of Cosmology and Astroparticle Physics* **2019** (2019) 042 [1902.09423].

[154] C. E. Rasmussen and C. K. I. Williams, *Gaussian Processes for Machine Learning (Adaptive Computation and Machine Learning)*. The MIT Press, 2005.

[155] A. Bonilla, S. Kumar and R. C. Nunes, *Measurements of H_0 and reconstruction of the dark energy properties from a model-independent joint analysis*, *arXiv e-prints* (2020) arXiv:2011.07140 [2011.07140].

[156] J. Shlens, *A Tutorial on Principal Component Analysis*, *arXiv e-prints* (2014) arXiv:1404.1100 [1404.1100].

[157] Kendall, *A NEW MEASURE OF RANK CORRELATION*, *Biometrika* **30** (1938) 81 [https://academic.oup.com/biomet/article-pdf/30/1-2/81/423380/30-1-2-81.pd

[158] R Core Team, *R: A Language and Environment for Statistical Computing*. R Foundation for Statistical Computing, Vienna, Austria, 2013.

[159] J. Görtler, T. Spinner, D. Streeb, D. Weiskopf and O. Deussen, *Uncertainty-Aware Principal Component Analysis*, *arXiv e-prints* (2019) arXiv:1905.01127 [1905.01127].

[160] L. Guttman, *On smith's paper on "'randomness of error' in reproducible scales"*, *Educational and Psychological Measurement* **13** (1953) 505 [https://doi.org/10.1177/001316445301300315].

[161] C. Ma and T.-J. Zhang, *Power of Observational Hubble Parameter Data: A Figure of Merit Exploration*, *ApJ* **730** (2011) 74 [1007.3787].

[162] A. V. Pan and U. Alam, *Reconstructing Dark Energy : A Comparison of Cosmological Parameters*, *arXiv e-prints* (2010) arXiv:1012.1591 [1012.1591].

[163] Planck Collaboration, N. Aghanim, Y. Akrami, M. Ashdown, J. Aumont, C. Baccigalupi et al., *Planck 2018 results. VI. Cosmological parameters*, *arXiv e-prints* (2018) arXiv:1807.06209 [1807.06209].

[164] M. Vazirnia and A. Mehrabi, *Nonparametric modeling of cosmological database on the χ^2 distribution*, *Phys. Rev. D* **104** (2021) 123530 [2107.11539].

[165] D. Huterer and M. S. Turner, *Prospects for probing the dark energy via supernovadistance measurements*, *Phys. Rev.* **D60** (1999) 081301 [astro-ph/9808133].

[166] A. Mukherjee, N. Paul and H. K. Jassal, *Constraining the dark energy statefinder hierarchy in a kinematic approach*, *Journal of Cosmology and Astro-Particle Physics* **2019** (2019) 005 [1809.08849].

[167] B. S. Haridasu, V. V. Lukovi ć, M. Moresco and N. Vittorio, *An improved model-independent assessment of the late-time cosmic expansion*, *Journal of Cosmology and Astro-Particle Physics* **2018** (2018) 015 [1805.03595].

[168] A. Singh, A. Sangwan and H. K. Jassal, *Low redshift observational constraints on tachyon models of dark energy*, *JCAP* **1904** (2019) 047 [1811.07513].

[169] H. K. Jassal, *A comparison of perturbations in fluid and scalar field models of dark energy*, *Phys. Rev.* **D79** (2009) 127301 [0903.5370].

[170] S. Nesseris and L. Perivolaropoulos, *Comparison of cosmological models using recent supernova data*, *Phys. Rev. D* **70** (2004) 043531 [astro-ph/0401556].

[171] S. Nesseris and L. Perivolaropoulos, *Comparison of the legacy and gold type Ia supernovae dataset constraints on dark energy models*, *Phys. Rev. D* **72** (2005) 123519 [astro-ph/0511040].

[172] S. Nesseris and L. Perivolaropoulos, *Crossing the phantom divide: theoretical implications and observational status*, *Journal of Cosmology and Astroparticle Physics* **2007** (2007) 018 [astro-ph/0610092].

[173] A. Sangwan, A. Tripathi and H. K. Jassal, *Observational constraints on quintessence models of dark energy*, *arXiv e-prints* (2018) arXiv:1804.09350 [1804.09350].

[174] R. Sharma, A. Mukherjee and H. K. Jassal, *Reconstruction of late-time cosmology using Principal Component Analysis*, *arXiv e-prints* (2020) arXiv:2004.01393 [2004.01393].

[175] R. Nair and S. Jhingan, *Is dark energy evolving?*, *Journal of Cosmology and Astroparticle Physics* **2013** (2013) 049 [1212.6644].

[176] L. Hart and J. Chluba, *Varying fundamental constants principal component analysis: additional hints about the Hubble tension*, *MNRAS* **510** (2022) 2206 [2107.12465].

[177] E. Kreyszig, H. Kreyszig and E. J. Norminton, *Advanced engineering mathematics*. Wiley, Hoboken, N.J., tenth ed., 2011.

[178] J. Salvatier, T. V. Wiecki and C. Fonnesbeck, *Probabilistic programming in python using pymc3*, *PeerJ Computer Science* **2** (2016) e55.

[179] A. Gelman and D. B. Rubin, *Inference from iterative simulation using multiple sequences*, *Statistical Science* **7** (1992) 457.

[180] M. Chevallier and D. Polarski, *Accelerating Universes with Scaling Dark Matter*, *International Journal of Modern Physics D* **10** (2001) 213 [gr-qc/0009008].

[181] E. V. Linder, *Exploring the Expansion History of the Universe*, *Phys. Rev. Lett.* **90** (2003) 091301 [astro-ph/0208512].

[182] S. P. Brooks and A. Gelman, *General methods for monitoring convergence of iterative simulations*, *Journal of Computational and Graphical Statistics* **7** (1998) 434 [https://www.tandfonline.com/doi/pdf/10.1080/10618600.1998.10474787].

[183] M. K. Cowles and B. P. Carlin, *Markov chain monte carlo convergence diagnostics: A comparative review*, *Journal of the American Statistical Association* **91** (1996) 883 [https://www.tandfonline.com/doi/pdf/10.1080/01621459.1996.10476956].